Scanning Tunneling Microscopy and Atomic Force Microscopy Investigation of Organic Molecules

Doctoral thesis for obtaining the academic degree

Doctor of natural sciences (Dr.rer.nat.)

submitted by

Tomasz Michnowicz

at the

Universität Konstanz

Faculty of Sciences

Department of Physics

Konstanz, 2019

Abstract

The importance of organic chemistry in modern science and industry has lead to an emergence of a variety of advanced techniques for the identification of organic molecules. The most common of them are vibrational spectroscopies, diffraction techniques and nuclear magnetic resonance spectroscopy (NMR). Resolving the molecular structures with these methods relies on the unique responses and interactions of the ensemble of the molecules to the applied stimuli, such as electromagnetic radiation or particle beams. Another approach to the structural determination relies on the real-space investigation and is offered by microscopy techniques. One of them, scanning tunneling microscopy (STM) is capable of identification of the organic structures by imaging explicitly single molecules at the nanoscale. Further integration of non-contact atomic force microscopy (nc-AFM) with STM allows direct observation of the molecular structures with atomic resolution. This unique possibility can be utilized to study chemistry with extraordinary precision at the scale of individual molecules. In this thesis, a homebuilt combined STM/nc-AFM instrument is used to investigate three distinct organic systems, focusing on the structure elucidation and chemical reactivity of single organic molecules.

The first research project concerns the structural and electronic properties of a tetracenothiophene (TCT), adsorbed on the Cu(111) surface. The TCT molecule is a pentacene derivative with a sulfur-containing thiophene group. The two pathways of an electric-field-driven desulfurization reaction of this thiophene group are demonstrated: a two-step pathway and a direct transition from the intact to the desulfurized state. The reaction is triggered by positioning the STM tip above the thiophene moiety and ramping the bias voltage. In the two-step pathway, the first step is induced only by the presence of the electric field. The second step can be induced by applying the electric field and simultaneously injecting the electrons into the system. With both high-resolution STM and nc-AFM imaging, we identify the two steps as the subsequent splitting of the two C-S bonds of the thiophene group. As a result, the two carbon atoms of the former thiophene group form covalent bonds to Cu surface atoms. After the reaction, the desulfurized molecule is anchored to the substrate mechanically. The conductance measured through the molecule suspended between the tip and the sample electrodes increases by ~50 % after the reaction. Due to the properties of the facile thiophene-copper bonding, it is of interest as an anchoring technique in single-molecule electronics.

In the second project, the chemical reactions induced by hyperthermal collisions of Reichardt's Dye molecules with a metal surface are investigated. Collisions with hyperthermal kinetic energies lead to a non-equilibrium process where the high energy of the molecules is dispersed in a very short time. By controlling the kinetic energy of the incident organic molecules with Electrospray Ionization-Beam Deposition (ES-IBD), we accessed new, thermally inaccessible states. We identified both thermally and kinetically created species of Reichardt's Dye with the STM/nc-AFM imaging and compared the results. Hyperthermal deposition of Reichardt's Dye indeed leads to the creation of new states that are inaccessible by thermal activation. This approach to reaction kinetics can be applied to different systems to yield new molecular species.

In the last chapter, we test the ability of STM/nc-AFM to identify the branched structures of small carbohydrates. This class of molecules is representative of many biologically active molecules that are difficult to analyze with traditional methods such as mass spectrometry and nuclear magnetic resonance spectroscopy. The carbohydrates can exhibit a polymerized and branched structure, often consisting of monosaccharides with identical mass and composition. Therefore, the full identification of their structure, if possible at all, requires a series of precise experiments, significantly increasing the material consumption. Carbohydrates, as well as proteins and peptides, are often not available in required amounts. The real space approach to investigating carbohydrates, including STM and nc-AFM, may provide information about the branching aspect of carbohydrate structure at low material cost, thanks to the possibility of structural identification performed on a single organic molecule. We analyzed a model system consisting of linear pentamers and branched hexamers of mannose. The studies of these linear carbohydrates lead to the identification of single monosaccharide units on Cu(100) and Cu(111). We also identified and assigned folded structures encountered during the experiments to single and double pentamers of mannose. Moreover, the imaging allowed us to approximately localize the branching points in the branched hexamers of mannose. This effort demonstrates the potential of using STM/nc-AFM as a complementary technique for the structural identification of carbohydrates.

Zusammenfassung

Die Bedeutung der organischen Chemie in der modernen Wissenschaft und Industrie hat dazu geführt, dass eine Vielzahl von fortschrittlichen Techniken zur Identifizierung von organischen Molekülen entwickelt wurde. Am häufigsten sind Schwingungsspektroskopie, Beugungstechniken und - Kernspinresonanzspektroskopie (NMR). Die Auflösung - molekularer Strukturen mit diesen Methoden beruht auf den einzigartigen Reaktionen und Wechselwirkungen des Ensembles der Moleküle auf die angewandten Reize, wie elektromagnetische Strahlung oder Teilchenstrahlen. Ein weiterer Ansatz zur strukturellen Bestimmung basiert auf der Realraumuntersuchung und wird durch Mikroskopietechniken angeboten. Eine- von ihnen, die Rastertunnelmikroskopie (RTM), ist in der Lage, die organischen Strukturen zu identifizieren, indem sie explizit einzelne Moleküle im Nanometerbereich abbildet. Die zusätzliche Integration der berührungslosen Rasterkraftmikroskopie (nc-AFM) mit RTM ermöglicht die direkte Beobachtung der Molekülstrukturen mit atomarer Auflösung. Diese einzigartige Möglichkeit kann genutzt werden, um die Chemie mit außergewöhnlicher Präzision im Maßstab einzelner Moleküle zu untersuchen. In dieser Arbeit wird ein selbstgebautes kombiniertes RTM/nc-AFM-Instrument verwendet, um drei verschiedene organische Systeme zu untersuchen, die sich auf die Strukturauflösung und chemische Reaktivität einzelner organischer Moleküle konzentrieren.

Das erste Forschungsprojekt befasst sich mit den strukturellen und elektronischen Eigenschaften von Tetracenothiophen (TCT), adsorbiert Cu(111). TCT ist ein Pentacenderivat mit einer schwefelhaltigen Thiophengruppe. Zwei Wege einer, durch ein elektrisches Feld kontrollierten, Entschwefelungsreaktion dieser Thiophengruppe werden demonstriert: ein zweistufiger Weg und ein direkter Übergang vom intakten zum entschwefelten Zustand. Die Reaktion wird ausgelöst, indem die STM-Spitze über dem Thiophenteil positioniert und die Biasspannung erhöht wird. Im zweistufigen Weg ist das elektrische Feld alleine nur für den ersten Schritt verantwortlich. Der zweite Schritt kann durch Anlegen des elektrischen Feldes und gleichzeitige Injektionder Elektronen in das System eingeleitet werden. Sowohl bei der hochauflösenden STM- als auch bei der nc-AFM-Bildgebung identifizieren wir die beiden Schritte als die aufeinanderfolgende Trennung der beiden C-S-Bindungen der Thiophengruppe. Die beiden Kohlenstoffatome der ehemaligen Thiophengruppe gehen kovalente Bindungen zu

Cu-Oberflächenatomen ein. Nach der Reaktion wird das entschwefelte Molekül mechanisch auf dem Substrat verankert. Der Leitwert, gemessen durch das zwischen der Spitzen- und derProbenelektrode schwebende Molekül, steigt nach der Reaktion um ~ 50 %. Aufgrund der Eigenschaften der einfachen Thiophen-Kupfer-Bindung ist sie als Verankerungstechnik in der Einzelmolekülelektronik von Interesse.

Im zweiten Projekt werden die chemischen Reaktionen untersucht, die durch hyperthermale Kollisionen von Reichardts Farbstoffmolekülen mit einer Metalloberfläche hervorgerufen werden. Kollisionen mit hyperthermischen kinetischen Energien führen zu einem Nichtgleichgewichtsprozess, bei dem die hohe Energie der Moleküle in sehr kurzer Zeit verteilt wird. Durch die Steuerung der kinetischen Energie der einfallenden organischen Moleküle mit Electrospray Ionization-Beam Deposition (ES-IBD) haben wir neue, thermisch unzugängliche Zustände erreicht. Wir identifizierten sowohl thermisch als auch kinetisch erzeugte Arten von Reichardts Farbstoff mit der STM/nc-AFM-Bildgebung und verglichen die Ergebnisse. Die hyperthermale Deposition von Reichardts Farbstoff führt in der Tat zur Entstehung neuer Zustände, die durch thermische Aktivierung nicht zugänglich sind. Dieser Ansatz zur Erforschung der Reaktionskinetik kann auf verschiedene Systeme angewendet werden, um neue molekulare Spezies zu erhalten.

Im letzten Kapitel testen wir die Fähigkeit von STM/nc-AFM, die verzweigten Strukturen von kleinen Kohlenhydraten zu identifizieren. Diese Molekülklasse ist repräsentativ für viele biologisch aktive Moleküle, die mit herkömmlichen Methoden wie der Massenspektrometrie und der Kernspinresonanzspektroskopie schwer zu analysieren sind. Die Kohlenhydrate können eine polymerisierte und verzweigte Struktur aufweisen, die oft aus Monosacchariden mit identischer Masse und Zusammensetzung besteht.Daher erfordert die vollständige Identifizierung ihrer Struktur, wenn sie überhaupt möglich ist, eine Reihe von präzisen Experimenten, die den Materialverbrauch deutlich erhöhen. Kohlenhydrate sowie Proteine und Peptide sind oft nicht in ausreichender Menge verfügbar. Der Realraumansatz zur Untersuchung von Kohlenhydraten, einschließlich STM und nc-AFM, kann Informationen über den Verzweigungsaspekt der Kohlenhydratstruktur bei niedrigen Materialkosten liefern, dank der Möglichkeit der strukturellen Identifizierung an einem einzigen organischen Molekül. Wir analysierten ein Modellsystem, bestehend aus linearen Pentameren und verzweigten Hexameren von Mannose. Die Studien dieser linearen Kohlenhydrate führen zur Identifizierung einzelner Monosaccharideinheiten auf Cu(100) und Cu(111). Wir identifizierten und ordneten auch gefaltete Strukturen zu, die während der Experimente bei einzelnen und doppelten Pentameren von Mannose auftraten. Darüber hinaus ermöglichte uns die Bildgebung eine annähernde Lokalisierung der Verzweigungspunkte. Diese Arbeit zeigt das Potenzial der Verwendung von STM/nc-AFM als ergänzende Technik für die strukturelle Identifizierung von Kohlenhydraten.

Contents

Abstract (English/Deutsch) **i**

1 Introduction **1**

2 Scanning tunneling microscopy - theoretical and experimental background **7**
- 2.1 Quantum tunneling 7
- 2.2 STM working principle 9
- 2.3 STM manipulation techniques 11
- 2.4 STM tip functionalizations and high resolution techniques 14

3 Non-contact atomic force microscopy - theoretical background and device realization **21**
- 3.1 AFM, nc-AFM and combined STM/nc-AFM 21
- 3.2 4 K STM/nc-AFM setup design 27
- 3.3 4 K STM/nc-AFM noise and performance optimization 31
- 3.4 Pauli repulsion imaging 39

4 On-surface reactions of thiophene functional groups **45**
- 4.1 Tetracenothiophene on Cu(111) 46
- 4.2 Electric field driven local reaction 48
- 4.3 Identification of the reaction product 51
- 4.4 Mechanism of the two-step reaction 55
- 4.5 Changes of the electrical conductance 57
- 4.6 Conclusions 62

5 Hyperthermal reactions of Reichardt's Dye **63**
- 5.1 Electrospray ion beam deposition (ES-IBD) 64
  - 5.1.1 Electrospray Ionization 65
  - 5.1.2 Experimental realization 65
  - 5.1.3 Soft landing and reactive landing 66
  - 5.1.4 Vacuum suitcase 66
- 5.2 Reichardt's Dye - model system and sample preparation 67
- 5.3 Soft landing of RD 69
- 5.4 Reactions induced thermally 71

5.5 Reactions induced by hyperthermal collisions 74
5.6 Conclusions 76

6 Carbohydrates on metal surfaces **79**
6.1 Structural complexity of glycans 80
6.2 Methods in the structural analysis of glycans 83
6.3 Oligomers of mannose as a model system 85
6.4 Linear pentamers on Cu(100) 85
6.5 Linear pentamers on Cu(111) 87
6.6 Analysis of the linear man5mer topography 88
6.7 Branched hexamers on Cu(111) 91
6.8 Conclusions 93

7 Summary and outlook **95**

Bibliography **101**

List of figures **123**

List of tables **127**

List of publications **129**

List of acronyms **131**

Acknowledgements **135**

1 Introduction

The structural identification of organic molecules has been a significant challenge since the early days of modern chemistry. At first, chemical analysis was performed qualitatively by mixing the analyte with various reagents that react selectively with atoms or functional groups, resulting in the formation of distinct products. This approach allows for the determination of specific features present in the analyte. For example, an addition of ammonia can be used to detect copper(II) ions, as together they form complexes of a characteristic blue color [1]. The field of analytical chemistry, first focusing on inorganic compounds and small organic molecules, in time progressed towards more advanced structures, including biologically relevant systems [2]. Nevertheless, the basic qualitative approach was not capable of facing advanced challenges like solving the structure of DNA, which took almost 100 years after the initial discovery of DNA and was accomplished with X-ray crystallography [3]. Thus, classical methods, such as the aforementioned qualitative analysis, had to be replaced with advanced, instrumentalized approaches that rely on the interaction of the analyte with electromagnetic radiation, non-destructive probing and advanced mathematical analysis. These techniques are now routinely used in many fields, including biochemistry [4], organic electronics [5] and food industry [6].

Most widely used instrumental methods of structural analysis of organic molecules include vibrational spectroscopies, diffraction techniques and nuclear magnetic resonance spectroscopy (NMR). Vibrational spectroscopies, such as infrared (IR) and Raman spectroscopies, rely on the inelastic scattering of electromagnetic radiation on the electron cloud of the specimen [7]. The majority of the interaction of photons with the investigated systems occurs through elastic (Rayleigh) scattering, where the adsorbed and emitted photons have the same energy. A small part of photons undergoes the inelastic scattering and they lose or gain an amount of the energy related to the spacing of vibrational and rotational energy levels [7], [8]. A spectrum can be recorded that carries information about the whole set of vibrational levels of the system, allowing for a determination of the specimen's structure. Moreover, vibrational spectroscopies can be used to identify analyzed substance with high certainty by comparison with existing entries in the database, as the vibrational spectrum is unique for each system.

Diffraction techniques profit from the wave-particle duality of photons [9], electrons [10] and neutrons [11], which, in form of a beam, diffract on the crystalline structure of the sample.

The intensity and angles of the diffracted beams carry information about the crystallographic structure of the system. The diffraction patterns can be both used to identify the specimen by comparison with the existing entries in the database and to elucidate a three-dimensional structure of the system: positions of the atoms, their type and connectivity [12]. The major requirement of all diffraction techniques is the crystallinity of the sample, however not all organic molecules can be crystallized. A notable example of organic structure determination with diffraction techniques is the aforementioned example of X-ray crystallography studies of the DNA structure [3].

A possibility to elucidate the structure of organic molecules regardless of their ability to crystallize is provided by NMR. Atom nuclei with non-zero spin exhibits degenerated spin states (for example +1/2 and -1/2 for a hydrogen proton). In presence of strong, constant magnetic field the spins are orienting themselves parallel or anti-parallel to the direction of the external field, which leads to an energy difference ΔE between two degenerated states. An additional, significantly weaker electromagnetic radiation is inflicted on the sample and if its frequency matches ΔE, the radiation will be absorbed and the spin will flip [13]. Afterward, it returns to the original state and emits radiation of the frequency corresponding to ΔE, which is recorded in NMR. The frequency of this signal not only depends on the type of probed nuclei but also on its electronic environment, as surrounding electrons also react to the applied magnetic field and can shield the nuclei. Therefore, the NMR signal also carries information about the connectivity of the atom, as well as surrounding atoms and functional groups, so it can be used to determine the structure of an investigated molecule [14]. Such a determination usually requires subsequent NMR measurements that focus at different components of organic molecules [15]–[17], such as hydrogen protons or ^{13}C atoms [18]. The amount of the analyte required for such a procedure increases with the size of the molecule and full structural identification might not be possible, especially for biomolecules that exhibit long, polymerized structure and are available only in limited quantities [19]–[21].

An approach alternative to a variety of spectroscopic and diffraction methods is offered by microscopic techniques. Instead of acquisition and analysis of convoluted patterns, spectra or spectroscopic "fingerprints" associated with specific structural features, microscopy techniques acquire real space images of investigated objects, starting at macroscale entities and finishing at single organic molecules and atoms. The spatial resolution of basic types of optical microscopy, which rely on the interaction of the imaged object with far-field photons of visible light, is limited by the Abbe diffraction limit (theoretically 250 nm for photons with 500 nm wavelength) [22]. Although this is sufficient for the observation of single cells [23], it is still far from the resolution required for the observation of single organic molecules (nm and sub-nm regime). The diffraction limit can be surpassed with more sophisticated types of optical microscopy, like stimulated emission depletion [24] or near-field scanning optical microscopy [25]. With these techniques, the resolution can be further improved to ~20 nm, which allows for the direct observation of the inside of cells [26], while still being unable to probe in real space the inner structure of single organic molecules. Electron microscopy is based on the interaction of the investigated object with far-field electrons in the form of the incident electron beam. The resolution of scanning electron microscopy (SEM), ~1 nm [27], is nearly sufficient to image molecular structures. The transmission electron microscopy (TEM) can resolve the features below 1 Å [28] for inorganic systems, which, for example, can be used to image single atoms of crystalline structures [29]. The usability of TEM for imaging of organic systems is limited, as increasing the resolution of TEM requires higher electron beam energy that will damage or destroy organic molecules before single bonds and atoms can be resolved [30]. The structure of biologically relevant organic molecules such as proteins can be identified with transmission electron cryomicroscopy (CryoTEM). In this technique, the molecules and particles are immobilized in vitreous ice that doesn't diffract the electron beam as strongly as crystalline ice and keeps the specimen in a state close to its native state (in contrary to high vacuum in the standard TEM column) [31]. The identification of structure requires the acquisition of a huge number of projection images of identical molecules acquired with small, non-damaging electron doses. The molecules are suspended in amorphous ice film in random orientations and by using advanced software, the images can be aligned, averaged and combined into a three-dimensional structural model of the molecule [32]. Despite the superior capabilities of TEM and its subtypes, direct observation of the structure of single organic molecules with atomic precision is yet to be achieved with TEM. The technique, which already attained this goal, is scanning tunneling microscopy (STM) and its combination with non-contact atomic force microscopy (nc-AFM).

Since its invention in 1981 [33], STM has become established as one of the most powerful tools in fundamental surface science [34]. It utilizes the quantum tunneling effect occurring between the sample and tip electrodes to probe the local density of states (LDOS) of the investigated system. STM operates in sub-nm range, as the tunneling effect is laterally confined in a small area defined by the last atoms of the tip apex. STM can be used to map the spatial distribution of LDOS and yields atomic-scale images of surfaces and surface adsorbates, including organic molecules. Moreover, it offers the possibility of performing atomically precise manipulations of adsorbates, either by utilizing the electric field and tunneling current or by interaction with the tip electrode. The experiments performed with STM in sub-nm scale often reveal the quantum nature of physical phenomena, such as conductance quantization [35] or single spin magnetism [36]. Further development of STM, including lowering the operational temperatures to mK range [37], [38], introducing magnetic fields [39], [40] and coupling the tip-sample junction with an optical readout [41], [42] expanded already broad possibilities of this technique.

STM can be used to identify the chemical structures on the basis of their appearance in the real space imaging [43]. As it probes LDOS, it is capable of recording high-resolution images of molecular orbitals such as surface modified HOMO and LUMO. The elucidation of molecular structures is possible by mapping the orbitals and comparing the experimental results with the simulations. Direct observation and identification of organic structures can be achieved with STM techniques that rely on modifying the STM tip apex with semi-fixed molecules and particles, like CO and H_2. Terminating a tip with a particle with an additional degree of freedom introduces the possibility of dynamically changing the junction geometry in response to short-range forces. These changes are detectable in the conductance signal, so terminations with an additional degree of freedom act simultaneously as a force detector and transducer [44]–[47]. As localized electrons yield stronger repulsive potential than the electrons delocalized in orbitals, they are detected in "force-conductance" STM images as features of higher intensity. Therefore, with this type of imaging, looking through the electron cloud, directly into the chemical structure of organic molecules, is possible in real space. This approach is further refined with utmost precision and control by nc-AFM, where the short range forces can be detected directly, without mixing of the mechanical and electrical signals [48]. The ability of combined STM/nc-AFM devices to perform direct structural identification of organic molecules is relevant for both fundamental science and industry. One of the examples of application of the STM/nc-AFM imaging with submolecular precision is presented by Schuler *et al.* [49] (Fig. 1.1). In their research, they identified the chemical structures of a variety of heavy oil molecules encountered during oil processing, providing information relevant to the oil industry and geology. The potential applicability of STM/nc-AFM in the non-fundamental studies can possibly bring the attention of scientists from various fields to the field of scanning probe microscopy (SPM).

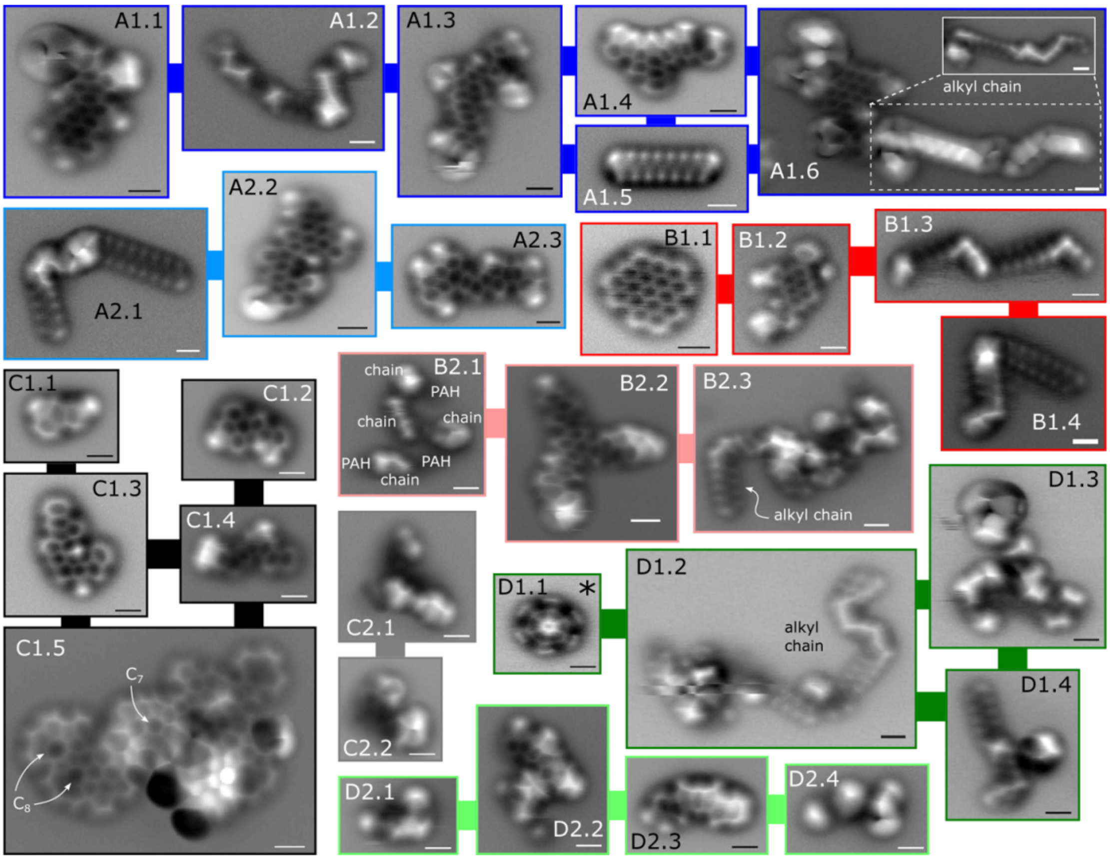

Figure 1.1 Structures of organic molecules encountered in the oil processing resolved by nc-AFM (Schuler *et al.* [49]).

In this thesis, we use the STM/nc-AFM manipulation and imaging techniques to identify the chemical structures of various organic molecules in three distinct projects. In the first two chapters, the concepts and working principles of both STM and nc-AFM are introduced, together with examples of available manipulation and imaging techniques realized by these instruments. Furthermore, in the second chapter, a practical realization of a combined STM/nc-AFM device is described. In the first research project, we use STM/nc-AFM to follow an on-surface desulfurization reaction of a thiophene moiety embedded in an organic molecule. We reveal a new reaction mechanism, which allows controlled dissociation of single bonds in the thiophene group, leading to strong bonding between the molecule and an underlying copper substrate. In the second project, we utilize the STM/nc-AFM imaging to identify new, stable conformations of the Reichardt's Dye molecule obtained by hyperthermal depositions realized with the electrospray ionization-beam deposition technique (ES-IBD). In the last chapter, we present the preliminary results of an investigation of carbohydrates on metal surfaces. In this project, we aim to obtain, with the help of the STM/nc-AFM imaging, information about the branching of oligosaccharides. If the ability to localize the branching points is proven and if the number of monosaccharide units in each branch can be determined, STM/nc-AFM may become a complementary structural analysis technique in glycomics and biochemistry.

2 Scanning tunneling microscopy - theoretical and experimental background

Scanning tunneling microscope (STM) was invented as an imaging tool of previously unprecedented resolution [33]. Its working principle is based on quantum tunneling effect, where electrons can tunnel through a classically impenetrable potential barrier. The flux of the tunneling electrons is exponentially dependent on the barrier width, which determines the lateral confinement of the effect in the STM tip-sample junction. The high confinement of the tunneling effect in the STM junction is the origin of the high resolution of this technique. The STM tip is piezoelectrically controlled with sub-*nm* precision and allows one to probe the local electronic properties of surfaces and surface adsorbates, including direct imaging of the atomic structure [50]–[52]. Moreover, not only can the STM be used to probe the investigated surface, but also to interact with it, which raises the possibility of performing precise atomic manipulations [53]. The possibilities provided by STM allow for the elucidation of processes like chemical reactions [54] or molecular movement [55], [56] at the atomic scale in real space, significantly improving our understanding of physical phenomena in various areas of science.

In this chapter, the quantum tunneling effect will be introduced in the context of a basic STM instrument. We will give the examples of manipulation techniques that represent the possibilities of influencing the state of the adsorbates with the STM tip: lateral and vertical manipulations, desorption, diffusion, switching, bond breaking and chemical reactions. The effects of tip functionalizations on the spatial resolution of the STM imaging will be described, including pentacene, hydrogen and CO tip terminations. Presented techniques allow resolving both the electronic and atomic structure of adsorbed organic molecules, as will be shown in the illustrated examples.

2.1 Quantum tunneling

According to classical physics, an object with an energy lower than the potential energy of a barrier is not able to pass through that barrier. The probability of finding the object before the barrier is equal to 1, and equal to 0 in the barrier and beyond. If the object is sufficiently small (for example an electron), its behavior is governed by the laws of quantum mechanics and the barrier is penetrable through a process called quantum tunneling [57], as depicted in Fig. 2.1.

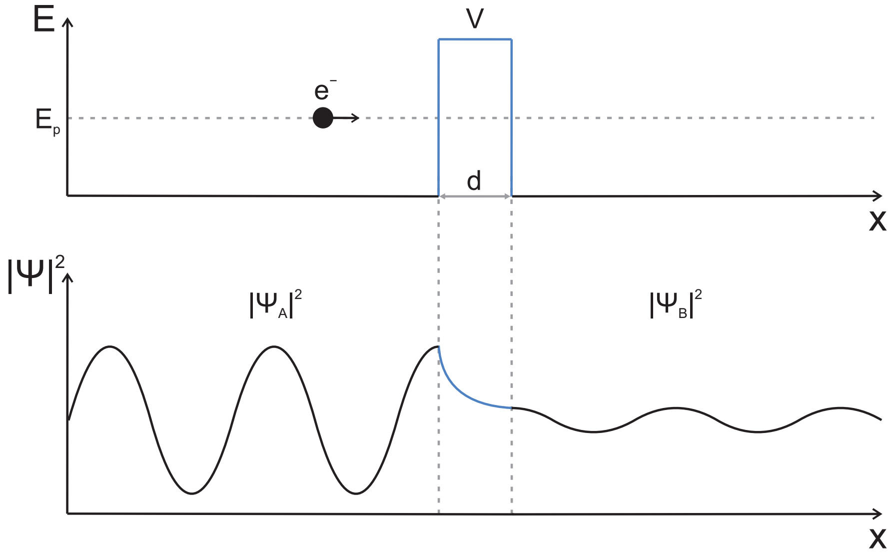

Figure 2.1 Elastic quantum tunneling through a rectangular barrier. Top panel: the energy of a particle moving towards a barrier. Bottom panel: probability of encountering the particle on both sides of the barrier.

Solving one dimensional Schrödinger equation for a potential barrier of width d and height V yields the following relation between the wavefunctions of an electron on both sides of the barrier:

$$\psi_B = \psi_A \cdot e^{-\kappa d}, \tag{1}$$

where ψ_A and ψ_B are the particle's wave functions on the left (in front of) and right (behind) of the barrier. κ is the decay constant $\kappa = \sqrt{2m(V-E)}/\hbar$, where m is the mass of the particle and $\hbar$ is the reduced Planck's constant. According to this relation, the amplitude of the wave function after tunneling through the barrier decays exponentially with the barrier width d, yielding a lower probability amplitude $|\psi_B|^2$, but having no influence on the energy of the particle ($E_A = E_B$, elastic tunneling) [58].

The simplest experimental realization of a tunneling effect comprises two metal electrodes separated by a vacuum gap, with a bias voltage applied between them, equivalent to a plate capacitor with separation of the plates in the Å - nm range. A flux of electrons, which is the tunneling current, occurs across the plates and its value depends on the applied voltage, available electronic states, separation of the electrodes and their size. If one of the plate electrodes is replaced with a metal tip, then the tunneling current flows only through the small part of the second electrode. Due to the exponential decay of the wave functions of electrodes, the tunneling barrier becomes wider when laterally farther from the tip apex. This lateral confinement of the tunneling effect is the origin of the high spatial resolution of the STM technique and it allows probing of the local electronic properties of the sample.

2.2 STM working principle

The STM was invented by Gerd Binnig and Heinrich Rohrer [33], who utilized the tunneling effect to create an alternative to other microscopy techniques existing at that time. For the invention, they were awarded a Nobel prize, which was shared with Ernst Ruska (for the invention of the electron microscope) [59].

Instead of imaging certain areas of the sample simultaneously, as in methods that rely on the interaction of the sample with far-field electrons (electron microscopy) or far-field photons (optical microscopy), STM is used to locally probe the properties of investigated samples with a tunneling effect spatially confined to the tip-sample junction. Therefore, the STM images are acquired by raster scanning the surface (Fig. 2.2).

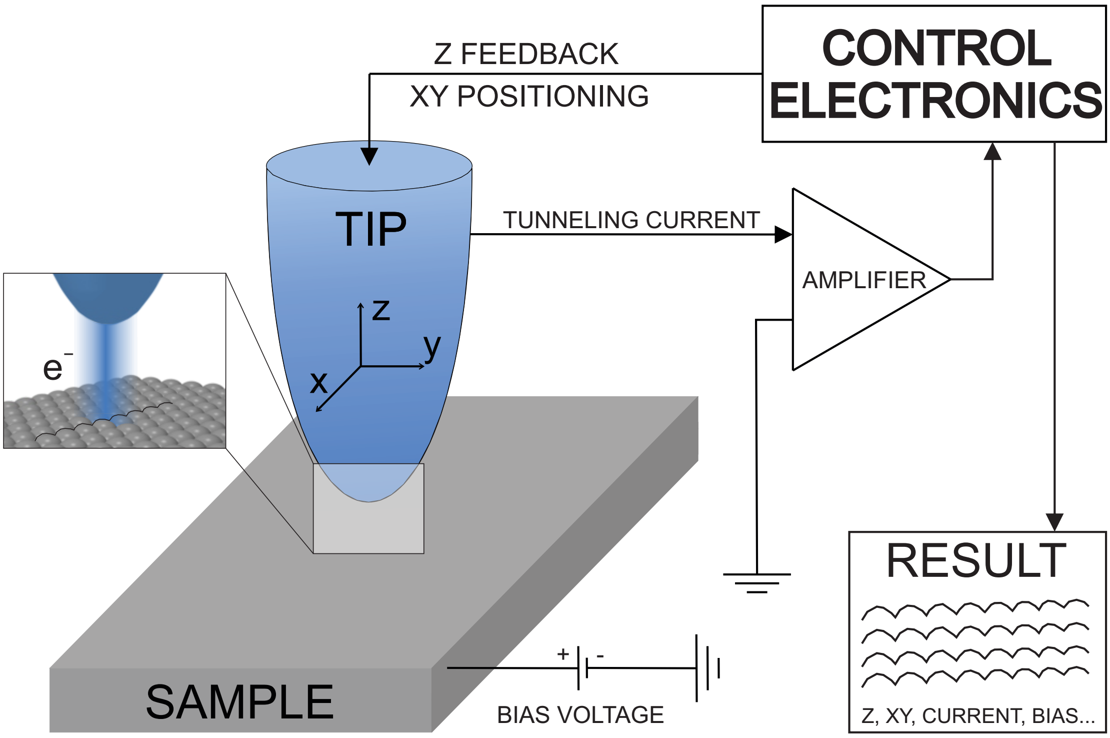

Figure 2.2 Schematic of the STM device, presenting crucial components of the device.

A piezoelectric scanner is used to control the tip displacement with sub-nm precision in the *Z* axis, as well as in the *XY* plane. Properties of the surface and surface adsorbates are probed by detecting the tunneling current that is present for small tip-sample distances if a bias voltage is applied between the tip and the sample. The STM can be operated in two basic modes [60]. In constant current mode, the constant value of the tunneling current is maintained by adjusting the distance between the tip and sample. The set value of the current is ensured by a feedback loop that counteracts the changes in the current by applying a voltage to the Z component of the scanner piezo. The current value, as well as the applied bias voltage and feedback loop parameters, are determined by the user. As a result of constant current imaging, a Z displacement image is acquired, which can be interpreted as a topography for the surfaces of uniform density of states, e.g. without adsorbates and surface states. Apart from the distance and the bias voltage, the value of the tunneling current and in turn the Z displacement depends on the wave functions of both the tip and the sample [34], [60]. The images of non-uniform systems, such as metals with surface states [61], [62], organic adsorbates on metals [63] or atomically thin insulating layers deposited on metal surfaces [64], cannot be interpreted as an accurate topography, as the object with the same physical height might appear differently due to a difference in electronic structure. Therefore, the tip in constant current scanning mode follows the contour of the constant density of states that arises from the convolution of the sample and the tip states [60].

In the second operation mode, constant height mode, the vertical position of the tip is not changed during the data acquisition [60], [65]. The starting position of the tip is defined by the user at a specific area of the sample. This technique yields images of the current as a function of the lateral position of the tip for given vertical position of the tip and the bias voltage. This operation mode can be used to probe the changes of LDOS at a fixed tip-sample distance, rather than to follow a contour of the constant density of states. It is normally used to investigate known areas and adsorbates, as without any Z feedback control the tip can come to direct contact with the sample and crash [66]. Thus, the imaging of unknown areas of samples should first be performed in constant current mode. Moreover, higher scanning speeds are possible as the resolution of the technique is not additionally limited by the time constants of the feedback loop [66].

The tunneling current I can be described with Tersoff and Hamman's approximation [67], [68]. Assuming a monoatomic tip termination with s-wave character (radially symmetric electron density), 0 K temperature, similar work function ϕ of the tip and the sample material, and that the majority of the tunneling current flows through the single atom of the apex (due to the exponential dependence on the tip-sample distance, equation 1), the following relation is obtained:

$$I \propto \frac{2\pi eU}{\hbar}\rho_s(E_F), \tag{2}$$

where U stands for the applied bias voltage and $\rho_s(E_F)$ is the LDOS at (E_F) of the sample at the position of the tip [60]. The first derivative of the current, dI/dU, also called differential conductance, follows the relation:

$$\frac{dI}{dU} \propto \frac{2\pi e}{\hbar}\rho_s(E_F + eU). \tag{3}$$

As the dI/dU depends linearly on ρ_s and is independent of used bias voltage U, LDOS at certain energy U can be measured directly. This relation is the base of scanning tunneling spectroscopy (STS), which can be used to record a spectrum of the energy states of the system.

The approach developed by Tersoff and Hamman does not take into account the properties of the tip. In reality, the tunneling current (so the resolution of the STM techniques), depends also on the shape and the composition of the tip apex. An intentional tip modification may lead to improved resolution of the imaging, which will be discussed in section 2.4. Conducting measurements of high quality requires a tip apex that fulfills the requirements of the experiment and needs to be carefully prepared to acquire the desired feats.

2.3 STM manipulation techniques

One of the unique features of STM, as compared to other types of microscopy, is its ability to influence the investigated system in a controlled, precise way. Although both far-field photons and electrons do interact with the sample, they rarely lead to any changes in the imaged systems and even if they occur, they usually have a destructive and uncontrolled character [30], [69]. All of the stimuli possible to exert with the STM tip are localized and can be used to induce local interaction. Three main "tools" are available for the STM manipulation in standard setup: mechanical forces (repulsion and attraction), an electric field (as the tunneling junction is capacitative) and tunneling electrons [53]. All three stimuli can be used to perform manipulations, often in a combined manner.

The first group of manipulation techniques considered here comprises lateral manipulations, also called "soft", as the manipulated object does not undergo any structural changes nor desorb from the surface [53]. They are used to change the position of the adsorbate or the adatom on the surface, for example in order to assemble structures with atomic precision. Lateral manipulations can be performed by approaching the tip closer to the adsorbate, where forces between it and the tip are now sufficiently high to displace the adsorbate towards the desired position. Lateral displacements can be attained with *pulling, pushing* and *sliding*, named due to the similarity to classical concepts [53]. Prominent examples of structures obtained via lateral manipulation include the letters IBM written with Xe atoms [70], a rewritable atomic memory made with vacancies [71] and the quantum corral [72], [73] (Fig. 2.3).

The displacement of the adsorbate on the investigated surface may be carried out not only through the means of lateral, but also vertical manipulations. The main feature of these techniques is the formation of a stable contact of the adsorbate with the tip apex, which can be utilized to pick the adsorbate from the surface. The process of a tip-adsorbate contact formation may occur due to the higher affinity of the adsorbate to the tip, as in the case of picking up single Xe atoms [74]–[77] or through the electron or the electric field assisted processes, such as the pickup of a CO molecule from metal surfaces [78]–[80]. The adsorbate might be lifted from the surface completely, moved on the tip apex to another lateral position

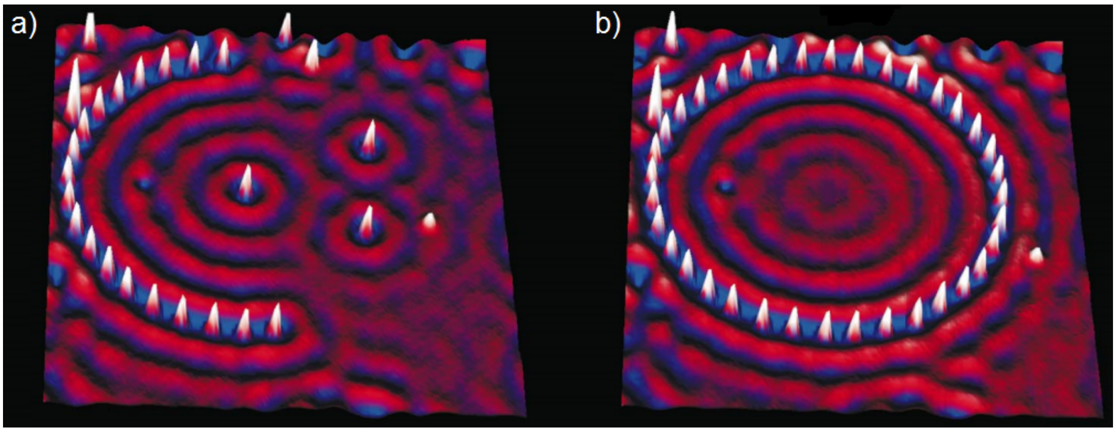

Figure 2.3 Construction of a quantum corral structure using Ag adatoms on the Ag(111) surface. a) Construction process in progress. b) Finished structure. Circular pattern is a confined standing wave of the Ag(111) surface states (modified from Hla *et al.* [73]).

and deposited back on the surface. The acquired effect is identical to lateral manipulations, but its usability is much greater, as an object of interest can be moved across and around various obstacles, such as surface steps or other, bigger adsorbates. One of the notable examples of using vertical manipulation techniques is the movie "A Boy And His Atom", each frame of which was composed of single CO molecules placed at desired positions [81]. Another application of vertical manipulation originates in the suspension of an object between the tip and sample electrodes, which occurs whenever the contact with the tip is maintained without breaking the contact with the sample. It can be used to selectively pass the current through a suspended object, for example in order to measure conductance through single molecules [44], [82]–[84]. The transfer of adsorbate to the tip can be done with an intention to keep it at the tip apex. Tip functionalizations can have a substantial effect on the achievable resolution of STM imaging. One example of such an enhancement due to the tip functionalization is the Xe pickup from Cu(211) [75]. The influence of various tip functionalizations on the resolution will be discussed in section 2.4.

The possibilities of influencing adsorbates are not limited to "soft" manipulations. The state of the adsorbate can also be modified in a variety of ways, ranging from the activation of the desorption to inducing changes of the chemical structure [53]. An example is diffusion activation. In comparison to the lateral displacement of an adsorbate, diffusion occurs in a pseudo-random manner (on available pathways) and does not require any constant interaction with a tip. It does require a destabilization of the adsorbate in its original position or geometry and can occur due to the population of the antibonding orbitals of the adsorbates [85], [86] or due to the excitation of vibrational modes with tunneling electrons [87]–[89]. Another example is STM-induced desorption. Unlike in vertical manipulations, desorbed atoms or molecules leave the surface without attaching to the tip apex. This type of process is usually induced by the tunneling current, as in the case of hydrogen desorption from Si(111) [90], [91]. Other examples include desorption of CO from Cu(111) [80], NH_3 from Cu(111) [92] and chlorobenzene from Si(111) [93]. The desorption of hydrogen can also be induced by a mixed tunneling current - electric field effect [94]. In this case, the width of the energy barrier is reduced by the electric field. Together with the excitation caused by the electrons, it allows for the tunneling desorption of hydrogen

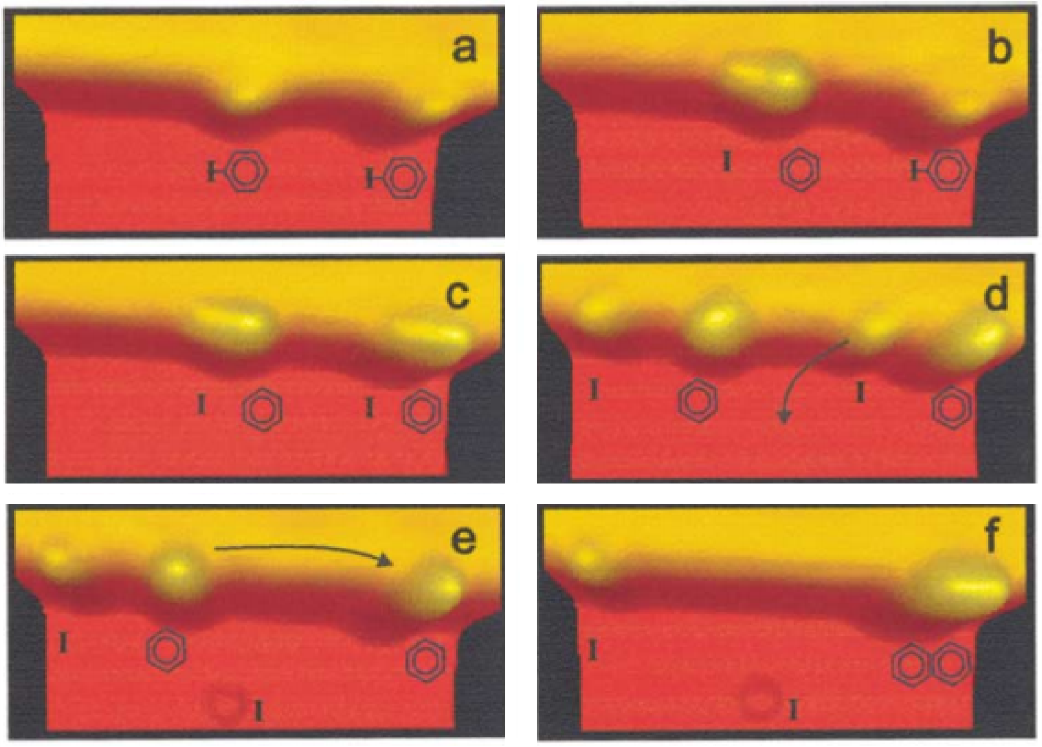

Figure 2.4 STM images presenting each step of an on-surface Ullman reaction. **a)** Two intact iodobenzene molecules adsorbed on a step edge of Cu(111). **b)** and **c)** Two C-I bonds dissociated. **d)** Removal of the I atom from the step edge. **e)** Lateral manipulation of two benzene molecules. **f)** Two benzenes molecule joined into a naphthalene molecule (Hla *et al.* [54]).

With STM, not only it is possible to affect the chemistry of an adsorbate with respect to the surface, but also to induce internal structural changes of the molecules. If the change is reversible on the same pathway it is called a switch [53]. The examples of switching include cis-trans isomerization induced with an electric field [95], [96] or tunneling electrons [97], [98]; conformational switching induced with an electric field [99], direct electron injection [100], [101] or electron injection via surface states [102]. The non-reversible changes of the internal structure of an adsorbate include bond breaking and formation, i.e. the chemical reactions. Local dissociation of single bonds with STM has been achieved for many molecules such as O_2 [103]–[106], H_2S, D_2S [107], H_2O [108], $(CH_3S)_2$ [109] and for bigger molecules as well [110], [111]. Apart from bond breaking, STM can also be used to form chemical bonds in a local and controlled manner. Therefore, STM can image and identify the products of globally induced chemical reactions (e.g. thermally induced [112]–[115]), but also follow the in-situ synthesis of molecules and structures. The prime example of an on-surface chemical reaction realized step-by-step with an STM is the synthesis of naphthalene from two iodobenzene molecules (Ullman reaction), realized by Hla *et al.* [54]. This particular study perfectly illustrates the capabilities of STM, as it utilizes different manipulation techniques in order to obtain a desired molecular structure. In the first step, depicted in Fig. 2.4 a), the two iodobenzene molecules adsorbed at the step edge of Cu(111) are imaged. The tip is then positioned above one of the molecules. The dissociation of the C-I bond is realized separately for both molecules by injection of the tunneling electrons (images b) and c)). One of the I atoms is picked up with the tip and dropped on the next terrace, as indicated by an arrow in the image d). This is followed by a lateral manipulation of the benzene ring along the step edge towards the second benzene ring, realized by the *pulling* movement, as depicted in e) and f). The formation of a chemical bond between the two benzene rings can be activated by the injection of electrons with a 0.5 V bias. The bond formation has been confirmed by laterally pulling the benzene rings together, whereas before the reaction they could be separated.

The spectrum of manipulations possible with an STM is of course much broader than the short overview covered in this section. For more details the reader is referred to references [53], [116], [117].

2.4 STM tip functionalizations and high resolution techniques

The initial experiments concerning manipulations of single Xe atoms on metal surfaces revealed that the resolution of STM imaging techniques can be enhanced by modifying the tip apex [75], [77]. Tip functionalizations are now a well-established part of the STM toolbox, providing better resolution for imaging metal surfaces [75], thin insulating layers [118] and organic structures [101], [119], [120]. In metals, the Fermi sea of electrons is equally distributed along the structure and in insulators, the electrons are localized on atoms (like in the case of thin layers of NaCl, where charged Cl^- ions are seen as bright protrusions in positive bias voltages [118], [121]). The interpretation of high-resolution images of the organic structures and single molecules has been challenging because the density of states is not associated with molecular structure in a straightforward manner. Therefore, the high-resolution STM imaging of molecules usually yields images corresponding to the surface-modified molecular orbitals. In this section, the STM techniques allowing such imaging will be shown, as well as methods that resolve molecular structure.

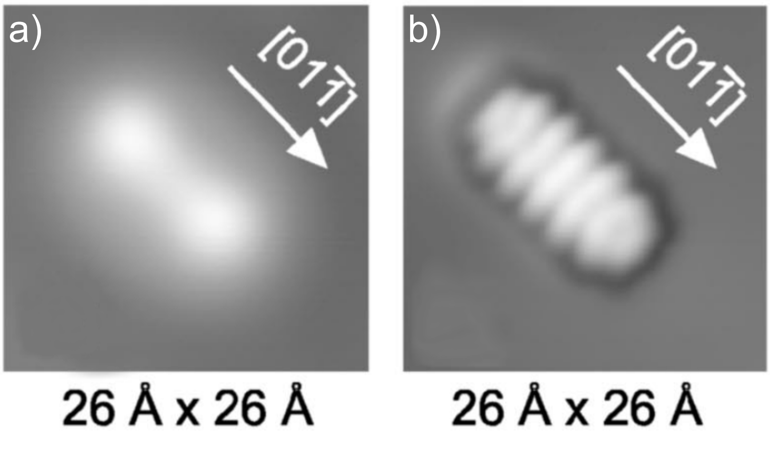

Figure 2.5 **a)** Pentacene molecule adsorbed on Cu(111). **b)** The same molecule imaged with pentacene-terminated tip (Lagoute *et al.* [63]).

The simplest type of tip functionalization that leads to an improved resolution, are single atom tip terminations, where the atom is of a different type than the tip composition. As already mentioned, the first experiments were done with Xe atoms and lead to significant improvement of the resolution for the imaging of the Cu(211) surface. Also, functionalization with a single Cl atom leads to improved resolution of the NaCl(100) layer [118]. This effect has been attributed to highly localized *p*-wave states of the chlorine terminated tip [118]. A similar explanation can be applied to the Xe terminated tips.

The study utilizing pentacene terminated tips has proven that organic molecule termination can also lead to an improved resolution. The pentacene molecule imaged on Cu(111) with a pentacene-terminated tip reveals five distinct lobes that resemble the lowest unoccupied molecular orbital (LUMO) of an isolated pentacene molecule (Fig. 2.5) [63]. Using the same functionalization, pentacene molecules decoupled from the metal substrate have also been imaged on NaCl(100) [122] (Fig. 2.6). Separation of the pentacene molecules from the metal surface with this insulating layer allowed for direct imaging of individual molecular orbitals. With a pentacene-terminated tip, near perfect agreement with theoretical calculations of the isolated molecular orbitals was obtained, for both the HOMO and LUMO, at -2.4 V and 1.7 V respectively. Other examples of organic molecule tip terminations include structural derivatives of pentacene (anthracenodithiophene) [101], [102], perylene [123] and C_{60} [124], [125]. Improved resolution can be attributed to changes of the character of the tip, as functionalization with organic molecules leads to an extension of hybridized orbitals (e.g. sp, sp^2, sp^3) in the Z axis [126]–[128].

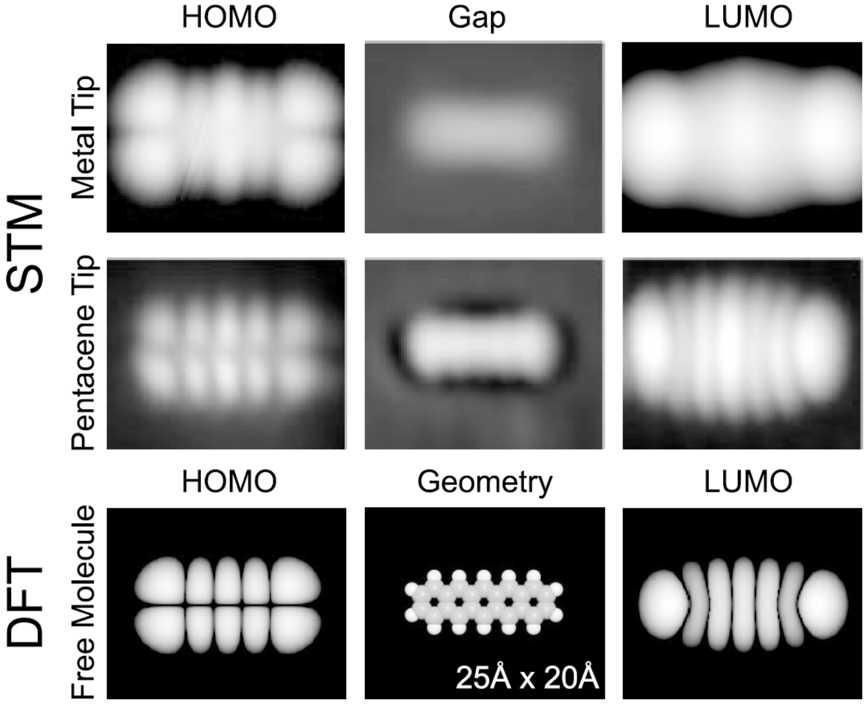

Figure 2.6 Orbital resolution images of pentacene on NaCl(100) layer. The STM images presented in the left column have been recorded at -2.4 V, in the right column at 1.7 V. The result of the DFT simulations of HOMO and LUMO states of an isolated pentacene molecule are depicted in bottom row (Repp *et al.* [122]).

Another approach to tip termination involves introducing additional degrees of freedom into the tunneling junction [47]. One of the most prominent cases is scanning tunneling hydrogen microscopy (STHM), which utilizes hydrogen terminated tips [44]. At cryogenic temperatures, H_2 is the most abundant residue that accumulates at the cold parts of the STM, including the sample and the tip. It can be removed by a limited warm-up of the instrument to around 50 K. If the sample or the machine is kept cold for an extended period of time, the accumulation of H_2 becomes high enough to cause spontaneous hydrogen tip functionalization, which can lead to increased imaging resolution. It was found that bringing the hydrogen-terminated tip close to the organic adsorbate (virtually to the Pauli repulsion regime) leads to a drastic change of contrast, where the obtained topography does not resemble LDOS, but the molecular structure of the adsorbate [46], as depicted in Fig. 2.7. The STHM imaging mechanism relies on the response of the particle decorating the tip to short-range forces. Slight changes of the particle's position in relation to the tip (an alteration of the junction geometry) are translated into changes of the conductance *dI/dU* signal. Therefore, H_2 simultaneously fulfills the role of a force sensor and a force-conductance transducer [44]–[47]. As the signals originating from the changes of the electronic structure and geometry of the H_2 molecule intertwine in the conductance *dI/dU* channel, the technique provides molecular structure images only for systems that do not have distinct states around the Fermi energy E_F (i. e. the experiment has to be carried out in the range of vibrational energies of H_2, namely -50 mV - +50 mV [47]). Moreover, a high density of hydrogen on the surface can be perceived as contamination, as it will render other experiments harder or even impossible to carry out (e.g. IETS experiment in the energy range of the hydrogen features).

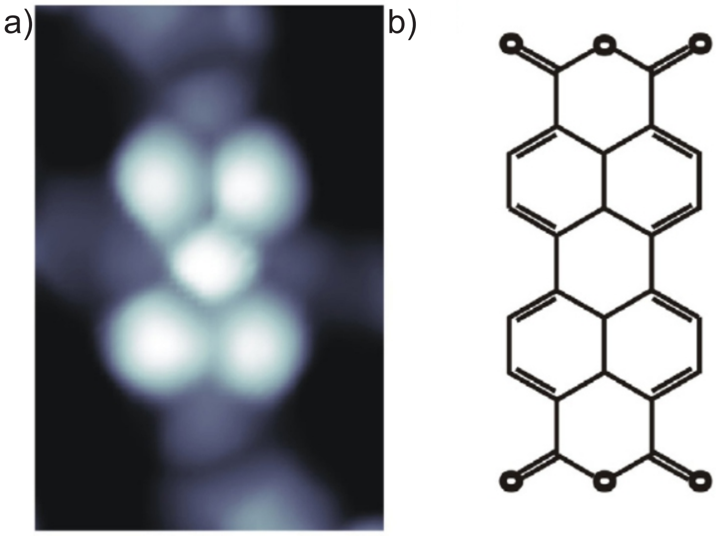

Figure 2.7 **a)** PTCDA molecule image with STHM technique. **b)** Chemical structure of PTCDA (Temirov *et al.* [44]).

Among various tip terminations, the carbon monoxide (CO) molecule has proven to be one of the most versatile. Due to its mechanical and electronic properties, it can be used to resolve the orbital structure and structural backbone of organic molecules. The CO molecule adsorbed at the tip apex is always oriented with the carbon atom attached to the apex and semi-free oxygen atom pointing out. This geometry yields horizontally oriented π orbitals extended in the Z-axis (p-wave character) [119], [129]. Tunneling through 5σ orbital and two degenerate π orbitals results in mixed s-p tip character, which can lead to an additional improvement in the imaging resolution for certain organic systems, like naphthalocyanine (Fig. 2.8), providing resolution similar to pentacene-terminated tips for pentacene and its analogs [119]. The mixed s-p tip imaging behavior has been analyzed in separate theoretical studies, confirming the observed effects [126].

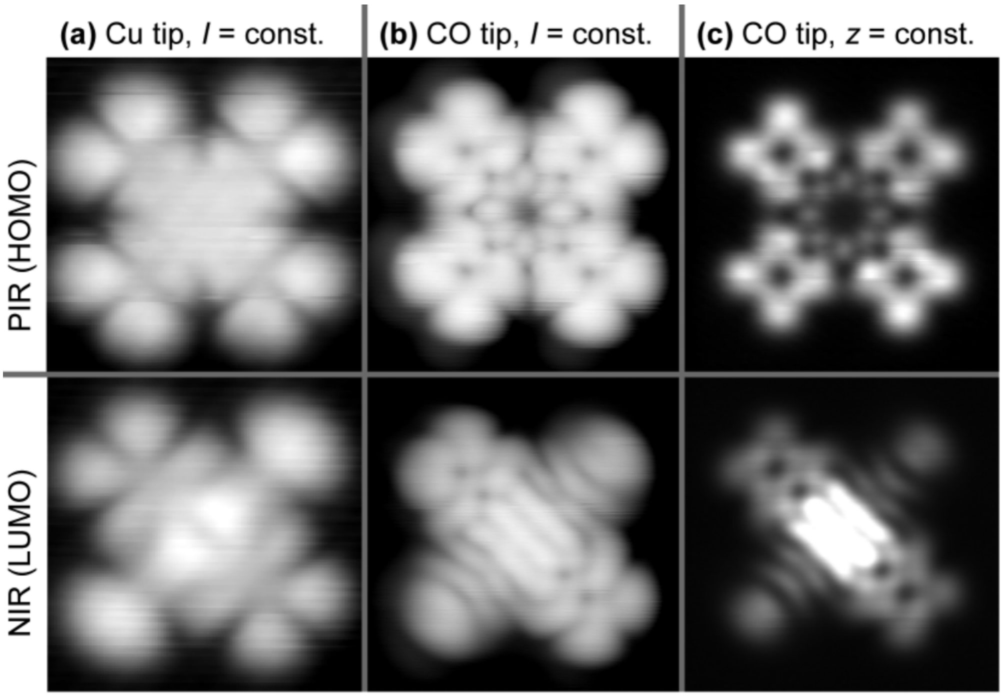

Figure 2.8 Effect of a CO-terminated tip on the imaging resolution of naphthalocyanine on NaCl(100). **a)** Constant current images of HOMO (-2.4 V) and LUMO (1.7 V) orbitals, acquired with a metal tip. **b)** Constant current images acquired with a CO-terminated tip. **c)** Constant height images acquired with a CO-terminated tip. (modified from Gross *et al.* [119]).

The mechanical properties of the CO molecule adsorbed at the tip apex are similar to properties of the H_2 molecule and it introduces an additional degree of freedom into the tip-sample junction. As already mentioned, it always adsorbs with the carbon atom stiffly attached to the apex and the oxygen atom extending into the junction. As the oxygen atom of the CO molecule is not stiffly attached to the tip, the whole molecule can vibrate in the hindered translational mode. This property is utilized in the inelastic tunneling probe technique, which allows imaging of the molecular structure [120], [130]. The CO molecule, adsorbed on the tip apex (as well as on the surface), exhibits vibration at distinct energy. Upon infliction of a force on the molecule, this energy is shifted. This effect can be utilized to detect the Pauli repulsion from the features of highly localized repulsive potential, like the carbon atoms of organic molecules. When the CO-terminated tip is close to those features, e.g. spectra **1**,**2**,**3**,**5**,**7**,**9** in Fig. 2.9 a), the Pauli repulsion results in dampening of the intrinsic vibration of the CO

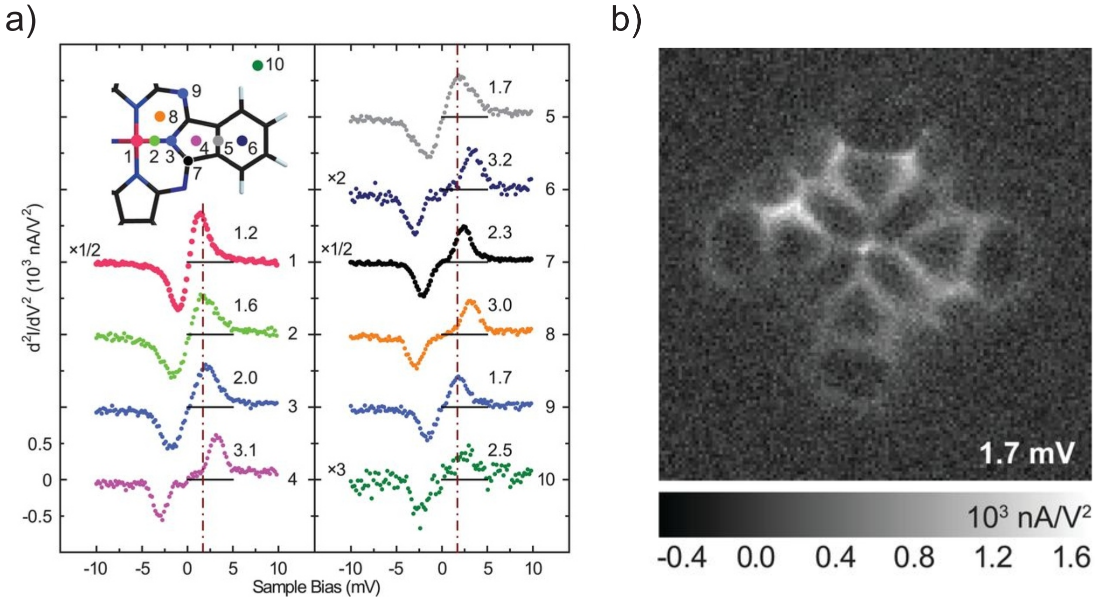

Figure 2.9 Principle of Inelastic Tunneling Probe imaging. **a)** Changes of the vibrational energies of the CO molecule placed at the tip apex. Color of the graph corresponds to point on the map, where the tip was positioned during the measurement. **b)** d^2I/d^2U map of cobalt phthalocyanine revealing its molecular structure (modified from Chiang *et al.* [120]).

molecule. This leads to lower vibrational energy that can be followed by inelastic tunneling spectroscopy. Mapping the changes of the vibrational energy of the CO molecule can result in the acquisition of an image representing the backbone structure of an organic molecule (Fig. 2.9 b)). The measurement itself is time-consuming and requires extraordinary stability. As a consequence, this technique might be difficult to implement in regular 4 K STM instruments [120].

As the CO-terminated tip behaves similarly to the H_2-terminated tip, a technique comparable to STHM can be realized with this tip termination, called bond resolving STM (BR-STM) [112], [113]. Analogously to H_2, CO can act as both a force sensor and transducer. The imaging is performed in the same way as in STHM, by recording the conductance *dI/dU* channel. BR-STM shares the same advantages and limitations as STHM (for example it will not yield an image of the organic structure of the adsorbate if it exhibits electronic states around E_F), however, BR-STM does not require flooding the measurement chamber with any gas, making the technique less invasive for both sample and the cryostat. Therefore, BR-STM is more preferable, as it does not pose a risk of making the sample unusable for other experiments.

The CO tip functionalization has been proven to provide extraordinary imaging resolution of organic molecules, for both imaging of orbitals and molecular structures. It has become one of the most widely used tip terminations in the field of STM. An additional factor that cemented its popularity, is its use in the Pauli repulsion imaging mode in the non-contact atomic force microscopy (nc-AFM), which can be carried out in combined STM/nc-AFM instruments. This technique allows imaging of the molecular backbone independently of their electronic structure, thus avoiding the issues of STHM and BR-STM. The concept, working principles and experimental realizations of nc-AFM, combined STM/nc-AFM, and the Pauli repulsion imaging will be described in the next chapter of this thesis.

3 Non-contact atomic force microscopy - theoretical background and device realization

The applicability and possibilities of STM can be expanded by combining it with non-contact atomic force microscopy (nc-AFM). At the time of the invention of STM, there was no technique, which allowed performing experiments on the surfaces of bulk insulators with a similar precision [131]. Existing devices, like stylus profilometer [132] or the scanning capacitance microscope [133] were able to obtain three-dimensional images of both conductive and insulating surfaces. The images were recorded with a vertical resolution below 1 nm and a lateral resolution above 100 nm, thus severely lacking the spatial precision of STM. In order to address this issue, atomic force microscope (AFM) was developed by one of the original inventors of STM [33], [131]. First AFM consisted of a diamond tip attached to the end of a flexible cantilever moved by a three-dimensional piezoelectric motor. The tip was placed in the proximity of the surface of the sample. A force arising from this proximity had a direct effect on the deflection of the cantilever. On its other side, the STM tip was used to track the motion of the cantilever with precision up to 10^{-4} Å. This setup was proven to image insulating surfaces with an unprecedented resolution [134]. Further development of the technique allowed AFM to achieve true atomic resolution, comparable with STM [135] as well as for combining it with STM, where a single tip was used for both the STM and AFM experiments [136].

In this chapter the working principle of nc-AFM will be presented, as well as the practical realization of a combined STM/nc-AFM instrument. Moreover, we describe in detail the Pauli repulsion imaging technique that allows for the imaging of the atomic structure of organic molecules with submolecular resolution.

3.1 AFM, nc-AFM and combined STM/nc-AFM

From the first design of Binnig [131], AFM developed in two different directions: conventional, industry-relevant AFM offering relatively easy operation based on the optical readout of the cantilever deflection and nc-AFM offering higher precision measurement, in modern versions

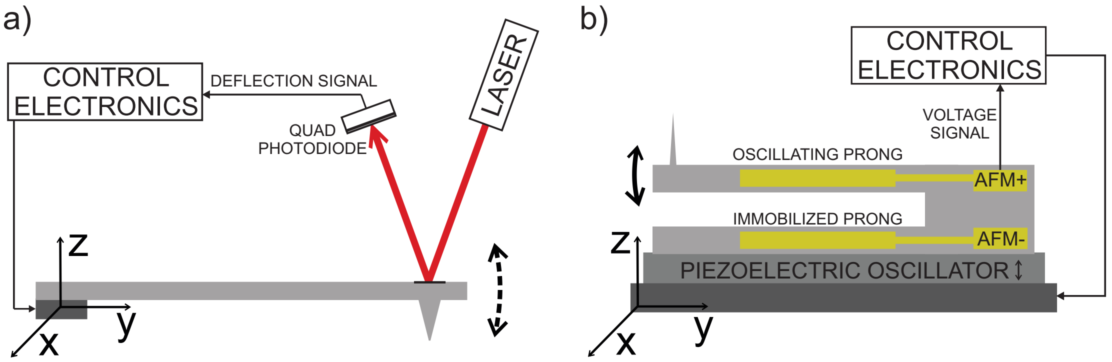

Figure 3.1 Two types of AFM. **a)** Scheme of AFM device with a laser deflection detection system. A laser beam hits the mirror surface placed at the end of a silicon cantilever and a reflected beam reaches the quad photodiode. The position of the reflected beam spot on the photodiode is dependent on the cantilever deflection, thus on the forces acting on the tip. **b)** Scheme of nc-AFM. A resonance oscillation of the quartz tuning fork prong is induced by a piezoelectric oscillator, which, due to the piezoelectric effect in quartz, generates charges, which are converted to a voltage signal of a frequency corresponding to the resonant oscillation of the prong. Upon inflicting any force on the tip, the spring constant of the prong (and therefore the resonance frequency) changes, which modifies the frequency of the outgoing voltage signal.

based on the piezoelectric read out of the movement of the sensor prong. The scheme of a basic design of the conventional AFM is depicted in Fig. 3.1 a). It consists of a silicon cantilever attached to a three-dimensional piezoelectric motor. The interaction between the tip placed at the end of the cantilever and the investigated surface results in the deflection of the cantilever in static operation mode or change of the parameters of the oscillation of the cantilever (for example oscillation amplitude) in dynamic mode. The deflection is detected by shining a laser beam on a mirror surface at the top of a silicon cantilever and reading the position of the reflected beam with a quadrant photodiode. With proper calibration, changes in the position of the reflected beam can be directly related to the cantilever displacement [137]. Most common operation modes of conventional AFM are contact, non-contact and tapping modes.

The easiest to realize is contact mode, where the tip is kept in contact with the sample during scanning. The feedback loop maintains a constant deflection of the cantilever, thus, it follows the topography of the surface [138]. Contact mode offers high speed of data acquisition and theoretically provides the highest resolution out of all of the conventional AFM operation modes, as the forces experienced while the tip is in contact with the sample are the strongest and they change rapidly with the distance (Fig. 3.2). Practically, the influence of shear forces acting on the tip often lowers the resolution of this mode. Moreover, contact mode is not suitable for the investigation of fragile systems, as their atomic structure might be damaged by direct interaction with the tip [66].

In non-contact mode, the tip is placed at a certain distance from the investigated surface, in the attractive regime (usually over 1 nm from the surface) (Fig. 3.2) and the cantilever is oscillating at its own resonance frequency. Changes in the topography, i.e. changes in the distance from the tip to the surface, alter the resonant frequency or the vibration amplitude of the oscillating

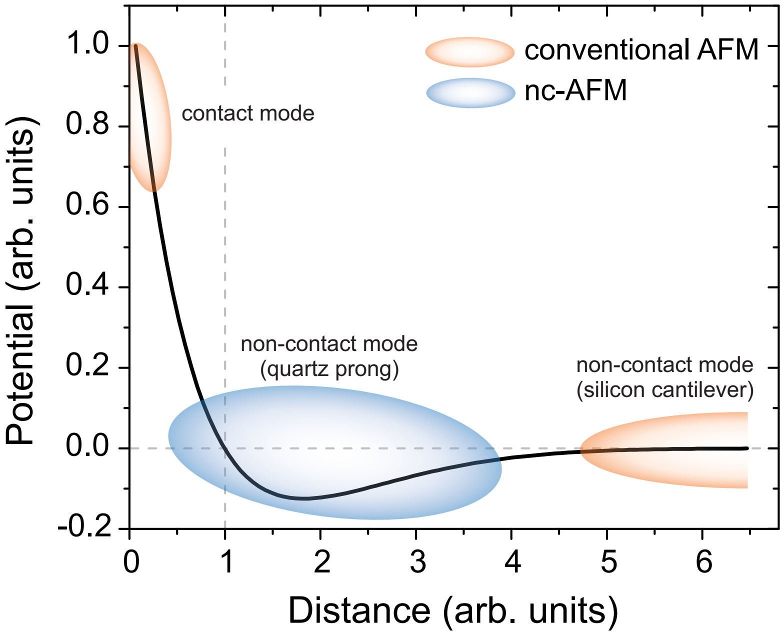

Figure 3.2 Lennard-Jones potential with marked regimes of operation of the AFM and nc-AFM modes. The static non-contact mode is sensitive to Van der Waals forces, while the dynamic non-contact mode can also be used to probe the Pauli repulsion.

cantilever. Keeping these parameters constant requires counteracting changes in topography, what is realized with the Z feedback loop that keeps the average force constant and yields the topography of the scanned surface. This mode avoids the issue of the shear forces, as well as it does not risk damaging the sample, however, it is slower than contact mode [66]. Moreover, the attractive forces are significantly weaker than the repulsive and maintaining the constant attractive force may be challenging (Fig. 3.2). This limits the resolution of non-contact mode. It can be improved by positioning the tip closer to the sample and oscillating the cantilever with smaller amplitudes, although this requires cantilevers stiffer than the standard ones made out of silicon [139].

In tapping mode, the cantilever vibrates with amplitude higher than the distance to the sample and the tip maintains contact with the surface for a short time at each oscillation cycle. The amplitude of the oscillation changes with the surface topography and the image is acquired by minimizing these changes with the Z feedback loop adjusting the average position of the cantilever [140]. Tapping mode shares the advantages of both contact and non-contact modes, providing resolution close to the contact mode, avoiding the issues of shear forces and minimizing potential destructive effects of moving the tip in persistent contact with the sample [66].

Conventional AFM is not suitable to investigate fragile surface adsorbates, such as organic molecules, as it often damages nanostructure of investigated systems [141]. Despite this limitation, even the static modes are capable of imaging atomic structures of certain surfaces under specific conditions [139], [142]. In comparison to STM, AFM does not require *in-situ* treatment of the tip apex (as its electronic state is relatively irrelevant for the experiment) nor careful sample preparation. Thanks to the relative simplicity of operation and the possibility of providing information at both the micro- and nanoscale, it has widespread use in both research and industry. It has been utilized in biology, biochemistry and biomedicine [137], [143]–[147] polymer chemistry [148], [149], microelectronics and industrial grade material science [150].

The second type of AFM, nc-AFM is dedicated only to the non-contact mode of operation. Its basic design, also called qPlus sensor, is presented in Fig. 3.1 b). It differs from the conventional AFM by the geometry, used materials and the detection system. The AFM cantilever is replaced by a prong that is perpendicular to the sample and oscillates in its plane. Moreover, the prong is made of quartz, which, compared to silicon, has a higher spring constant and stiffness, rendering oscillation with smaller amplitudes possible to control and utilize [151]. As already mentioned, oscillation with smaller amplitudes at shorter tip-sample distances (Fig. 3.2) improves the resolution of non-contact mode. The construction of basic nc-AFM was based on the quartz tuning fork used in Swatch wristwatches [139], due to their high-quality factors (Q-factors), thus, low energy losses during the oscillation. Due to the properties of the quartz prong, the resolution of nc-AFM is significantly higher than the resolution of the non-contact mode of the silicon-based conventional AFM [139]. As quartz exhibits the piezoelectric effect, the read-out system could be changed, from laser-based to purely electrical, where the piezoelectrically generated charges are sensed with metal electrodes evaporated on both sides of the prong. The working principle of nc-AFM is based on the fact that the infliction of external forces on the oscillating prong leads to changes of the spring constant and the resonant frequency. When unperturbed by external forces, the quartz prong with spring constant k_0 vibrates at the resonance frequency f_0, maintained by an external oscillation. When the tip is placed in proximity to the sample, a force is inflicted, leading to a change of the spring constant of the prong, and to a new, shifted resonance frequency. The oscillation of the prong generates a piezoelectric current signal between the electrodes of the prong, which is read out and converted to a voltage signal [151], [152]. The difference between the original and the new resonance frequency, Δf, carries information about the measured force. An oscillating quartz prong with such a tip can be represented as a mass m, attached to a spring (k_0). The resonance frequency of such a system is thus:

$$f_0 = \frac{1}{2\pi}\sqrt{\frac{k_0}{m}}. \tag{4}$$

Forces acting on the tip and the cantilever will alter the spring constant, resulting in a change of the resonance frequency to:

$$f_i = \frac{1}{2\pi}\sqrt{\frac{k_0 + <\Delta k>}{m}}, \tag{5}$$

where $<\Delta k>$ stands for time average of Δk over a single oscillation cycle [153]. Taking into account the approximations: $< \Delta k > \ll k_0$, $\Delta f = f_i - f_0$ and $\Delta k \approx \frac{2k_0}{f_0}\Delta f$, allows deriving a relation between the force and the frequency shift Δf [60], [153]:

$$\Delta f = \frac{f_0}{2k}\frac{2}{\pi A^2}\int_0^{2A} d\zeta \frac{A-\zeta}{\sqrt{2A\zeta - \zeta^2}} F(z_{min}+\zeta), \tag{6}$$

where A stands for the oscillation amplitude and z_{min} is the closest approach position of the tip to the sample (z-A, where z is the average position during oscillation). Term ζ takes into account the position of tip at time t for the resonance frequency f_0: $\zeta = A(1 + cos(2\pi f_0 t))$, which is a substitution of variables that allows integrating the tip position over one oscillation cycle. According to this relation, the existence of an attractive force between the tip and the sample would result in a lower spring constant and a negative frequency shift. A repulsive force would lead to the reversed effect, resulting in a higher spring constant and a positive frequency shift (Fig. 3.3).

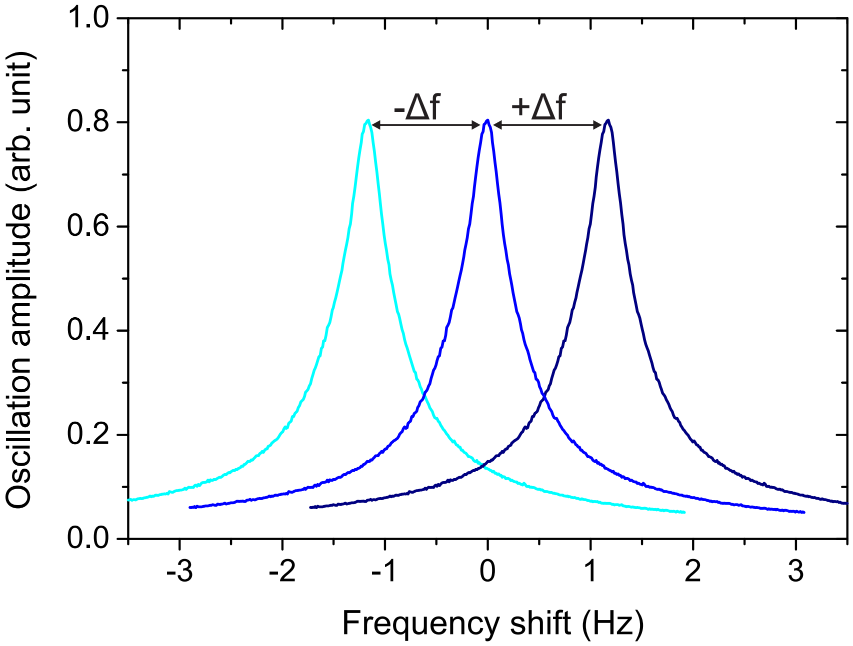

Figure 3.3 Resonance curves of a tuning fork in the unperturbed state (middle curve) and under the influence of an external force (light and dark blue). The force applied to the tip can lead to a positive (repulsive force) or the negative (attractive force) frequency shift. 0 on the frequency shift coordinate corresponds to the original, unperturbed resonance peak position.

The design of the nc-AFM depicted in Fig. 3.1 b) has been developed by Giessibl in 1996 [139]. Over time, the qPlus design has become a standard solution in nc-AFM. Compared to the silicon cantilevers, the properties of the quartz-based qPlus sensors do not vary dramatically with temperature, and in addition, cooling the quartz sensor increases its spring constant [154], [155]. As there is no laser-based detection system, the qPlus sensor can be efficiently cooled, which further improves the signal-to-noise ratio and the mechanical properties of the sensor. All of these aspects are especially important for precise, nanoscale experiments at low temperatures [154]. Furthermore, its default resonance frequency of 32.768 kHz, is high enough to avoid interaction with the vast majority of noise sources encountered in a typical laboratory environment. Moreover, the length of the electrodes can be reduced without significantly reducing the sensitivity of the sensor (e.g. reducing the length by 20 % reduces the sensitivity only by 4 % [151]). Reducing the length of the oscillation read-out electrode on the prong allows contacting the tip electrically in a circuit separated from the nc-AFM one. This introduces a possibility of using the nc-AFM tip as a tunneling tip, thus, permitting integration of nc-AFM and STM in one device.

Contrary to the first model of the qPlus sensor using *Swatch* watch tuning forks, the modern successor, here manufactured by *Omicron*, is specifically designed for STM/nc-AFM combined devices (Fig. 3.4). In this version, the immobilized prong is completely removed and replaced by a flat slab of quartz used for mounting the sensor at the head of the instrument. Three electrodes are integrated into the prong: two for the nc-AFM outgoing signal and one for the STM tip. The two nc-AFM electrodes can be accessed from both sides (Fig. 3.4 b) and c)), so that integration of the sensor into instruments with different STM/nc-AFM head geometries can be done. At the end of the prong, a gold pad is present with enough space to glue the tip to it.

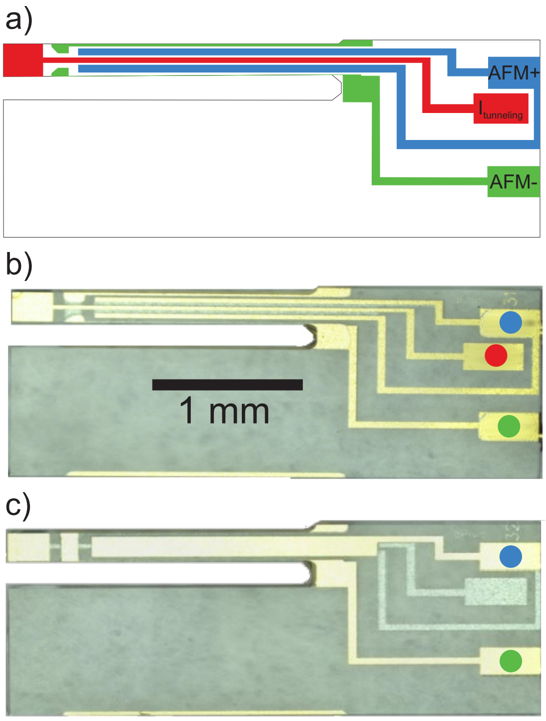

Figure 3.4 **a)** Scheme of the *Omicron* qPlus sensor with marked electrodes and its distribution along the sensor. The nc-AFM electrodes are presented in blue and green, the STM electrode in red. **b)** and **c)** Pictures of an *Omicron* qPlus sensor from the front and the back. The STM electrode is accessible only from the front side.

As the oscillation amplitude during standard operation is often in the sub-Å regime, the electric signal carrying the oscillation information is extremely small and needs to be amplified and processed [152]. During bending of the quartz prong, charges are piezoelectrically generated at the prong surfaces, read out by the electrodes and amplified by the current-voltage amplifiers in two separate electrical channels (Fig. 3.5). In this approach, the uncorrelated noise increases by a factor of $\sqrt{2}$, but since the signal is now also twice as large, effective signal-to-noise ratio increases by $\sqrt{2}$. Two separate deflecting signals are later differentially amplified in the instrumentation amplifier so that the correlated noises can be completely canceled out [152]. In order to achieve maximum amplification, the current-voltage amplifiers have to be placed as close as possible to the qPlus sensor. In all combined STM/nc-AFM devices, the tunneling current is processed in a circuit that is separated from nc-AFM.

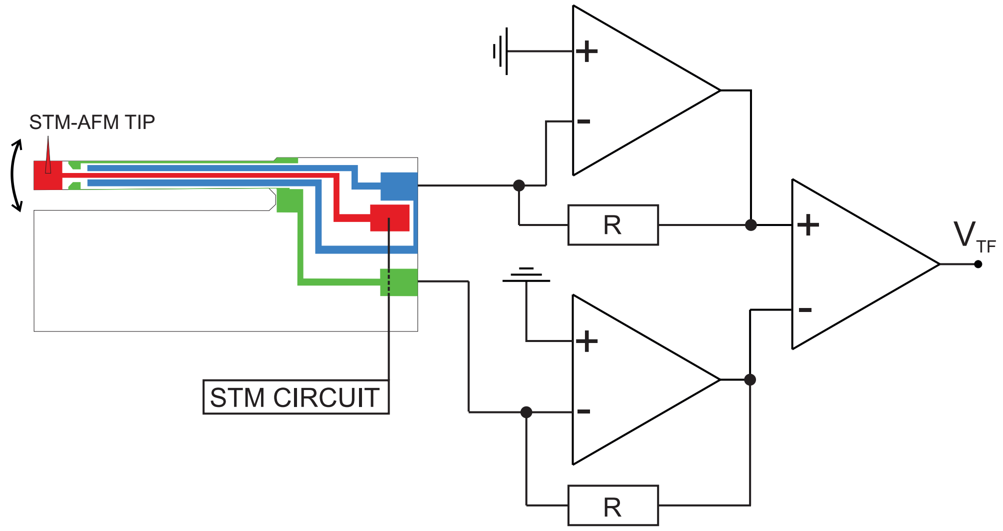

Figure 3.5 The nc-AFM signal amplification circuit. Signals from the electrodes are amplified by two current-voltage amplifiers ($10^8 V/A$), followed by an instrumentation (differential) amplifier (10^{2-4}) and a bandpass filter.

3.2 4 K STM/nc-AFM setup design

The design of the ultra-high vacuum (UHV) 4 K STM/nc-AFM used to carry out experiments presented in this thesis is based on the UHV 4 K STM previously constructed in the Nanoscale Science Department of the Max Planck Institute for Solid State Research (MPI FKF) by D.P. Rosenblatt [156], which itself was based on the STM head design by C. Ast [157]. This section will focus on the design changes necessary to implement the nc-AFM option.

The combined STM/nc-AFM device enables both STM and nc-AFM measurements at 4 K under UHV conditions. The set-up can be divided into three main parts, namely the preparation chamber, the load-lock chamber and the STM/nc-AFM measurement chamber (Fig. 3.6). The preparation chamber operates in the 10^{-10} mbar range. It is used for sample preparation, which includes sputtering/annealing and the evaporation of volatile organic molecules onto clean surfaces. The chamber also contains a manipulator, which serves as a transfer system that allows for the sample and the qPlus sensor transfers between the chambers.

The load-lock chamber functions as a connection between the UHV of the preparation chamber and the ambient conditions and it can be used to introduce new samples, as well as new qPlus sensors. The load-lock chamber also provides a docking station for vacuum and cryo-vacuum suitcases. The vacuum suitcases are transportable chambers, which can maintain UHV without external support for a limited time. They can be used to transfer samples without exposing them to non-UHV conditions. Usually, they are attached to an opened load-lock, which is then pumped to HV or UHV. Upon reaching a satisfactory vacuum, the valve separating the suitcase and preparation chamber can be opened, allowing for the sample transfer. The use of the vacuum and cryo-vacuum suitcases will be described in details in Chapters 5 and 6.

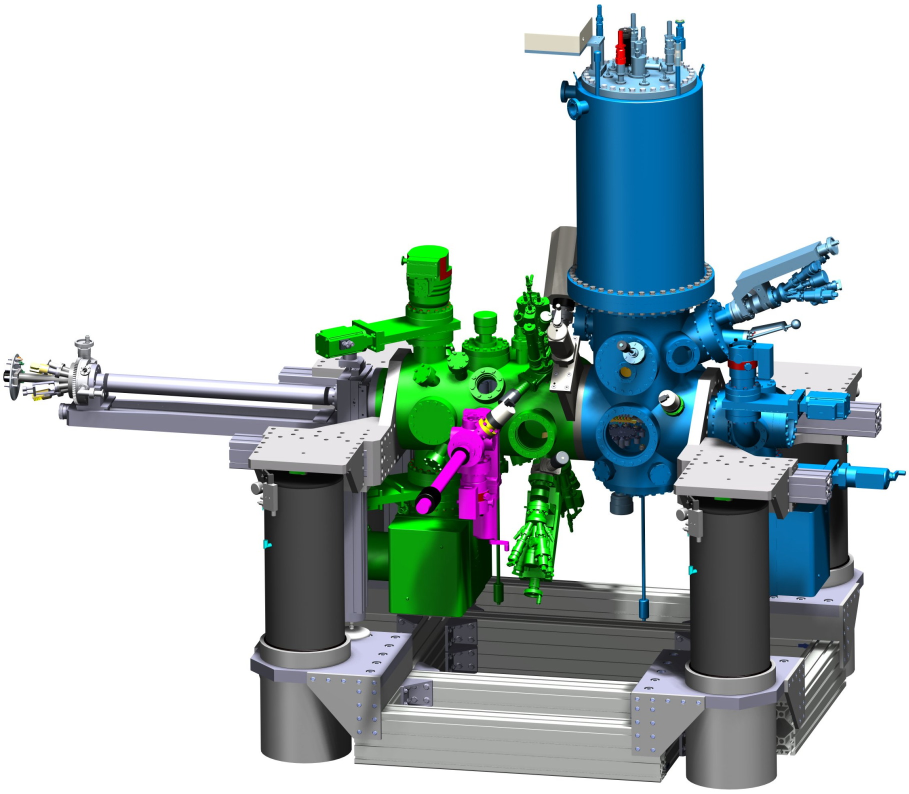

Figure 3.6 3D drawing of the 4 K STM/nc-AFM. Main parts of the machine are marked by colors: blue - measurement chamber; green - preparation chamber; pink - loadlock chamber.

In order to provide clean and stable conditions for the experiments, the STM/nc-AFM device in the measurement chamber is mounted to a liquid helium - liquid nitrogen bath cryostat. With holding times of 6 days for the 20 L helium vessel and 4 days for the 15 L nitrogen vessel, it allows for over 3 days of unperturbed measurements. The STM/nc-AFM head is attached to the bottom of the cryostat. Furthermore, to ensure thermal stability, the STM/nc-AFM head is surrounded by radiation shields. The vacuum in the measurement chamber is maintained by an ion pump, carbon trap and the cryostat itself, providing the operating pressure of 10^{-11} mbar. The chamber is also equipped with a parking carousel with storage positions for samples and qPlus sensors. The additional feature of the chamber is a dosing system, which allows dosing gases directly onto the cold surface at the center of the STM/nc-AFM head.

In order to be suitable for STM/nc-AFM operation, the head has been modified from the original design (Fig. 3.7 a)). Inside a piezo tube, four additional electrical connections are now present. In the previous design, only a slot for the main plug of the STM tip shuttle (similar to the one presented at Fig. 3.7 b)) was present, providing the tunneling contact. The additional electric connections are used to contact the nc-AFM sensor. These electrodes are attached to the qPlus sensor assembly via gold spring loaded contacts in the qPlus shuttle. The oscillation of the qPlus sensor is driven by applying an AC voltage signal matching the resonant frequency of the sensor to the Z component of the scanner tube and no additional oscillator is needed.

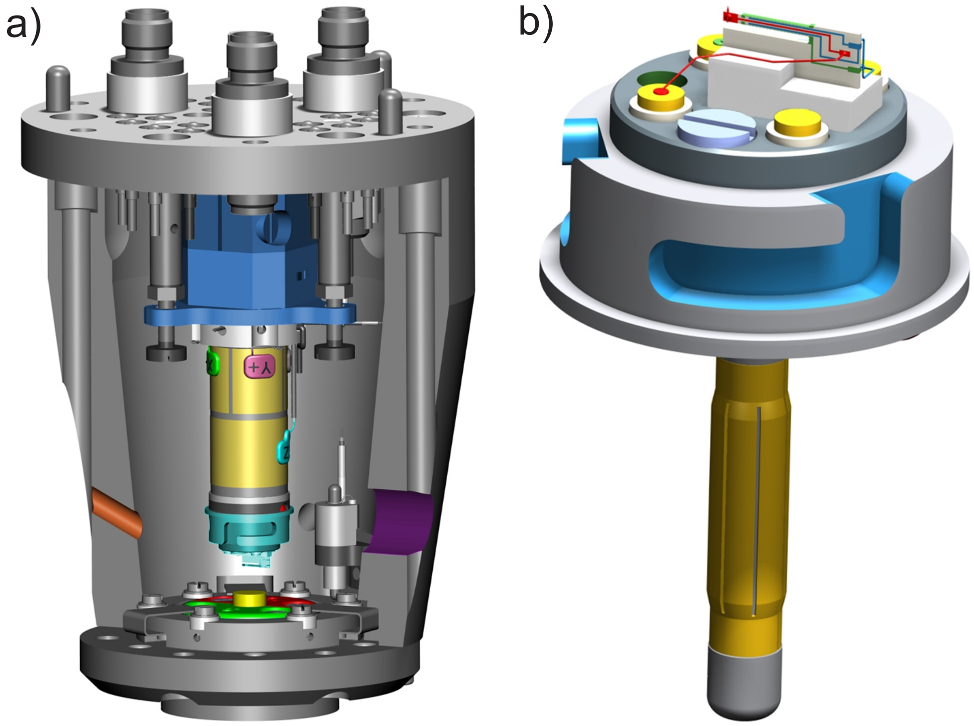

Figure 3.7 3D drawings of the 4 K STM/nc-AFM head and the qPlus sensor transfer shuttle. **a**) Inside view of the enclosed STM/nc-AFM head. Main parts of the head are marked by the colors: blue - piezoelectric slipstick approach system from *Attocube*; gold - scanner piezo; turquoise - qPlus sensor shuttle; green and red - sample holder half-plates holding the sample; purple - optical access used for controlled in-situ qPlus sensor exchange; orange - access for the in-situ dosing. **b)** The qPlus sensor shuttle. The shuttle consists of: the qPlus assembly seen on top; the main plug which is inserted into scanner piezo tube visible at a); the bayonet mechanism serving as a lock during transfers; four spring-loaded contacts (not visible in the image, except their upper counterpart at the qPlus sensor assembly itself) and a ruby sphere, which fulfills a role of a positioner during insertion of the shuttle into the piezo tube (visible in a) as a red feature above the turquoise qPlus shuttle).

According to the design presented in the previous section, the outgoing AFM electrodes are contacted to a preamplifier roughly 30 cm away from the sensor and attached to the liquid nitrogen cryostat shield. Optical access to the head is available, which is used for controlled in-situ exchange of qPlus sensors.

The qPlus sensor assembly (Fig. 3.8) is prepared in the following way:

1. A metal base plate is fabricated, with four holes for contacts and two countersunk holes for mounting screws, **a)**.
2. Four spring loaded gold contacts glued inside insulating ceramics are inserted and glued into the holes of the metal base plate, **b)**.
3. The sapphire support is glued on top of the base plate, **c)**.
4. The qPlus sensor is glued to the support in two stages, **d)**. First, two patches of glue are applied to temporarily hold the sensor in a proper, vertical position. Additional glue is applied along the bottom edge of the sensor to ensure long term structural stability.

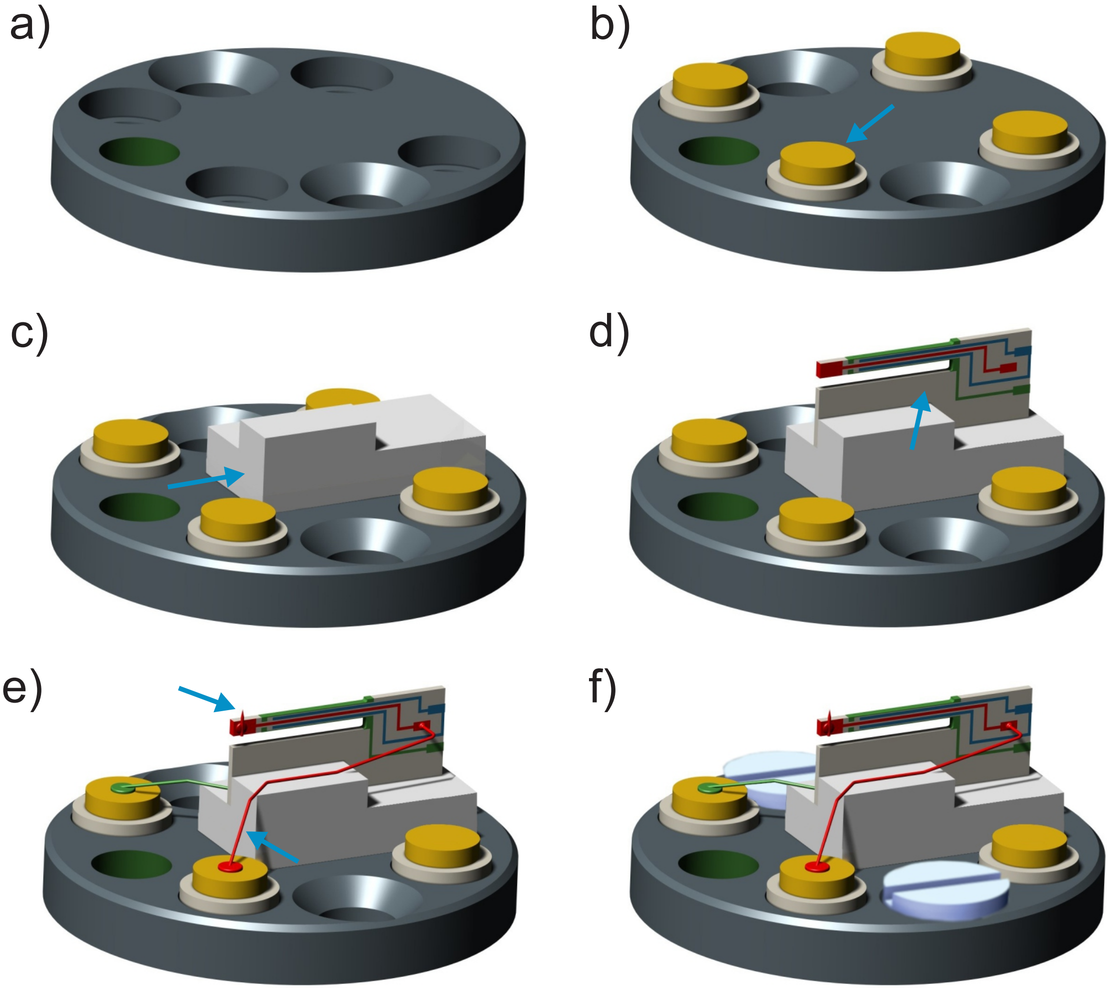

Figure 3.8 Step by step assembly process of the qPlus sensor shuttle. The elements added in subsequent steps marked with blue arrows.

5. A small patch of conductive epoxy *EPO-TEK E4110* is placed with a needle tip on the gold pad at the end of the qPlus prong, visible in **d)**.
6. With the help of a three-dimensional positioner controlled by micrometer screws, the assembly is moved into close vicinity of a prepared glass slide, where 99.95%, 25 μm platinum wire is cut into tips with length around 0.5 mm using clean laboratory scalpel blades.
7. One of the tips is pushed to the edge of the slide, close to the prong in such a way, that with one end it resides on the glass slide and with the second it hangs in the air.
8. The prong is moved upwards, contacting the hanging side of the tip, **e)**.
9. The assembly is left for 2 hours, to start the curing process of the conductive epoxy, making the epoxy semi-solid. After this time, it is transferred to the oven for high-temperature curing (100^{o}C, 1 hour).

10. $50 \mu m$ thick gold wires (**6**) are bonded between the pads on the qPlus sensor and the top side of the spring loaded contacts, **e)**.

11. The assembly is attached to the shuttle with two molybdenum screws, **f)**.

For all of the gluing process (except the tip attachment), *EPO-TEK H77* electrically insulating, heat conducting epoxy was used and after each step, the curing procedure of 1 hour at 150^{o}C was done.

3.3 4 K STM/nc-AFM noise and performance optimization

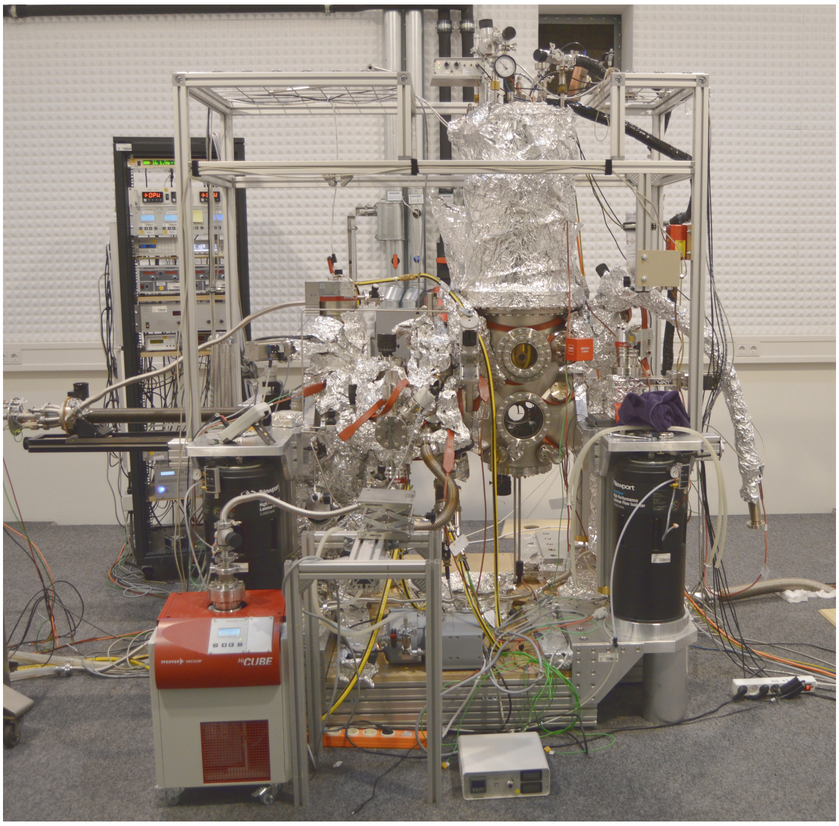

Figure 3.9 Photo of the 4 K STM/nc-AFM instrument in the Precision Lab of the Max Planck Institute for Solid State Research

The 4 K STM/nc-AFM was originally assembled in the main building of the Max Planck Institute for Solid State Research and the first tests were performed in place. They included the check of the basic functions of STM and nc-AFM such as basic imaging of metal surfaces with step recognition, without atomic resolution and surface reconstruction imaging [158]. Furthermore, tests of sample cleaning procedures and the cryostat cooling were performed. Upon proving that all the basic functions of the instrument are working, it was moved to the Precision Lab (Fig. 3.9). In its specialized, low noise environment, where the equipment is highly isolated (electrically, electromagnetically, mechanically and acoustically), a significant improvement of the machine's performance was immediately observed. The first spectrum (Fourier transform of tunneling current signal, Fig. 3.10), acquired with 100 mV 100 pA setpoint, revealed ±11 pm oscillation in *Z* axis in the tip-sample junction. Although switching the lab environment to the Precision Lab improved the signal-to-noise ratio of the STM mode, additional fine-tuning of the device was necessary to perform the high precision nc-AFM measurements. Measured spectra revealed a number of noise features with defined frequencies that degrade the STM and nc-AFM performance, mainly in the low-frequency regime, below 150 Hz. These issues were resolved as follows:

- **1.9 Hz** - the eigenfrequency of the concrete laboratory damping, appeared due to the deregulation of the sensors used for keeping the floor of the room in one, stable plane. Fixed by the recalibration of the aforementioned sensors.
- **7.8 Hz** - the eigenfrequency of CuBe springs holding the STM/nc-AFM head. The noise could be eliminated by putting the head into the stiff position, however, this enhanced the reception of every other noise, therefore they had to be eliminated before dealing with this issue.
- **14 Hz, 28 Hz, 30 Hz, 57 Hz** - the eigenfrequencies of cryostat and chambers. Due to the heavy mass, the machine can oscillate in the set of its own resonance frequencies

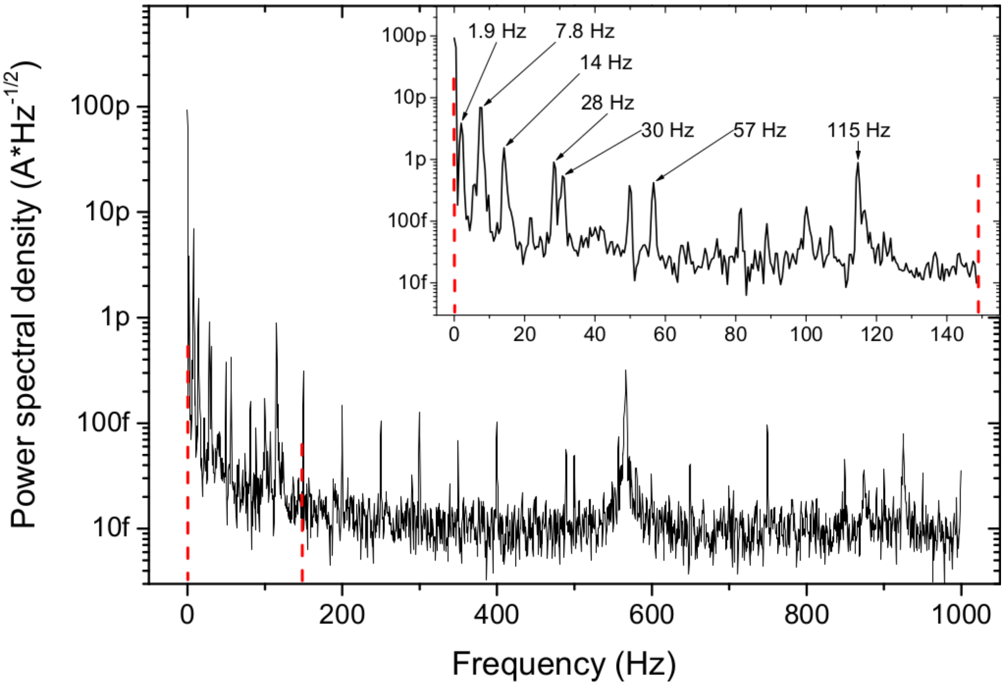

Figure 3.10 Noise spectrum of the tunneling current in the 0-1000 Hz range, recorded with a disabled STM *Z* axis feedback. The peak at the 0 Hz position is an artifact of the mathematical analysis of the signal, whose height depends on the total height of the peaks in the signal. The inset shows the low-frequency noise peaks between 0-150 Hz. Setpoint: 100 pA, 100 mV.

for a long time after being excited. The issue was solved by changing the mechanical properties of the system by:

  - removing the active dampers from under the machine (with working laboratory damping they were obsolete) and replacing them with solid metal cylinders for better contact with the concrete mass of laboratory dampers;
  - adding 400 kg of lead, resulting in even better coupling to the concrete block, as well as lowering the center of the mass of the machine;
  - adding a frame and crossbars, making the chamber stiffer and preventing self-oscillations.

- **115 Hz** - frequency of the pumping systems outside of the laboratory. Connecting of the damped and the undamped parts of the laboratory resulted in the transport of the mechanical vibration omitting the damping system. Thick water cooling tubes were found to be responsible for this effect, cross-connecting the aforementioned parts. The rearrangement of the tubes eliminated the problem.
- **550-600 Hz** - the mechanical noise of an unidentified source, not associated with the device or the lab itself and encountered on very few occasions.

After elimination of the noise sources, the STM/nc-AFM head was put into a stiff contact with the cryostat, which in turn revealed the broad range of mechanical noises that originate from boiling of the liquid nitrogen in the cryostat. This effect can be eliminated by pumping. Upon lowering of the pressure in the nitrogen cryostat, the boiling point of the nitrogen falls following the Clausius-Clapeyron equation [159]. Upon reaching pressures of around 100 mbar the nitrogen starts solidifying. The boiling is then replaced by sublimation, which is virtually noiseless. The nitrogen pumping system using a high power scroll pump was assembled and placed in a separate pumping room in order to prevent mechanical noise. It is able to pump liquid nitrogen below 100 mbar and solidify the whole reservoir. After the noise minimization, the mechanical stability of ±400 fm was achieved, fully utilizing the low noise environment of the Precision Lab and allowing even the most demanding nc-AFM measurements to be performed (Fig. 3.11). Next, the electric noise appearing at multiplications of 50 Hz was dealt with. The so-called ground loop noise originates from the unintentional loops in the circuitry of the machine. The grounding was rearranged into a star layout, with the central point at the *Femto* tunneling current amplifier. As a result, the amplitude of the ground loops noise was reduced by an order of magnitude (Fig. 3.12).

After achieving the desired stability and signal-to-noise ratio, performance tests of the STM mode were done. First, an atomically resolved image of Cu(111) was acquired with hydrogen-assisted STM (described in section 1.3) and is depicted in Fig. 3.13. It proves that the STM mode of our 4 K STM/nc-AFM device is capable of imaging atomic structures with high precision. Secondly, an atomically resolved image of a NaCl(100) monolayer (Fig. 3.14) was acquired using a CO terminated tip. Two Na vacancies in the NaCl lattice have been imaged,

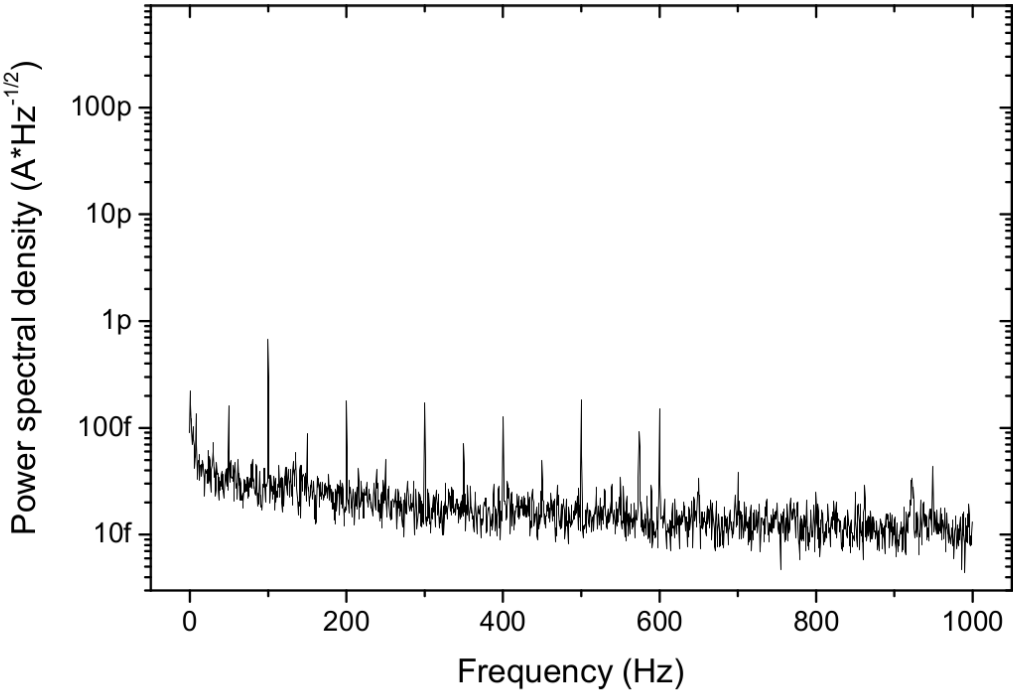

Figure 3.11 Improved noise spectrum of the tunneling current in the 0-1000 Hz range, recorded with the STM *Z* axis feedback disabled. All of the peaks associated with mechanical noise are eliminated or minimized to negligible values. Setpoint: 100 pA, 100 mV.

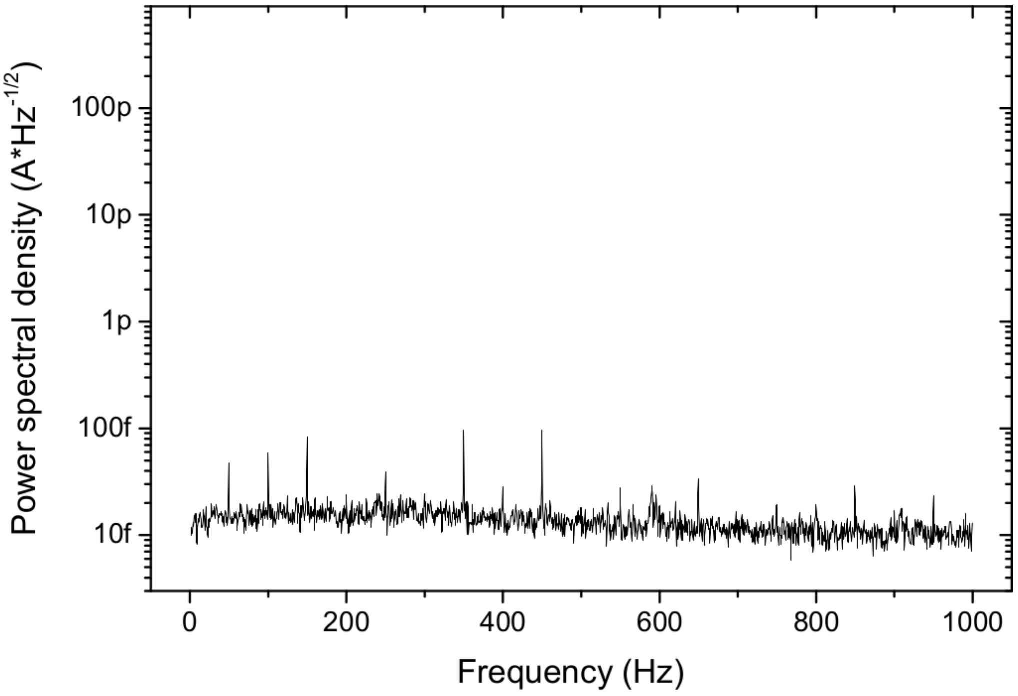

Figure 3.12 Final noise spectrum of the tunneling current in the 0-1000 Hz range, recorded with the STM *Z* axis feedback enabled. Peaks associated with ground loops are minimized by an order of magnitude. Setpoint: 100 pA, 100 mV.

showing a decrease in the corrugation of the surrounding Cl$^-$ ions [118], [121]. Data from both the Cu(111) and NaCl(100) images were used to calibrate the piezo scanner. Both experiments confirmed the readiness of the STM mode.

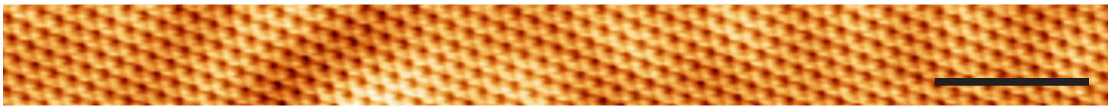

Figure 3.13 Constant current image of a Cu(111) surface revealing its atomic structure. The ripples on the image correspond to standing wave of surface electrons arising from scattering at surface defects (atomic steps, adatoms, adsorbates) [160], also called the Friedel oscillations. The image has not been filtered. Set point: 100 mV, 10 pA. Scale bar 2 nm.

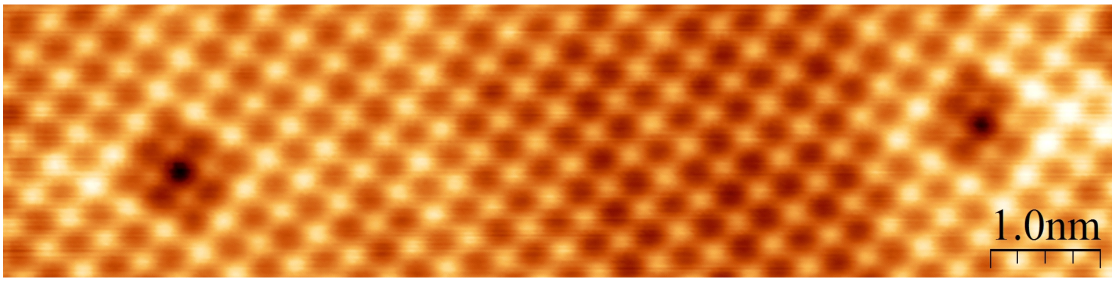

Figure 3.14 Constant current image of a NaCl(100) surface, revealing its atomic structure. Bright protrusions correspond to Cl$^-$ ions, low intensity features to Na$^+$ ions [118], [121]. Two features with the lowest intensity are associated with Na vacancies. The image has not been filtered. Setpoint: 1 V, 100 pA.

Along with the improvement in the STM performance, nc-AFM tests were carried out. The validation of the nc-AFM qPlus sensor consists of measurements of the resonance curves without any other object in close proximity. At the start, a resonance frequency of the qPlus sensor has to be found. For the unperturbed sensors, it is equal to 32.768 kHz and drops when the tip is attached to the prong [155]. For the sensors used in this work, the placement of the tips shifts the resonance position to values around 30 kHz. The resonance curves are attained by sweeping the driving oscillation frequency around the resonance of the qPlus sensor and recording the amplitude of the prong oscillation (Fig. 3.15). Simultaneously, the amplitude signal is analyzed to determine its phase difference with respect to the driving voltage. The main parameter that describes the performance of an oscillator is the Q-factor, which describes the energy loss in each cycle of a resonant oscillator and it is calculated by dividing the value of the resonance frequency by the full width at half maximum of the resonance curve. The higher the Q-factor, the more sensitive the measurements are. On the other hand, too high Q-factor results in slow sensor reaction to the force fluctuations. The dissipation of energy stored in the oscillation movement will be too slow, thus, the time to detect a change in the force will be longer, slowing down the overall measurement [161]. This is undesirable, so for standard operation of nc-AFM, the Q-factor should be kept in the 10000 - 100000 range, which guarantees experimentally feasible sensitivity and time of the measurement.

The first resonance curves were obtained in the main building of the Institute. Due to the presence of mechanical and electromagnetic noise (the ends of the electrodes of the qPlus sensors are open and act as antennas), the performance of the sensor was unsatisfactory (Fig. 3.15). After moving the device to the low noise environment of the Precision Laboratory, an immediate increase of the *Q*-factor from 5000 to 18500 was observed. Upon further cooling to 4 K, the *Q*-factor further increased to ~40000, due to the higher stiffness of quartz at low temperatures [162].

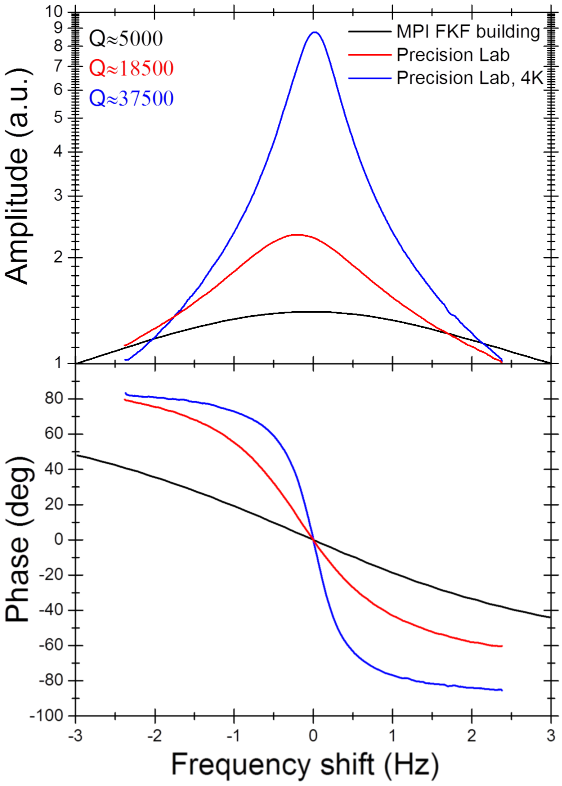

Figure 3.15 Comparison of resonance curves of the qPlus sensor in different environments.

Next, a scanning test of the nc-AFM was performed. Simultaneous operation of an STM and nc-AFM is possible due to their separated frequency regimes. Standard STM works in the range of 0-1 kHz, while the qPlus sensor prong oscillates at around 30 kHz. The only influence of the prong oscillation in the STM mode should be visible as an offset in the tunneling current. This is because, in one current integration cycle, a few oscillation cycles of an nc-AFM happen, which are averaged over time. The prong oscillates around one position (the STM set point), with the same amplitude in both directions. Due to the exponential behavior of the tunneling current, bending of the prong into the direction of the sample increases the current more than bending in the opposite direction decreases it, leading to an average offset in the tunneling current. The first test of the simultaneous operation of STM and nc-AFM has shown that the influence of the oscillation was different than expected. Two noise spectra are depicted in Fig 3.16, one with the prong oscillation disabled and one with the 30 pm oscillation. The 30 pm oscillation increased the signal baseline and induced additional noise peaks in the 1-400 Hz range. The nature of these peaks was purely mechanical and they were present in the data acquisition range of both nc-AFM and STM modes (nc-AFM is operating at ~30 kHz, but it has the same time regime of scanning or recording spectra as STM). It rendered both operation modes unable to distinguish a feature smaller than the average metal surface step size, ~200 pm. Shifting the driving oscillation frequency off the resonance position was disabling the effect, which indicated that it is not associated strictly with the rapid movement of the scanner piezo, but with the oscillation of the qPlus prong.

The oscillation of the scanner that is negligible with respect to STM is inducing the oscillation of the quartz prong with an amplitude three orders of magnitude higher. It was found, that this, in turn, was strong enough to induce resonant shaking of other elements of the assembly despite different resonance frequencies. The source of the noise was identified as the vibration

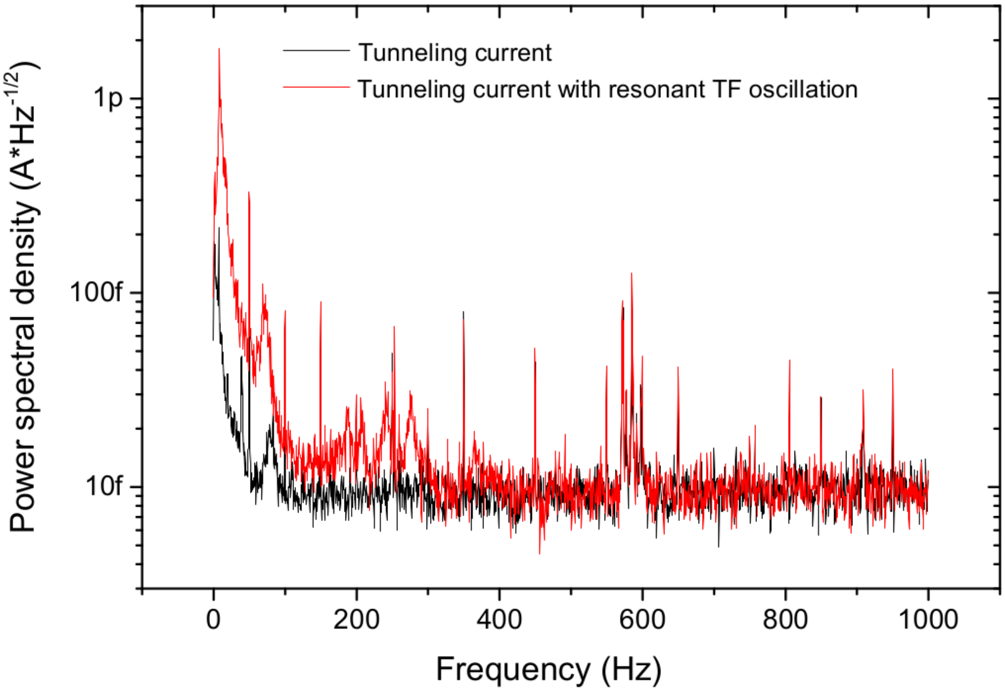

Figure 3.16 Two noise spectra in 0-1 kHz range representing the influence of the running nc-AFM on the current noise, recorded with the STM feedback switched off. With the 30 pm oscillation, increased baseline and additional noise peaks are present in the 1-400 Hz range. Setpoint: 100 pA, 100 mV.

of gold wires connecting the gold pads on the qPlus quartz slab to the spring loaded contacts at the qPlus transfer shuttle. As a solution, the wires were embedded in *H77* epoxy, whose highly stiff, amorphous structure acquired through curing, should prevent the vibrations.

Embedding the wires in the epoxy is realized on completed qPlus assembly. It is carried out in steps, as the epoxy changes its volume during the curing and if the wires are completely covered with semi-liquid epoxy before curing, fragile contacts between wires and electrodes can break. The process starts with an application of a layer below the wires and curing it at 150 ^{o}C. The wires are usually completely submerged with five applications of the epoxy. The result of the process is presented in Fig. 3.17.

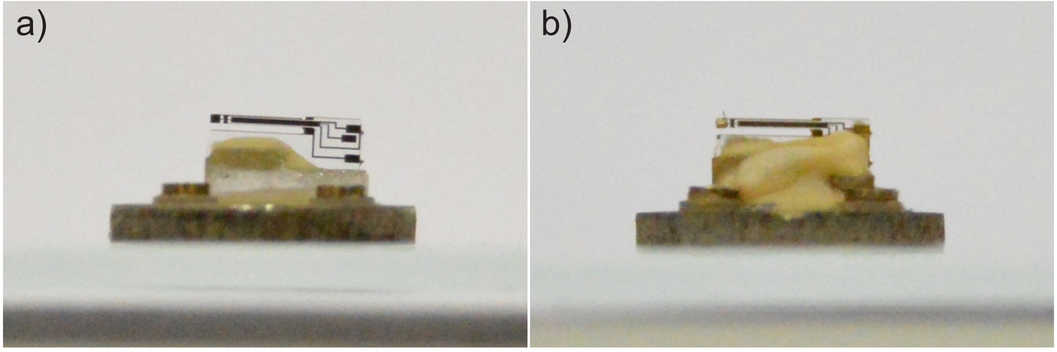

Figure 3.17 **a)** The qPlus assembly before attaching tip and bonding the wires. **b)** The qPlus assembly after attaching the tip, bonding the wires and embedding them in *H77* insulating epoxy. A tip can be seen on the left side.

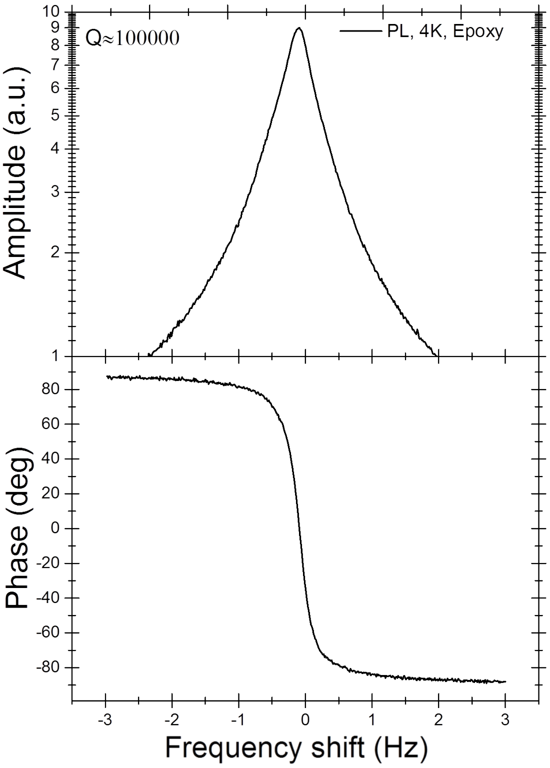

Figure 3.18 The embedding of the qPlus assembly resulted in an increase of the *Q*-factor to 100000. The dependence of the phase of the signal on the frequency shift is much steeper around 0^o, which corresponds to higher sensitivity of the sensor.

Embedding the qPlus assembly in epoxy resulted in doubling of the *Q*-factor (Fig. 3.18). The steepness of the phase signal around 0^o increased, confirming the higher sensitivity of the embedded sensor. During the measurement, the frequency shift, carrying the force information, is obtained by tracking 0^o phase with the frequency shift feedback. The higher the influence of the force on the phase of the incoming signal (the steeper the relation around 0^o), the smaller the force changes that can be detected by following the frequency shift. Embedding of the wires of the qPlus assembly solved the problem of the nc-AFM induced noise. Simultaneous STM/nc-AFM imaging has been performed as proof (Fig. 3.19). The atomic structure of NaCl was imaged, revealing the positions of Cl^- ions in both the nc-AFM frequency shift (Fig. 3.19 a)) and STM constant height imaging (Fig. 3.19 b)). During the image acquisition, the bias of STM has varied between 0 and 10 mV. The changes had no influence on the frequency shift channel, proving that the STM and the nc-AFM modes are successfully decoupled and advanced nc-AFM techniques, like the Pauli repulsion imaging, can be performed.

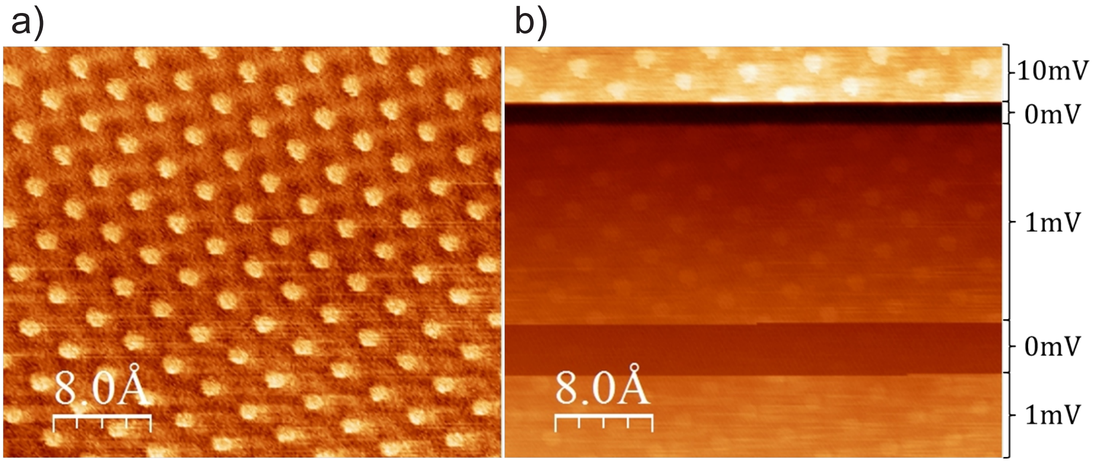

Figure 3.19 **a)** Simultaneous constant height imaging with STM and nc-AFM. Setpoint: 100 pA, 10 mV. **a)** The nc-AFM frequency shift image of the NaCl surface, revealing the positions of the Cl^- ions. **b)** The STM current image with varying bias. Changing the bias voltage, including 0 V (negligible tunneling current), has no influence on the nc-AFM measurement.

3.4 Pauli repulsion imaging

In addition to its original use (the imaging of insulating materials with atomic precision), the nc-AFM technique excelled in the imaging of organic molecules with submolecular resolution independently of their electronic states [48]. In the regular working regime (up to 1 nm separation between the tip and the sample), nc-AFM detects attractive potential that originates from Van der Waals forces. Moving the tip closer to the sample changes the interaction character to a repulsive one, as described by the Lennard-Jones potential (Fig. 3.20). The reason for this repulsive potential at close distances between two objects is the fermionic exchange interaction, also called Pauli repulsion as it originates from the Pauli exclusion principle. The interaction between two objects will be stronger if the associated electron density is higher, which can be exploited in nc-AFM [163]. Furthermore, repulsive interaction depends strongly on the distance, therefore small changes in distance or density of the electrons lead to remarkable changes in the force, which can be detected with nc-AFM. Considering this interaction for organic molecules, it should be the strongest for regions with a highly localized potential, like atoms and ridges between nearest atoms. Following this logic, placing the nc-AFM probe close enough to the investigated organic molecule should allow differentiation between the molecular backbone and the molecular orbitals. In this thesis, the technique utilizing this approach will be referenced to as the Pauli repulsion imaging.

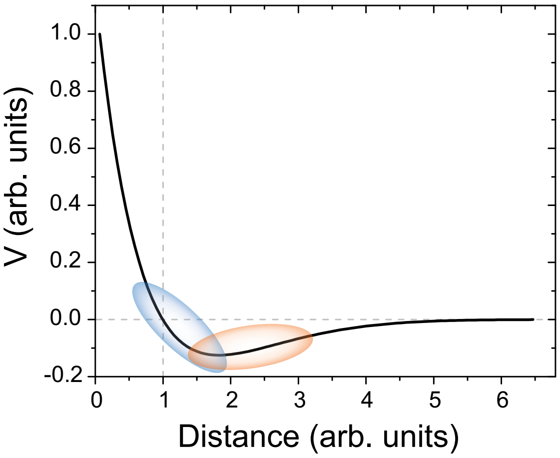

Figure 3.20 Lennard-Jones potential approximating the interaction between with distance between two neutral atoms or molecules. For metal surfaces the minimum of interaction is usually placed at 2-3 Å distance from the surface [164].

In order to achieve images of molecular structures with high contrast and easily distinguishable features, a few conditions have to be fulfilled. The imaging needs to be carried out at a specific distance from the adsorbate. It has to be at a range, where the Pauli repulsion starts to be detectable and the interaction potential becomes repulsive (blue area in Fig. 3.20). Positioning the tip even closer than that results in a stronger interaction and potential destabilization of the tip apex itself, which leads to a lowered resolution or unintentional changes of the junction geometry, either on the tip or the adsorbate side. At a proper operating distance, the interaction with the surface lying below the organic adsorbate may still have an attractive character (orange area in Fig. 3.20), leading to a significant contrast between the features of the molecular backbone and the rest of the image. This means that for the high contrast Pauli repulsion imaging, the interactions with the adsorbate and the underlying surface should take place on the opposite side of the minimum of Lennard-Jones potential. Such a placement of the tip would result in an image, where the structure is clearly distinct from the rest of the surface with features of the molecular backbone easily distinguished [48]. This strategy provides the starting distance conditions for the Pauli repulsion imaging.

The second requirement of the Pauli repulsion imaging is the on-surface stability of the investigated organic molecule. Following Newton's third law, the same force detected by the sensor will be inflicted on the investigated adsorbate [165]. If the molecule upon infliction of this force becomes mobile on the surface, it may be removed completely or at least change its geometry in the tip-sample junction. Furthermore, an alteration of the tip itself is possible. If only a certain part of the molecule is mobile, while the rest remains stable it will result in an inability to resolve the mobile part with the Pauli repulsion imaging. It is recommended that one avoids those parts while imaging the rest of the structure, as they also may induce changes to the tip apex, for example, remove the actual tip termination.

The third condition for the high contrast Pauli repulsion imaging arises from the proximity of the tip and the adsorbate. As the tip stays in the 1-2 Å distance to the molecule during this type of imaging, it renders the junctions consisting of pure metal tips unstable [166]. It results in either pick up of the molecule or uncontrolled crashes into the molecule/underlying surface, which heavily modify the tip apex. Therefore, a tip passivation with atoms or molecules is necessary for achieving tip-adsorbate separations in the Pauli repulsion regime [166], [167]. A wide array of tip terminations has been proposed, including Xe atoms [48], [168]–[170], Cl atoms [48], [168], [170], Br atoms [48], [168], [170], I atoms [168], O_2 [171], CuO [171], pentacene [48], CH_4 [172] and others, yielding results of different quality. Among them, the most established for the Pauli repulsion imaging is the CO termination [48], [163], [167], [169], [173]–[186].

The CO termination exhibits some favorable properties that allowed it to become a standard solution in the Pauli repulsion imaging. First of all, the tip apex functionalized with CO is more inert than a metal one and the Pauli repulsion regime is reachable without altering the junction [187]. Secondly, it always adsorbs on the apex with the C atom attached to the tip metal atoms and the O atom pointing down. In this geometry, the O atom is flexible. It relaxes laterally in close proximity to localized potentials, which results in tilting of the CO molecule and more abrupt changes of associated frequency shifts [169], [183]. In close vicinity of those features, even small differences in the position of the tip can cause significant changes in the magnitude and the direction of the relaxations of the CO molecule (Fig. 3.21) [183], [188]. It results in more pronounced frequency shifts and better resolution of the Pauli repulsion imaging, as compared with rigid tips and tip terminations.

Another reason for preferring CO terminated tips is the relative ease of functionalization. For less reactive surfaces like Au(111) or Ag(111), the CO molecule can be picked up directly from the metal surface. For more reactive ones like Cu(111), it is still possible, but each pickup attempt has a small chance of success. In order to make the CO functionalization available on demand for different types of surfaces, NaCl can be deposited onto the surface, forming clean, single or multilayer islands [64], [113]. The CO molecules are deposited on the sample

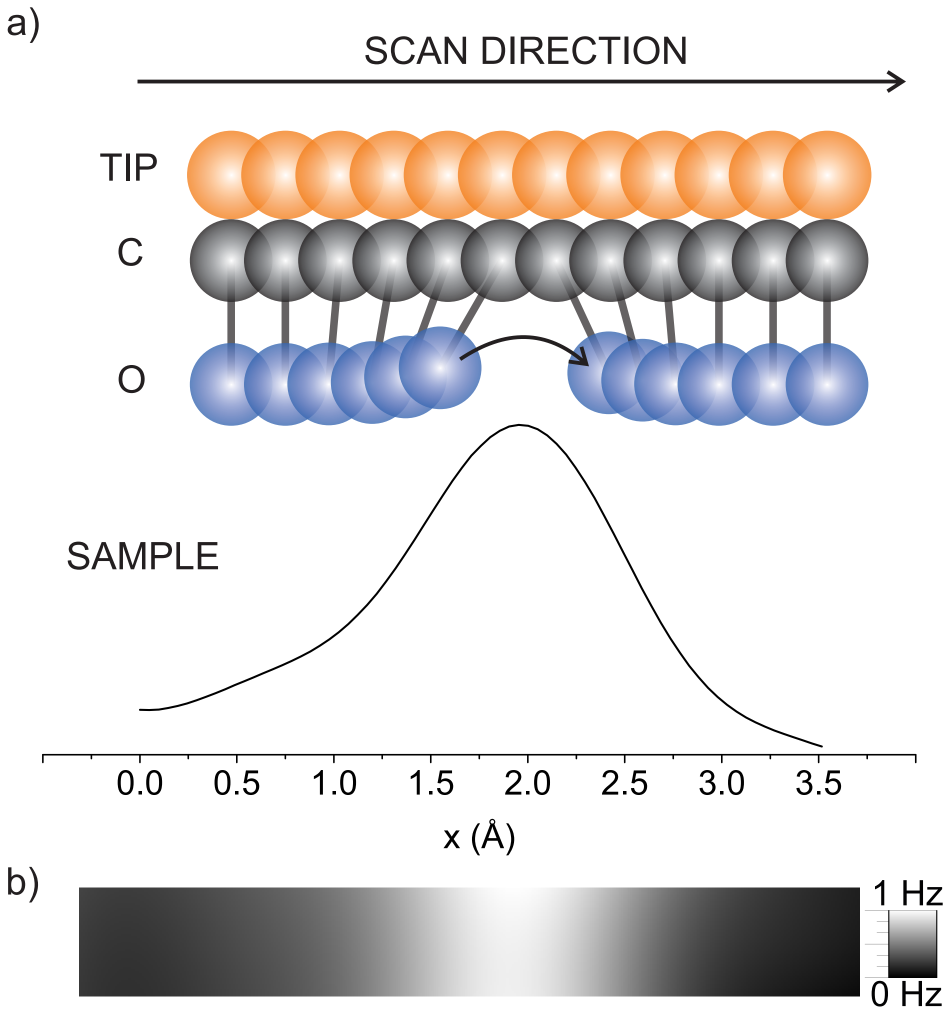

Figure 3.21 **a)** The behavior of the CO molecule at the tip apex during the Pauli repulsion imaging of a single C-C bond feature. The oxygen atom of the CO molecule is partly mobile and the C-O bond is flexible, resulting in its tilting in the close proximity of a localized potential. **b)** Slice of a frequency shift image of a feature between two carbon atoms connected with a covalent bond, corresponding to the line profile from a).

at cryogenic temperatures ensuring that they stay on the NaCl islands (at higher temperatures they would be mobile on this low reactive layer and desorb). Pickup from these islands is straightforward as the CO molecules have low binding energy to NaCl and the functionalization process only requires approaching the tip to the molecule. Then, the CO molecule desorbs due to the local potential of the tip, rotates, and attaches to the apex [189]. This technique can be used in combination with the majority of surfaces, including all of the most common metals in the scanning probe microscopy field (gold, silver, copper).

An example of the CO termination procedure is presented in Fig. 3.22. Before the pickup, the tip has to be treated in order to acquire a sharp apex with a pure metal composition. Such a tip results in the appearance of CO on the NaCl layer as a negative intensity feature, with an apparent depth below -100 pm (for arbitrary 1 V bias). Due to this contrast, CO on the NaCl can be used as a benchmark to validate the quality of the tip before the pickup

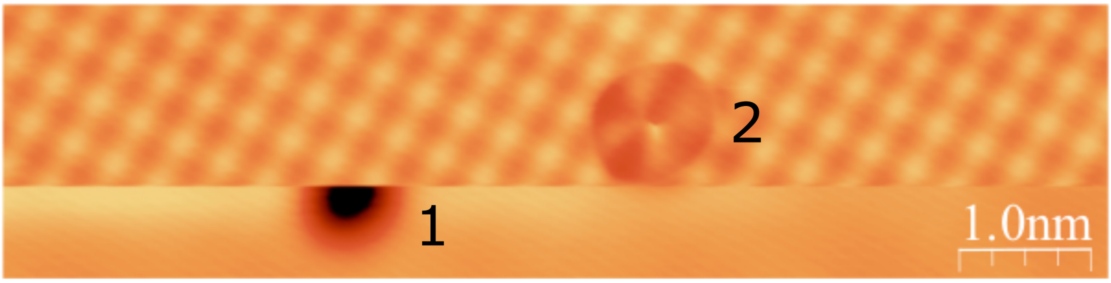

Figure 3.22 STM constant current image (20 pA, 1 V) before and after the CO pickup from the NaCl monolayer. The scanning is stopped upon reaching the CO molecule (**1**) with a sharp metal tip (bottom part of the image). Afterward, the CO molecule is picked and the scan is continued with the same parameters, revealing improved resolution of the NaCl layer and a different appearance of the next CO molecule (**2**), which now is a bright protrusion that distorts the appearance of the NaCl atomic lattice below it.

procedure. Clean metal tips usually do not resolve the atomic structure of the NaCl layer for relatively large distances (i.e. 20 pA, 1 V setpoint). In order to carry out the pickup procedure, the tip is stabilized above the targeted CO molecule. The bias is gradually lowered to 50 mV (with enabled STM feedback), what is followed by a gradual increase of the tunneling current set point, until the moment when an abrupt change of the Z position is observed, indicating the pickup. If the CO molecule is attached symmetrically to the last atom of the apex, the resolution of the NaCl layers is dramatically increased, revealing its atomic structure. Moreover, the topographic appearance of another CO molecule present on the NaCl layers changes, becoming a bright, "lens-like" protrusion, that elongates the appearance of the underlying Cl atoms [166].

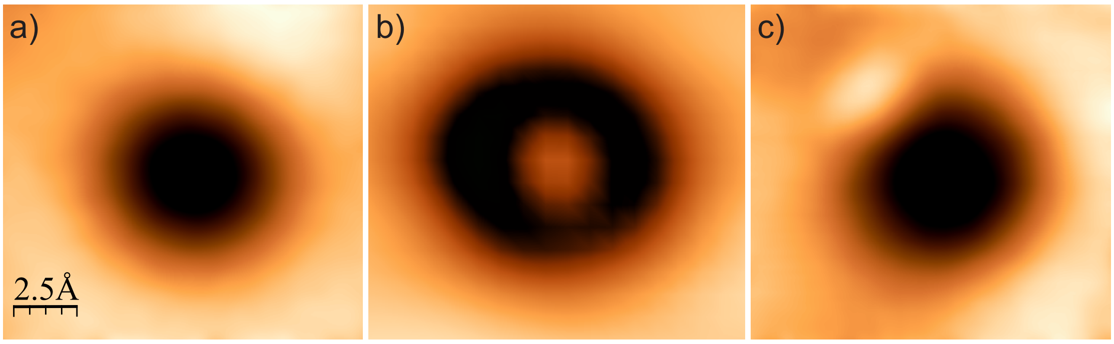

Figure 3.23 Comparison of the CO topographic appearance on Cu(111) before and after CO tip functionalization. Images were recorded in constant current mode, setpoint: 100 pA, 100 mV). **a)** Appearance of the CO molecule with the metal tip. **b)** Appearance of the CO molecule with a CO terminated tip. **c)** Appearance of the CO molecule with a non-symmetric CO tip termination.

Another validation of the CO functionalization quality can be done by imaging the CO molecule adsorbed on Cu(111) (Fig. 3.23). Before the CO pickup, when the tip apex composition is metallic, CO appears as low intensity, uniform, symmetric feature. After the pickup, CO takes on a "sombrero-like" appearance, where a bright protrusion is surrounded by a low-intensity halo. Any asymmetries of the CO adsorption on the tip apex would be visible as asymmetric distortions in the "sombrero-like" appearance, for example, a bright protrusion at the border of the low-intensity halo (Fig. 3.23 c)).

With a properly CO-functionalized tip, a high-resolution image of the molecular backbone can be obtained in the following way. First of all, the tip has to be stable in both *Z* axis, as well as in the lateral *XY* plane. The drift in *Z* might result in tip crashing (if in the direction of the sample) or losing the sensitivity during the image acquisition (if out of the sample). Drift in the lateral plane would result in the distortion of the image, either squeezing or elongating the features in the direction of the drift. With both the phase and amplitude feedbacks of nc-AFM enabled, the tip is positioned above the highest topographic point of the investigated molecule (leftmost benzene ring in the case in Fig. 3.24) with a bias voltage of 10 mV and chosen current value. Three different tunneling current set points were used in the example: **a)** 100 pA, **b)** 150 pA, **c)** 230 pA. After the stabilization, the STM *Z*-feedback is switched off and the bias voltage is reduced to 1 mV, in order to minimize the electrostatic and tunneling effects during image acquisition. The images are recorded with the scanning speed kept below 0.5 nm/s. The top image was recorded with the tip too far from the molecule, resulting in low intensity and resolution of the features of the molecular backbone. The bottom image, on the other hand, was recorded with the tip placed too close to the molecule and the interaction was too strong, resulting in a distorted appearance of the backbone. The middle image was recorded with the distance between the tip apex and the molecule fulfilling the conditions described at the beginning of this section, resulting in a non-distorted, sharp image, proving the capabilities of the 4 K STM/nc-AFM. This image and the investigated structure will be analyzed in detail in Chapter 4.

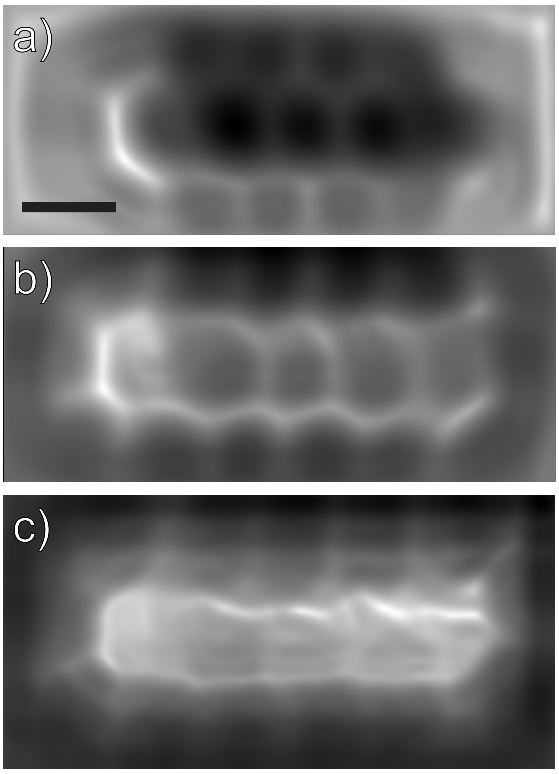

Figure 3.24 Set of Pauli repulsion images of the reacted tetracenothiophene molecule on a Cu(111) surface. Starting set points: **a)** 100 pA, 10 mv; **b)** 150 pA, 10 mV; **c)** 230 pA, 10 mV. Scale bar 2 Å.

The ability to perform the Pauli repulsion imaging is the final goal of the development of the combined STM/nc-AFM instrument and the realization of this technique marks its readiness. The Pauli repulsion imaging was used to identify the chemical structures in the projects presented in the following chapters of this thesis.

4 On-surface reactions of thiophene functional groups[1]

STM can be used to induce and study chemical reactions with nanoscale precision. Other techniques that allow for the elucidation of the chemical processes, such as IR spectroscopy, MS and NMR, share a limitation, as they measure huge numbers of the same processes in an ensemble. With STM, a different approach is possible, where the chemical processes can be accessed on a level of a single molecule. Furthermore, the chemical reactions can not only be induced on a single object but also in steps, which allow direct following the reaction pathways. Thus, this approach can be used to control and study sequences of the bond breaking and formation in single organic molecules with utmost precision. One of the prime examples of such a possibility is an STM-induced on-surface Ullman reaction [54], first presented in Chapter 2. A vast number of chemical reactions have been studied at the nanoscale with the help of STM [53], [54]. Among the fields which can potentially profit from the information obtained through the STM-induced processes are on-surface catalysis [163], [190], [191] and molecular electronics [192], [193]. In this chapter, an on-surface desulfurization reaction of a single sulfur-containing functional group embedded in a pentacene analog will be explored.

Pentacene, a molecule consisting of five benzene rings, is one of the most commonly investigated systems with STM [63], [194]–[200]. It has a simple and well-defined structure with flat adsorption geometry, where a π-conjugated system adsorbs parallel to the surface [63], [201], [202]. Moreover, it has good mechanical and chemical stability. It can be thermally evaporated and usually does not cluster upon the adsorption. Because of these properties, pentacene has often been used as a test system for the STM and nc-AFM imaging techniques with functionalized tips, including the organic molecule tip termination imaging [63], the p-wave tip imaging [119] and the Pauli repulsion imaging [48].

Replacing one benzene ring of a pentacene molecule with a sulfur-containing group (which is a more reactive moiety), creates a system that retains the stability and simplicity of the original pentacene structure, but introduces new possibilities in terms of chemical and physical properties. Here, we focus on a tetracenothiophene (TCT) molecule, where one of the benzene

---

[1] This chapter is based on publications 3 and 4 from the publication list.

rings of a pentacene molecule has been replaced with a sulfur-containing thiophene group. Chemistry of sulfur-containing groups, especially desulfurization reactions, bears significant importance in the sulfur cycles of biology [203]–[205], as well as in the fuel industry [206], [207], as sulfur has to be removed from natural fuels before they can be used. Especially, the heterogeneous catalysis for the desulfurization of diesel oil is of extreme importance and still poses a challenge to chemistry [208], [209]. Studying the desulfurization of a thiophene group directly on the surface of metals might prompt a better understanding of the catalytic effects of the metal surfaces and potentially lead to more efficient fuel processing methods.

In this chapter, we introduce two ways of inducing an on-surface desulfurization reaction of a thiophene group embedded in the TCT molecule. The first approach, realized by elevating the temperature of the Cu(111) substrate, forces all of the molecules into a desulfurized state. In the second approach, the thiophene units are addressed individually with an STM tip. The two elementary steps of the reaction are induced using the electric field and the tunneling electron injection. With the help of the high-resolution imaging, we identified these steps as a subsequent splitting of the two C-S bonds of the thiophene group. As a result of the reaction, a desulfurized molecule is obtained, which is anchored to the Cu(111) surface atoms. A 50 % increase of the electrical conductance measured through the molecule is obtained after the reaction.

4.1 Tetracenothiophene on Cu(111)

The TCT molecule consists of four benzene rings (tetracene part) and one thiophene group, which replaces the first benzene group of a pentacene molecule (Fig. 4.1).

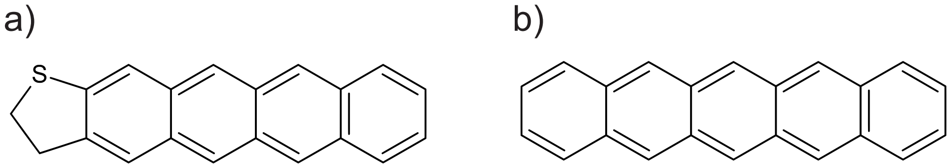

Figure 4.1 **a)** TCT structure. **b)** Pentacene structure.

We use the Cu(111) surface as a substrate. It is cleaned by repeated Ar^+ sputtering (1.3 kV, 10-40 min) followed by annealing (1 minute at 800 K). The TCT molecules synthesized as described in [210] were then thermally evaporated onto the precooled Cu(111) surface (200 K) until coverage of below half a monolayer was reached. The Knudsen cell containing the molecules was heated up to 500 K and evaporation was carried out after stabilizing the temperature for 30 minutes, ensuring proper thermalization of the cell and its contents. Afterward, the sample was moved to STM. The TCT molecules adsorb along the three [101] axes of Cu(111) and do not cluster (Fig. 4.2 a)). A single TCT molecule shows the topographic appearance of an asymmetric dumbbell, with the brighter lobe corresponding to the thiophene end (Fig. 4.2 b)).

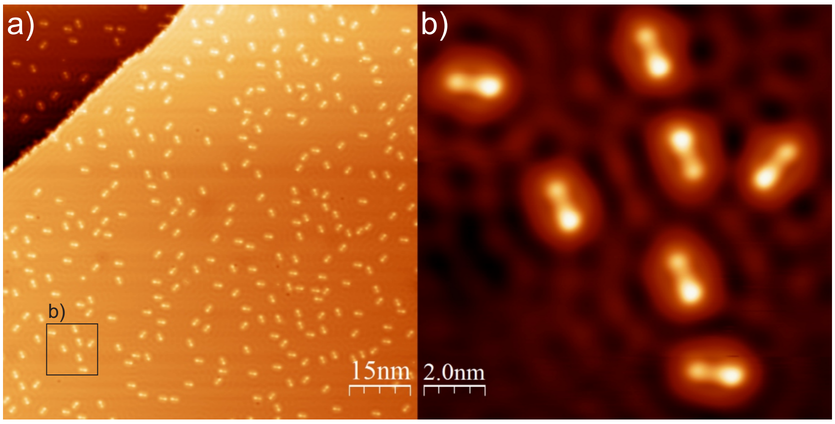

Figure 4.2 Constant current images of the TCT on Cu(111), recorded with metal tip. Set point: 100 pA, 100 mV. **a)** Overview image of Cu(111) with adsorbed TCT. The molecules follow the crystallographic axes of the surface and do not cluster. **b)** Zoom of the area indicated in a). TCT shows the appearance of an asymmetric dumbbell.

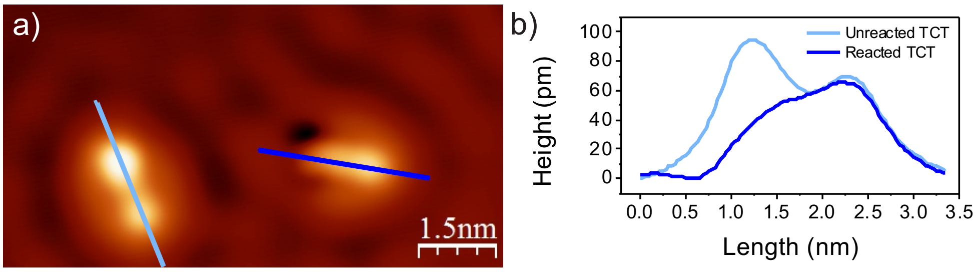

Figure 4.3 a) Constant current image of two TCT molecules, of which the left one is intact and the right one is a species encountered after the evaporation on the substrates at the elevated temperatures. Recorded with a metal tip. Set point: 100 pA, 100 mV. **b)** Line profiles marked at a).

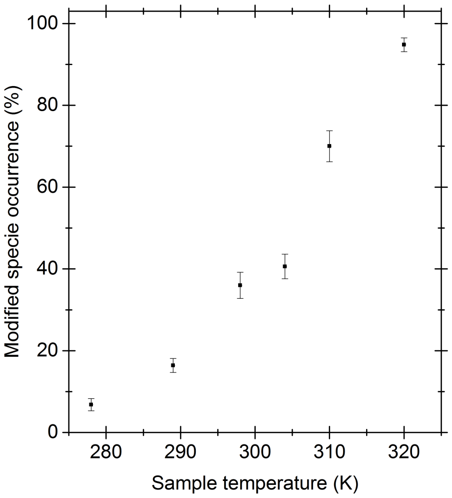

Figure 4.4 Percentage of the modified TCT molecules on the surface as a function of the temperature of the sample during the evaporation.

The molecular conformation of TCT adsorbed on the surface is strongly influenced by the temperature of the sample during the deposition. Above 270 K, a second state of the molecule is observed (Fig. 4.3 a)). It has a different topographic appearance: one of the lobes is gone and is replaced by a narrow, curved feature with a low-intensity spot on its side. The other lobe remains unchanged, having the same size and height (Fig. 4.3 b)) as the feature at the tetracene side of an intact TCT molecule. Taking into account previously reported reactions of thiophene groups with copper [211], as well as the thermally induced reactions on different metal surfaces [114], it can be assumed that the thiophene ring embedded in the TCT molecule undergoes structural changes upon adsorption on Cu(111) at elevated temperatures. Furthermore, the stability of pentacene on Cu(111) suggests that the tetracene side of the molecule stays intact. The ratio of pristine TCT and the modified species on the surface can be tuned by changing the temperature of the sample during the evaporation. Below 270 K not a single modified species is observed and above 330 K nearly all TCT molecules are modified (Fig. 4.4).

4.2 Electric field driven local reaction

In contrast to thermal activation, the modified state of the TCT molecule can also be attained locally. In order to induce the reaction of a single TCT molecule, the STM tip is precisely positioned above the thiophene group, as indicated with the blue circle in Fig. 4.5 a) and a short voltage pulse is applied. It creates a strong electric field in the tip-sample junction and injects electrons into the system (Fig. 4.5 b)). The final state of the molecule, equivalent to the final state achieved with thermally induced reaction, can be attained in two reaction pathways, differing by the action of the applied stimuli.

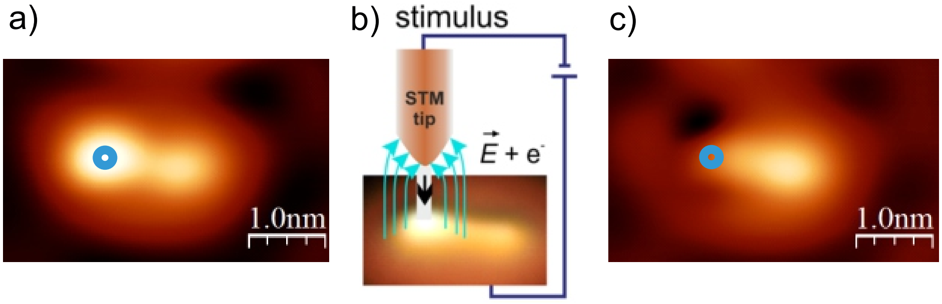

Figure 4.5 **a)** The intact TCT molecule. Tip position during the bias ramp marked with the blue circle. **b)** Stimuli present in the STM junction during the bias ramp. **c)** The TCT molecule after the locally induced reaction.

One of the pathways, labeled as **R**, prompts the molecule from the initial state **1** directly into the final state **2** (Fig. 4.6 a), purple arrow). In the second pathway, a two-step reaction through an intermediate state **1i** is followed. The two steps are labeled as **RI** and **RII** (Fig. 4.6 a), blue arrows). The intermediate state **1i** is obtained by applying a voltage pulse above 5.5 V at the 2 nm tip-sample relative distance (**RI**). Similarly to the initial state, the intermediate state has the topographic appearance of a dumbbell. Furthermore, a low-intensity feature is visible slightly off the center axis of the molecule (Fig. 4.6 b)), reminding similar feature visible next to TCT in the final state. The tetracene side of the TCT molecule in the intermediate state appears to be intact (Fig. 4.6 c)). The state **1i** can be further reacted to the final state **2** through the second reaction step **RII**. It is realized by applying a voltage pulse between 1.5 and 4.5 V. The exact value of the bias depends on the relative tip-sample distance in the 0 - 1.25 nm range, where 0 is defined by stabilizing the tip at 100 pA, 100 mV setpoint and approaching by 220 pm. This position corresponds to a tunnel resistance of 16.5 ± 1.2 MΩ.

Different relative tip-sample distances, at which the reactions **RI** and **RII** occur, indicate that **RI** and **RII** differ by the importance of the electric field and the electron injection. At sufficiently large tip-sample distances, such as required for **RI**, the tunneling current is negligible and, thus, the electric field is the dominating stimulus during a bias pulse. Lowering this distance increases the tunneling current so that the electrons can be injected into the system. The

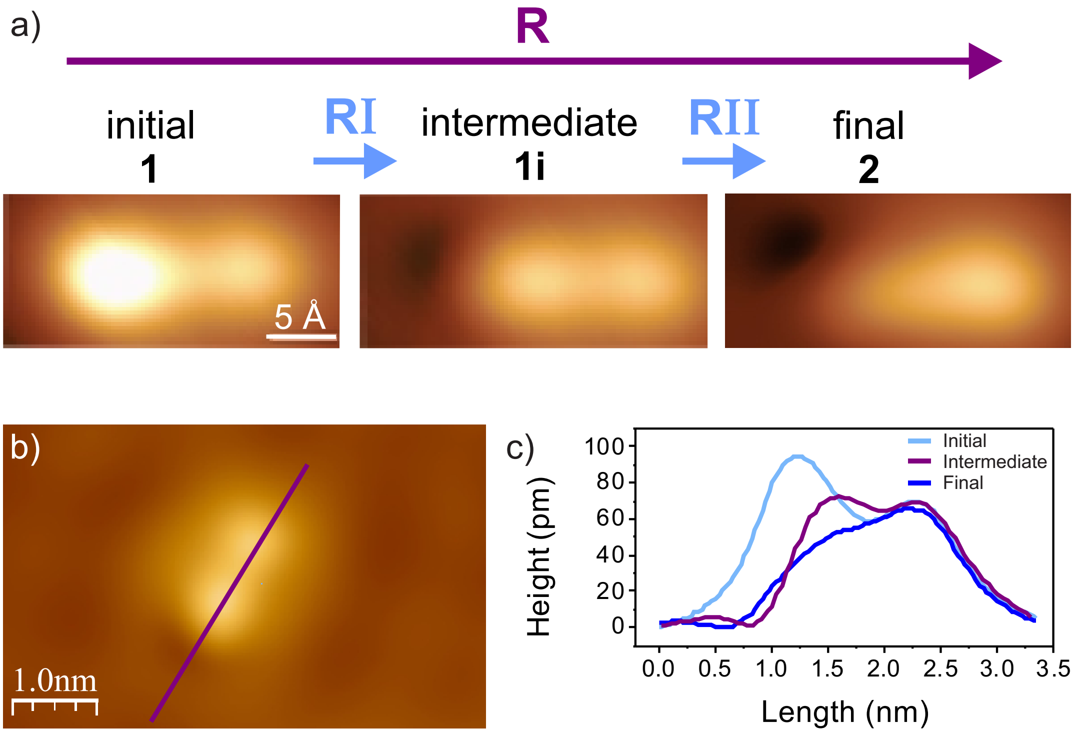

Figure 4.6 **a)** Constant current images of initial, intermediate and final states with arrows indicating the reaction pathways. Setpoint: 100 pA, 100 mV. **b)** TCT in the intermediate state. **c)** Line profile of the molecule depicted in b), compared with line profiles of the initial and final states.

steps **RI** and **RII** can be associated with these two different regimes. We have found an exact experimental procedure to trigger the **RI** step. First, an image of TCT in state **1** is acquired and the tip is positioned above a thiophene moiety at the 0 relative tip-sample distance, as defined above. Afterward, the tip is retracted by 2.2 nm and a short (minimum 100 μs) pulse of 6 V is applied. During such a voltage pulse, the tunneling current value is negligible as it is in the noise level of the current amplifier, 300 fA. Therefore, it is confirmed that the electric field is the dominant, possibly sole stimulus of **RI**.

As already mentioned, the step **RII** can be activated with a voltage pulse in a shorter distance regime. The experimental procedure is similar to **RI**, with an exception of shorter tip-sample distance. In this regime, the tunneling current is not negligible and we are able to detect the current changes associated with the induction of the reaction step **RII**. We have recorded I(V) curves of the bias ramps at different relative distances from the 0 - 1.25 nm range (Fig. 4.7 a)). The step-like features in the I(V) traces indicate the transition from the state **1i** to the final state **2**, what is confirmed by the STM images acquired after the bias ramps. The tunneling current and the bias voltage threshold values, at which the reaction **RII** occurs, are marked with (I_R, V_R). The summary of the V_R values shows, that V_R follows a linear dependence on the tip-sample relative distance (Fig. 4.7 b), solid circles), which is a hallmark of an electric-field-driven process [96], [99]. This dependence has a slope of 2.27 ± 0.07 V/nm and it represents the value of the electric field necessary to activate the reaction **RII**, which, as compared to

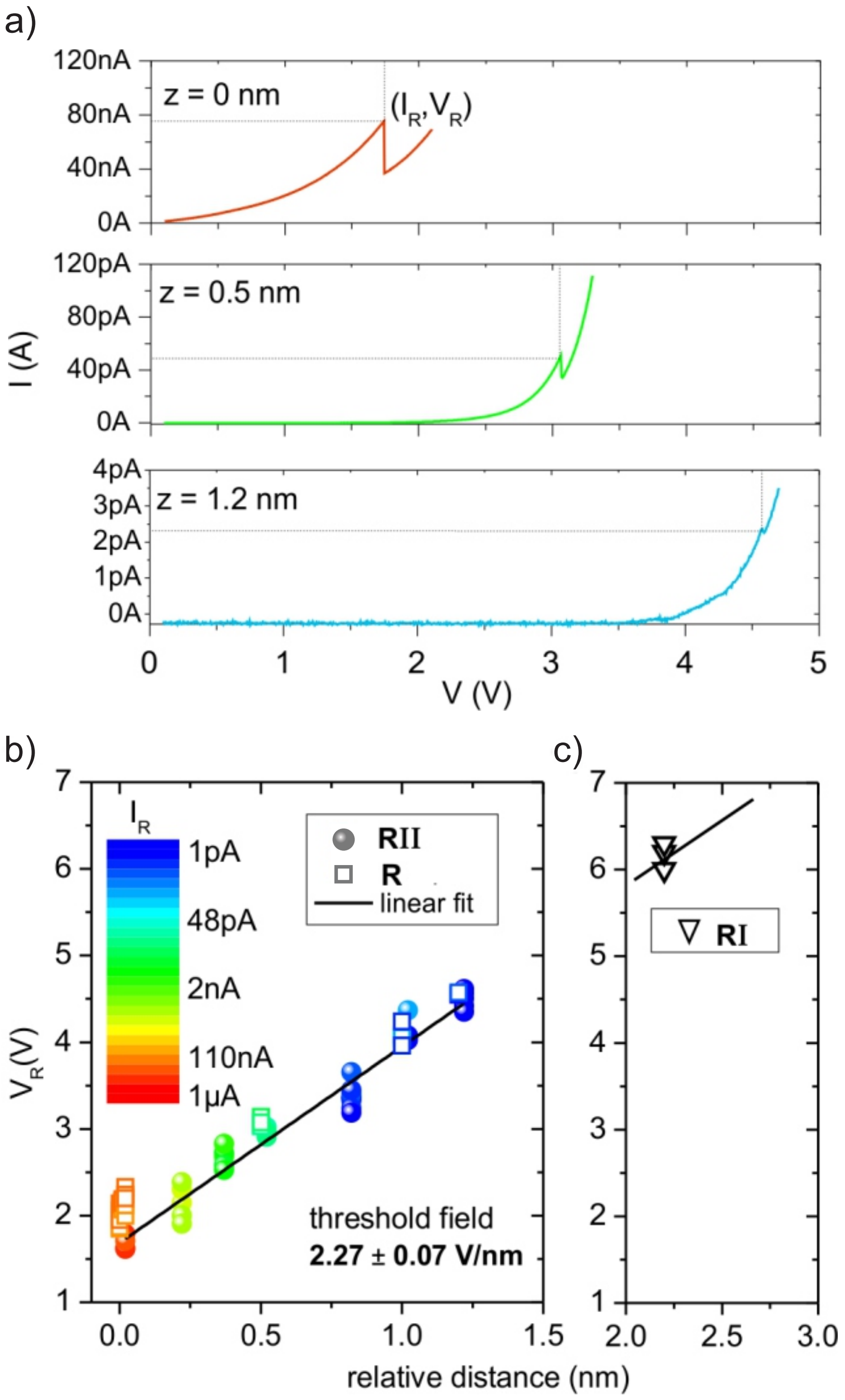

Figure 4.7 **a)** Tunneling current recorded during the reaction inducing bias sweeps. **b)** Dependence of the threshold voltage of the reaction steps **RI** and **RII** on the tip-sample relative distance. The linear dependence is characteristic of an electric field driven effect. The threshold field was calculated from the linear regression. **c)** Extrapolated threshold voltages of the reaction to the intermediate state in the distances, where the tunneling current is negligible.

RI, requires an additional injection of electrons into the molecular system. Therefore, the reaction step **RI** is an example of pure electric field effect in the STM, while the step **RII** is a mixed electric field - electron injection process [212]. The parameters, which we used to trigger the **RI** step are plotted in Fig. 4.7) c). These values follow the exact linear dependence observed for **RII**. It implies that both the steps **RI** and **RII** require the same critical value of the electric field.

If the voltage pulse in the short tip-sample distances regime is applied on TCT in the initial state **1**, it can be directly transited into the final state **2** (pathway **R**). The (I_R, V_R) values obtained from the I(V) traces recorded during the bias ramps triggering the reaction **R** have been plotted in Fig. 4.7 b) as empty squares. V_R follows the same dependence as in the case of **RII**, which means that a critical field of the same value is required to trigger reaction through the pathway **R** and the threshold electric field required for **R**, **RI** and **RII** is identical. Taking into the account that the product of both the pathways **R** and **RI** + **RII** is equivalent and inducing the reaction **R** fulfills the electric field requirement of **RI** and **RII**, as well as the electron injection requirement of **RII**, we conclude that **R** = **RI** + **RII**.

Every state of the TCT molecule was stable at 4 K and every reaction was irreversible. Moreover, all of the states were only accessible with positive polarity of the electric field from the surface to the tip apex. The electric field value, $2.27 \pm 0.07\ \mathrm{V\,nm^{-1}}$, was obtained by treating the tip-sample gap as a simple plate capacitor. In the STM tip-sample gap, the highest electric field is present directly below the apex of a metallic tip (thus at this position the electric field reaches the threshold values the fastest) and its value at this certain position can be approximated with plate capacitor model [213]. A proof of the correctness of this assumption is in the linear behavior of the threshold voltage V_R with respect to the tip-sample relative distance.

4.3 Identification of the reaction product

The STM imaging performed with a metallic tip, even atomically sharp, does not provide a resolution high enough to identify the newly acquired molecular structure. Considering the thiophene's chemistry on the metal surfaces, it can be assumed that the reaction includes a scission of the C-S bonds [114], [214]–[217], however a full structural identification with higher spatial resolution is necessary. Thus, we decided to perform imaging with a TCT terminated tip. First, the molecule in each state was imaged with a metallic tip (Fig. 4.8 a)). In the next step, the tip was functionalized with an intact TCT molecule, picked up from the Cu(111) surface by positioning the tip above the thiophene group and approaching it with a constant voltage of 100 mV. At a certain distance, a drastic increase in current is observed, indicating a jump-to-contact. Afterward, the tip is retracted, lifting the molecule off the surface. The imaging with the TCT-functionalized tip allows resolving the spatial distribution of density of states corresponding to the surface-modified molecular orbitals. As the molecule does not always adsorb on the tip apex in the same geometry, the resolution of the images may vary.

Each investigated molecule is imaged in constant height mode, with the STM Z-feedback

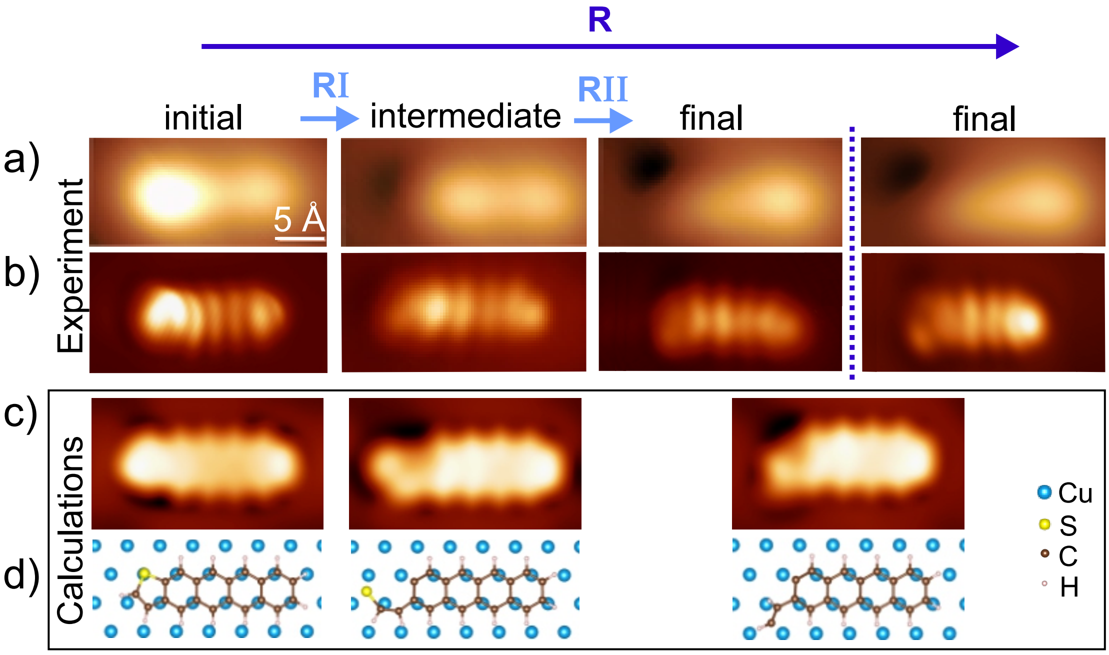

Figure 4.8 Comparison of acquired high resolution orbital images with simulations. **a)** The initial, intermediate and final states (final obtained by both **RI** + **RII** and **R**). Images acquired with metal tip, set point: 100 pA, 100 mV. **b)** High resolution orbital images recorded with the TCT functionalized tip in constant height mode. Tip stabilized above the topographically highest parts of the molecule at setpoints: 100 pa, -1 V for the initial one; for the rest 100 pA, 100 mV. **c)** Appearances in the Tersoff-Hamman approximation obtained from DFT simulations. **d)** Ball-and-stick model of the molecular structures corresponding to the simulated images.

disabled after positioning the tip above the topographically highest part of the molecule (Fig. 4.8 b)). The images reveal lobe-like parallel features, characteristic for the shape of LUMO of a flat, π-conjugated molecules consisting of benzene rings [119], [218], [219]. Moreover, it is also confirmed that the final states acquired through different processes **RI** + **RII**, **R**, as well as through the thermally induced reaction, show identical structures. The high-resolution images that reveal the orbital shape were compared with on-surface DFT simulations, performed in collaboration with Andres Arnau and Rémy Petuya. The simulation results are depicted in Fig. 4.8 c) along with the corresponding molecular structures (Fig. 4.8 d)). TCT in the initial state resembles LUMO obtained by DFT for the adsorbed molecule (Fig. 4.8 c)). Due to the strong hybridization and charge transfer to the molecule, the energy of the LUMO is shifted close to the Fermi level (E_F), as observed before for other pentacene analogs [101]. The simulated STM images are in qualitative agreement with the experimentally obtained high-resolution images of the initial, intermediate and final states, thus they confirm the structural changes at the thiophene side. Moreover, the low-intensity feature appearing in the vicinity of the molecule is reproduced in simulations. The comparison of the acquired images with the calculated appearances of the surface-modified LUMO allows us to assume that the reaction consists of the subsequent breaking of the two C-S bonds and splitting of the S atom away from the molecule. Moreover, an opening of the C-S bonds suggests the formation of C-Cu bonds with Cu(111) surface atoms, as the molecule in the final state cannot be vertically manipulated from the surface anymore.

A comparison of the high-resolution images with DFT simulations confirmed the initial assumptions of the structural changes of the molecule. To further investigate the reaction and to achieve a full understanding of the acquired molecular conformations, the nc-AFM Pauli repulsion frequency shift images of the initial and final states were acquired and compared with the simulated images (Fig. 4.9). The imaging has been performed as described in section 3.4, with the same scanning parameters as the image b) in Fig. 3.24. The simulated frequency shift images are calculated with probe particle model [188], [220] on the basis of molecular geometries acquired by DFT by Pingo Mutombo, Pavel Jelinek, Andres Arnau and Rémy Petuya. We compare the image of the initial state (Fig. 4.9 a)) with the simulation of the intact conformation of TCT (Fig. 4.9 b) and c)) and the image of the final state (Fig. 4.9 d)) with the simulation of TCT, where the thiophene ring has been opened by breaking a single C-S bond (Fig. 4.9 e) and f)).

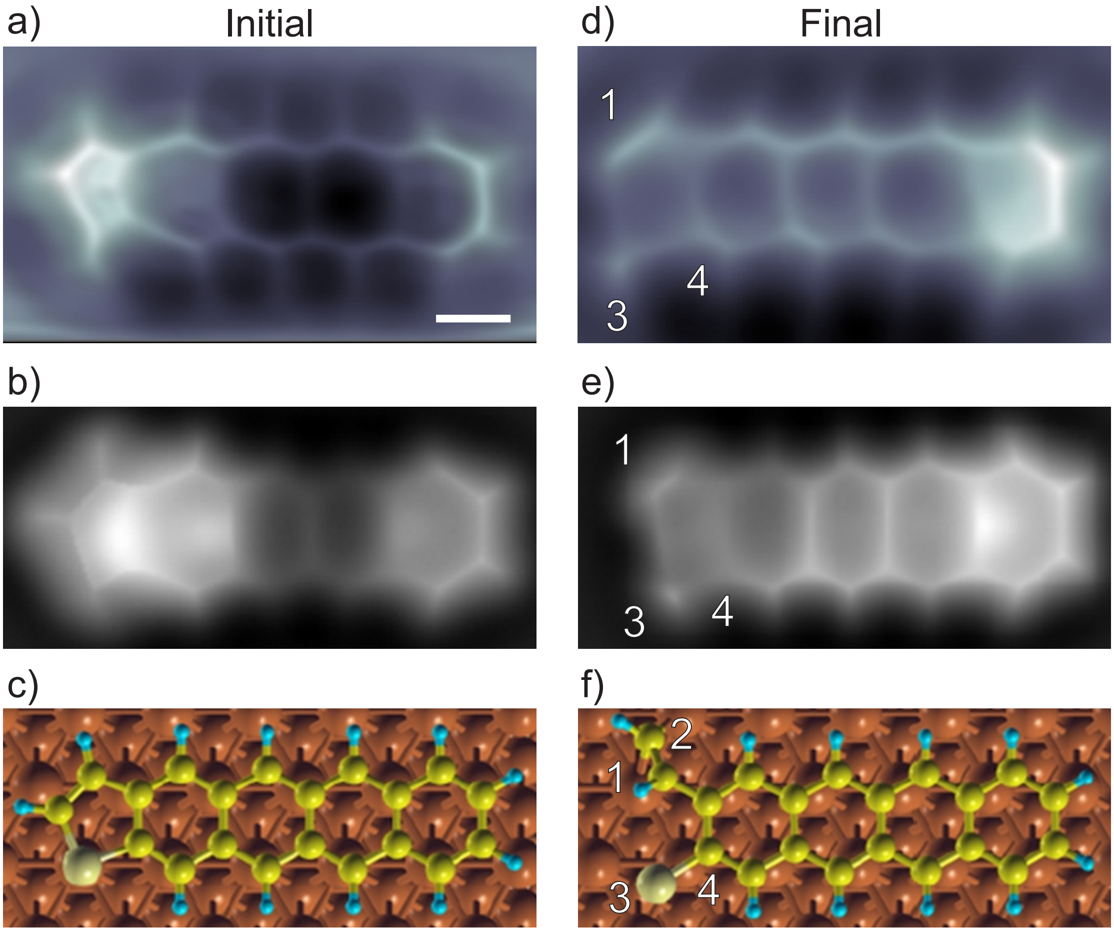

Figure 4.9 Comparison of Pauli repulsion images with simulations (probe particle model). Scale bar 2 Å. **a)** The initial state of the molecule, frequency shift image recorded with both phase and amplitude feedback enabled and CO terminated tip. Set point: 150 pA, 10 mV. The bias voltage during image acquisition: 1 mV. **b)** The image of the potential of the initial state of the TCT molecule, simulated with the probe particle model on the basis of the DFT obtained geometry. **c)** Model structure corresponding to b) **d)** The final state of the molecule, image parameters identical to a). **e)** Potential image of the final state of the TCT molecule, obtained using the same techniques as b). **f)** Model structure corresponding to e).

In the Pauli repulsion image, the initial conformation of TCT resembles that of the molecule in the gas phase. Both terminals are slightly lifted from the surface, which is characteristic for pentacene and its analogs adsorbed on metal surfaces [48], [101]. We found near perfect agreement between the experimental data and the probe particle simulation of the initial state of the TCT, which again confirms that the molecules land intact on Cu(111).

In the image of the final state of TCT, a change is observed at the side of thiophene moiety after the reaction. The tetracene part, as previously assumed, stays chemically intact and the reaction concerns only the thiophene functional group. The feature labeled as **1** in Fig. 4.9 d), e) and f), arises from the H atom attached to the first C atom of the alkyl chain (that had previously formed one of the sides of the thiophene group). As the H-C bond points upwards, the H atom is uplifted and gives rise to a high-intensity feature, what is resolved in both the experiment and probe particle simulations. The rest of the alkyl chain (**2** in Fig. 4.9 f)) is not resolvable in both the experiment and simulations because the second C atom is bonded to the Cu(111) surface, making the rest of the chain point downwards. The agreement between the theory and the experiment concerning the appearance of the alkyl chain confirms the scission of one of the C-S bonds and the opening of the thiophene group.

Comparing the experimental and simulated images reveals a disagreement in the position of the S atom (**3**). In the simulated potential map (Fig. 4.9 e)), where one of the C-S bonds is retained, the length of the ridge feature between the S atom and the closest C atom (**4**) is ~1.7 Å. This value is in agreement with both the experimental and theoretical literature data concerning the length of covalent C-S bonds (~1.85 Å) [221], [222]. A slight difference occurs most probably due to the fact that the structure is not ideally flat and its parts might be slightly tilted in the Z axis, what shortens the appearance of the feature in the two-dimensional image. The length of the corresponding feature measured at the experimental image (Fig. 4.9 d)), ~2.3 Å, is ~25 % bigger than the literature value. Therefore, the experimentally observed feature is too long to correspond to the C-S covalent bond. As the reaction can be carried through the two-step pathway, the most probable interpretation of this process involves separate dissociation of both C-S bonds, one after the another. Hence, it can be assumed, that the S atom is split apart from the molecule and, as suggested by the length of the feature **3**-**4** in the Pauli repulsion image, resides at the nearest hollow site of the top atomic layer of the Cu(111) surface.

A ridge between the features **3** and **4** may originate from the properties of the CO-functionalized tip used for the Pauli repulsion imaging and its observation does not need to indicate the existence of a chemical bond between the C and S atoms. In the Pauli repulsion imaging, the potential can be detected and summed from two or more atoms in close proximity. This may give rise to a feature of high intensity directly between them, where the sum of the potential is the highest, even if there is no direct chemical bond. In other systems, similar features were also misinterpreted, for example as corresponding to hydrogen bonding [182], [188], [220]. Another bond-like feature appears on both experimental (~2.8 Å) and simulated (~2.9 Å) data, between the S atom (**3**) and the feature associated with the upstanding C-H bond (**1**).

Those values are over 50 % higher then the length of covalent C-S bonds, thus again they cannot correspond to a direct chemical bond. Therefore, rigid, bond-like features can appear on the frequency shift images even in the absence of a direct chemical bond and their intensity depends, among other factors, on the distance between the two sources of potential [188], [220].

In summary, the nc-AFM imaging confirmed the opening of the thiophene group. Although the theory does not reproduce the experiment in all the details, it is strongly suggested that the S atom is split apart from the molecule and positioned at the nearest hollow site of Cu(111) after the reaction. Two covalent C-Cu bonds to the Cu(111) surface are formed as a consequence of the opening of the thiophene moiety. The rest of the molecule, the tetracene part, is not chemically altered.

4.4 Mechanism of the two-step reaction

With the resolved structure of the TCT molecule in the final state and the reaction inducing stimuli identified, the following mechanism is concluded with the help of theoretical calculations. The adsorption of thiophene moieties on the surfaces of different metals tends to lower the activation barrier of the desulfurization process. It has been proven already that this reaction can be induced thermally [114], [214], [215]. Upon adsorption of the TCT molecule on the Cu(111) surface, an electron transfer from the metal to the molecule occurs, which corresponds to populating the LUMO by one additional electron, as depicted in Fig. 4.10 a). This state of the molecular orbital is called a surface-modified LUMO (Fig. 4.10 b) upper panel).

The first step of the reaction, **RI**, is induced by the electric field above 2 V nm^{-1}, oriented from the sample towards the tip. An applied electric field disturbs the energy position of the surface-modified LUMO, which may further lower the energy barrier of the desulfurization reaction. Moreover, the electric field interacts with the intrinsic dipole of the thiophene group. The S atom is positively charged (0.2 e) and two neighboring C atoms are charged negatively (-0.16 e and -0.29 e). Under the influence of the field, the forces act on the charged atoms, pulling the S atom upwards, towards the tip and repelling the C atoms towards the sample. The C-S bonds are elongated, up to the moment when one of them breaks, removing one of the constraints from the S atom and rendering the molecule into an intermediate state (Fig. 4.10 c)). The remaining C-S bond is much more flexible after breaking of the first one and the charge is redistributed (Fig. 4.10 d)). The energy barrier of 0.9 eV for **RI** was calculated and is in agreement with the different theoretical predictions of the influence of the electric fields on the C-S bonds [223], as well as with the experimental findings concerning the different electric field driven processes [94], [96], [99], [224]–[227].

The second step of the reaction, **RII** can be induced with the electric field of the same polarity, with an addition of the injection of tunneling electrons. The influence of the electric field is similar to the reaction **RI** - the charge redistribution of the system lowers the energy barrier

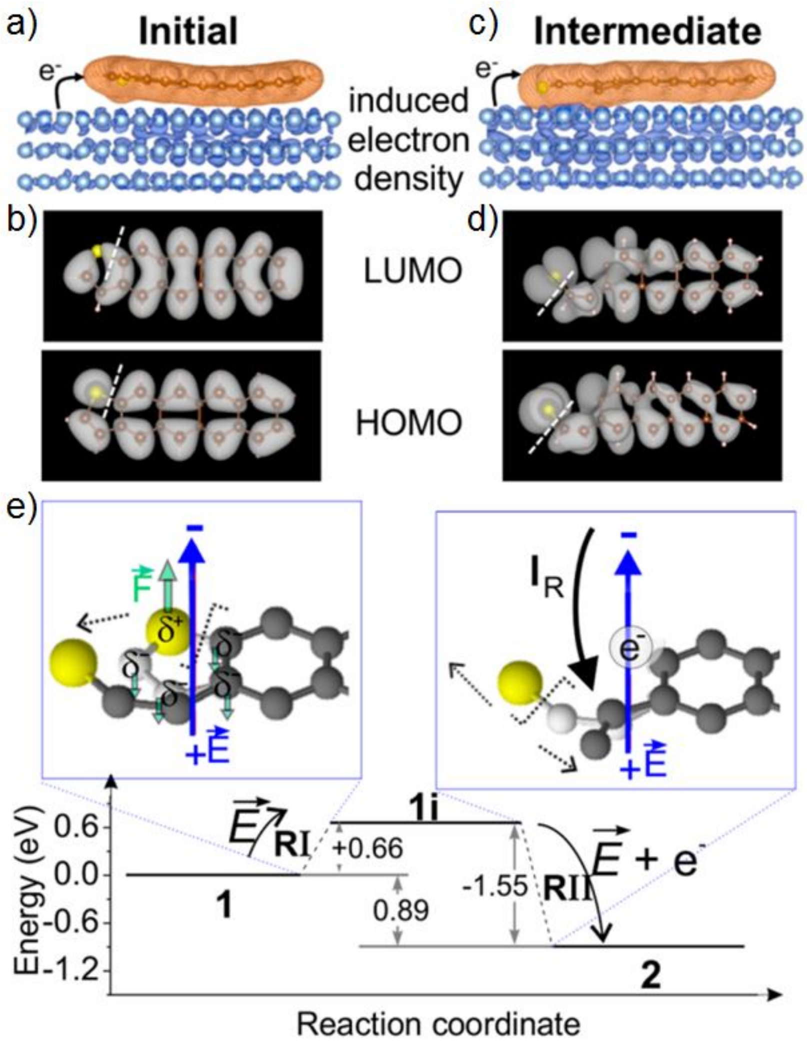

Figure 4.10 The effect of the electric field on the two-step reaction mechanism **a)** Simulated induced electron density of TCT on Cu(111). Upon adsorption, an electron transfer from the metal surface to the molecule occurs, modifying the LUMO. **b)** Simulated orbitals of the intact TCT molecule: surface modified LUMO (upper panel) and HOMO (bottom panel). **c)** Simulated induced charge density of the intermediate state of the TCT molecule. **d)** Calculated orbitals of the intermediate state: surface modified LUMO (upper panel) and HOMO (bottom panel). **e)** Energetic pathway of the two-step desulfurization reaction of the TCT molecule. The total energies of each molecular state are expressed with respect to the initial state. Left inset: overlapped structures before (light gray) and after (dark gray) the **RI** reaction. Right inset: overlapped structures before (light gray) and after (dark gray) the **RII** reaction. The S atom is split from the molecule. Bond scissions and changes of positions are marked with dotted lines. Blue and black lines correspond to the electric field and tunneling electrons, respectively. Green arrows indicate forces acting on the system due to the presence of the electric field.

of the process. The tunneling electrons are injected into the orbital of the intermediate state (Fig. 4.10 d), upper panel). Due to the additional population of the antibonding orbital, the probability of the scission reaction of the second C-S bond is increased, resulting in splitting the S atom from the molecule. Another option involves the coupling of the tunneling electrons to the vibrational states of the molecule and breaking of the bond. Within this model the reaction **R** = **RI** + **RII** is exothermic by 0.89 eV (Fig. 4.10 e)).

4.5 Changes of the electrical conductance

The changes of the TCT structure, both concerning the molecule itself and the nature of the contact to the surface, have a significant influence on the properties of the molecule. The mechanical anchoring of TCT to the Cu(111) surface atoms drastically improves. Before the reaction, the molecule can be picked up from the surface. After the reaction, the molecule cannot be lifted from the surface, nor laterally manipulated.

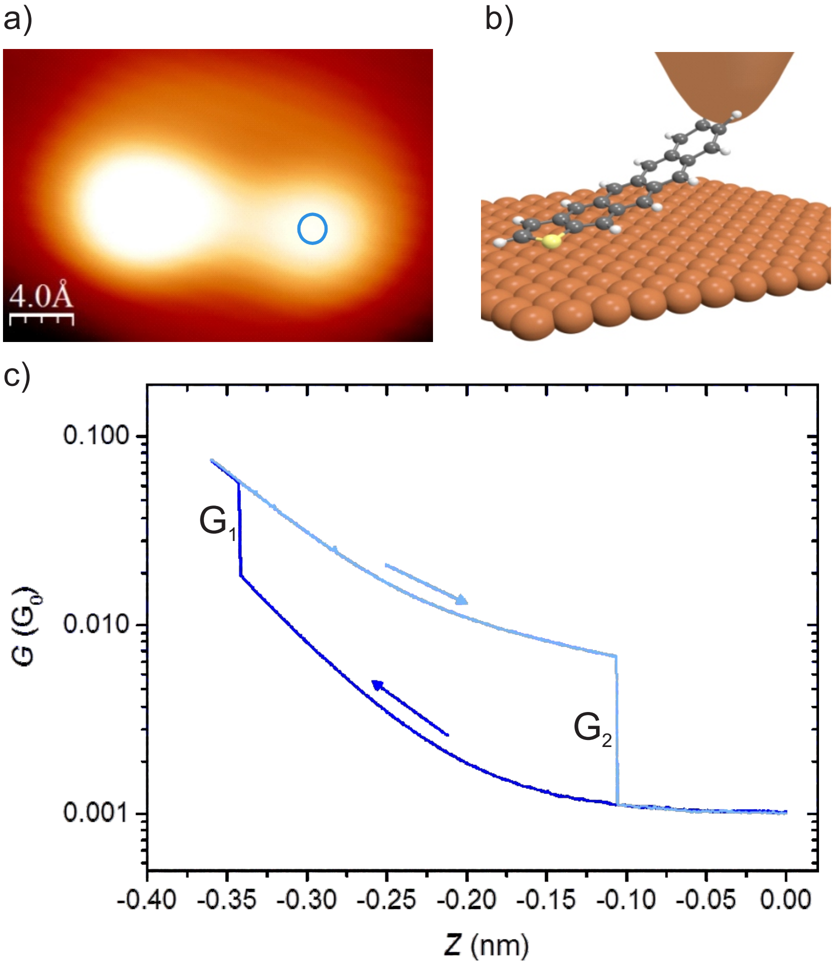

Figure 4.11 Methodology of a conductance measurement through a single TCT molecule. **a)** An intact TCT molecule is imaged and the tip is stabilized with 100 pA, 100 mV set point above the thiophene group, as indicated by the blue circle. **b)** Schematic representation of a single molecule suspended between the tip and the sample. **c)** Changes of conductance during the measurement. The recorded tunneling current is divided by the used bias voltage and expressed in units of the conductance quantum. Values G_1 and G_2, associated respectively with formation and breaking of the tip-molecule contact, represent the conductance of the suspended molecule and are obtained by subtraction of the tunneling current value before the change, subtracting it from the overall current value directly after the change and dividing by used bias voltage.

Another property affected by the structural changes in its electrical conductance, measured through a single molecule suspended between the STM tip apex and the sample. The technique is the STM controlled equivalent of a mechanically controlled break junction (BJ)

[228]–[230] and is well established in the SPM field [124], [231]–[234]. Compared to the classic BJ technique, the STM version does not offer the same acquisition speed but instead provides a higher precision of the measurement. The molecule can be localized and characterized with atomic precision and the contact with the tip can be created at the chosen position of a single molecule. Due to this capability, a single molecular junction with the desired geometry can be fabricated.

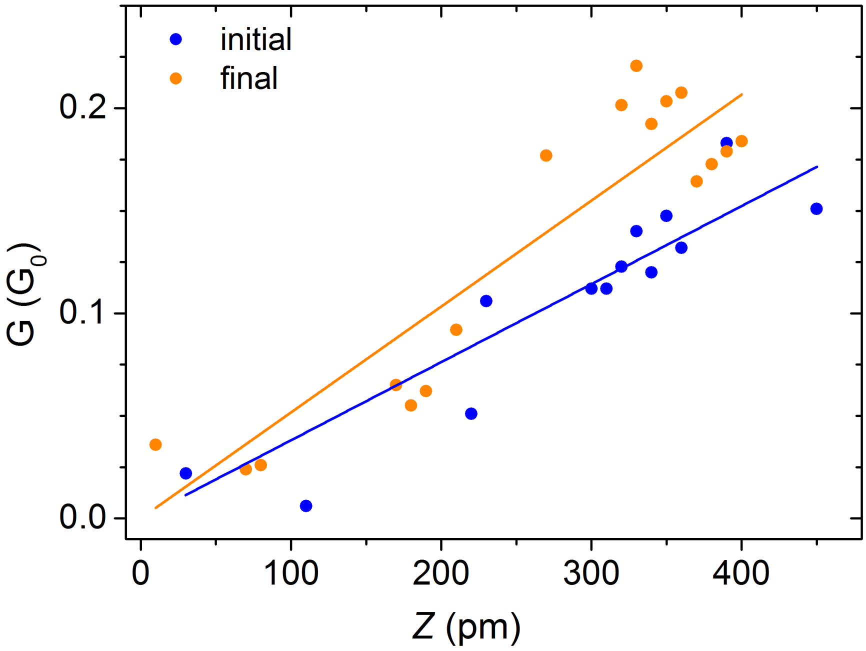

Figure 4.12 Conductance of the initial and final states of the TCT molecule as a function of the approach distance. The values have been averaged for each distance (±5 pm). Z-axis corresponds to the distance approached towards the sample, at which contact formation/break occurred. In the 0-400 pm range a linear behavior of the molecular conductance was observed for both initial and final states.

An experimental approach to the measurement of the conductance of a single not reacted TCT molecule is presented in Fig. 4.11. The tip is stabilized above the tetracene end of the molecule (indicated by a blue circle in Fig. 4.11 a)), with set point 100 pA, 100 mV. The STM feedback is switched off and the tip is moved towards the molecule by 400 pm. During the approach, the molecule snaps to the tip apex and is suspended between it and the surface (Fig. 4.11 b)). During this procedure, the current in the junction is recorded and upon formation of the contact, a drastic increase of its value is detected (giving rise to the change of conductance marked as G_1 in Fig. 4.11 c)). The tip is afterward withdrawn from the molecule in the same controlled manner. If the bonding of the end group to the metal surface is stronger than the bonding of the contacted group to the tip apex, the molecule will lose contact and return the surface, which is again visible in the recorded current as a drop in its value (corresponding to the conductance change G_2 in Fig. 4.11 c)). The changes in the current arise from the forming and breaking of additional conductance channels between the molecule and the tip electrode. After subtraction of the values of the tunneling current at the moment of contact formation/breaking, the current flowing through the single molecule is obtained. The values of those abrupt changes can be divided by the bias voltage and expressed in units of the conductance quantum G_0 = 77.5 μS, yielding the value of the conductance measured through the intact TCT molecule. An identical methodology is used for the TCT molecule in the final state.

The conductance change associated with contact formation and breaking depends on the geometry of the junction i.e. at which point during the approach/retraction the contact is formed/broken [82]. This distance cannot be directly controlled and the conductance measurements through the TCT molecules, both in the initial and final state, were repeated for multiple molecules. The result of those measurements is depicted in Fig. 4.12. The measured values were averaged for the distances at which the conductance change occurred (bin size ±5 pm). On average, the conductance of the molecule in the final state is higher than in the initial state and for both molecules, the dependence can be approximated with a linear fit. Direct interpretation of this behavior is not trivial, as forming a contact at different distances not only changes the length of the suspended molecule, but also the length of the part remaining on the surface and thus the hybridization and character of the interaction with the Cu(111) substrate. Therefore it cannot be interpreted as a simple extension of the length of the suspended molecule. However, it can be seen as a clear indication of a significant increase in electrical conductance measured through the molecule in the final state.

The values of the conductance measured through a single intact and reacted TCT molecule can be compared more directly in the narrow approach distance range of 50 pm. In this range, the highest number of conductance values was obtained, hinting of a most preferable distance for the contact formation for both states of the molecule (Fig. 4.13) that yields a comparable junction geometry for both states. Moreover, in this range (significantly smaller than the length of the whole molecule), the differences of the geometry of the molecular structure suspended between the electrodes have only a small influence on the conductance. It can be assumed that the distribution of the measured conductance values can be attributed to small differences in adsorption geometry of the tetracene termination on the tip apex.

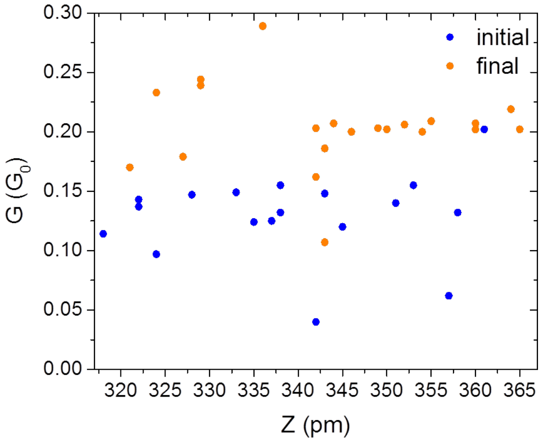

Figure 4.13 Distribution of conductance values for the 320 - 360 pm approach range for both initial and final states. Data points are not binned and not averaged. Z axis defined as in Fig. 4.12. In the range of 320-360 pm, the highest number of measurements was acquired, hinting a most preferable position, at which the contact formation occurs for both states of TCT. Each conductance value has been obtained from the measurement of a different molecule.

Conductance values depicted in Fig. 4.13 have been summarized in the form of histograms, fitted by Gaussian functions (Fig. 4.14). For the analyzed range, the conductance for the final state is ~50 % higher than the conductance through the intact molecule (Fig. 4.14 a)). We

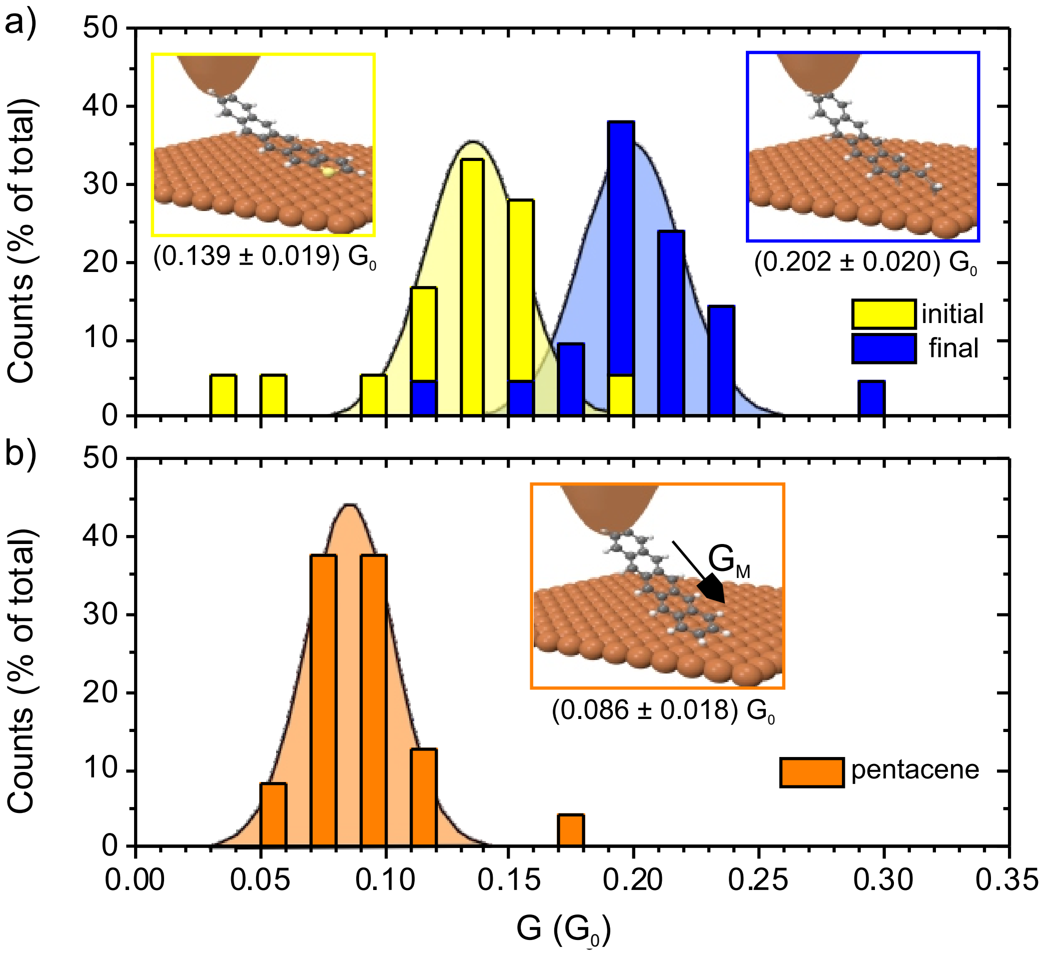

Figure 4.14 Comparison of the conductance for two states of TCT and pentacene. **a)** Conductance histograms of initial and final states of TCT. **b)** Conductance histogram for the pentacene molecular junction. The errors of the histograms' peak positions are standard deviations of Gaussian fits. Schematic representations of the molecular junctions during the conductance measurements are depicted in the insets. The numbers of the measurements for each position have been normalized to the total number of measurements for each species.

also performed measurements for pentacene molecules that reveal values lower than that of both states of TCT (Fig. 4.14 b)). The conductance measured in the STM-BJ technique is determined by three factors: the tip-molecule interaction, the internal resistance of the molecule and the molecule-sample interaction. As the moiety contacted by the tip is the same for both pentacene and two states of the TCT, it undergoes the same variations of the adsorption geometry at the tip apex. Therefore, the differences in conductance values for TCT in the initial and final states can be attributed to the modification of LDOS within the molecule and the changes of the interaction of the broken thiophene ring with the Cu(111) surface.

The simulated partial charge densities of each type of the molecule, obtained by integration of the energy around E_F, are depicted in Fig. 4.15 a). The distribution of the charge is similar for all of the molecules at the center and the acene termination. Qualitative differences are reported for the thiophene side. The desulfurization reaction results in an increase of the

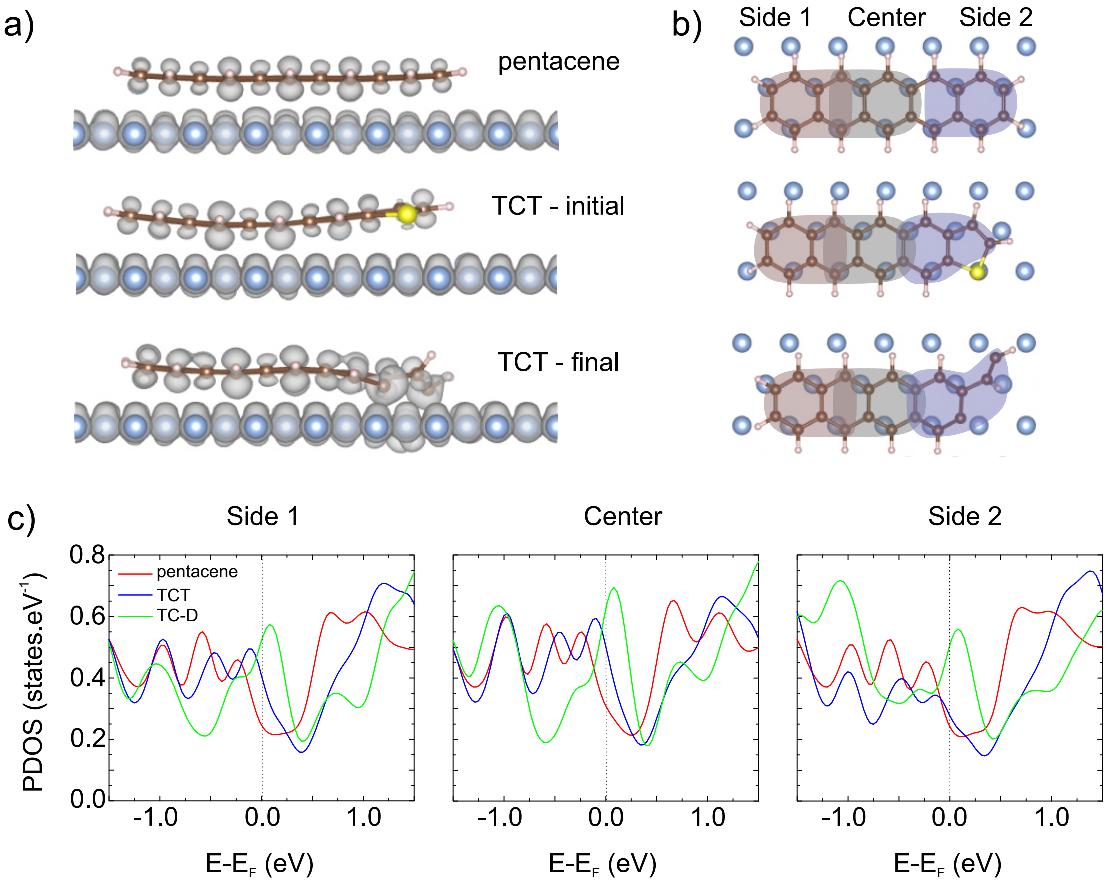

Figure 4.15 Electronic properties of pentacene and two states of TCT. **a)** Partial charge densities. **b)** Parts of the analyzed molecule used for projected density of states calculations. **c)** Projected density of states for the molecular parts marked in b).

overlap of the wave functions of the underlying Cu(111) surface and the desulfurized TCT molecule at the former thiophene group. This indicates the decrease in the TCT-Cu(111) contact resistance.

In order to understand the effect of the desulfurization reaction on the electronic structure of the molecule, the projected density of states (PDOS) of three types of molecules was simulated in collaboration with Andres Arnau and Rémy Petuya (Fig. 4.15 c)). PDOS was summed over atoms in three different parts of the structures, as presented in Fig. 4.15 b). A significant enhancement of PDOS close to E_F is observed at the thiophene side (side 2) of desulfurized TCT, as compared to the intact molecule. Furthermore, smaller enhancement of PDOS near E_F is reported at side 1 and center of the TCT molecule in the final state. This suggests that the reaction lowers the internal resistance of the TCT molecule itself. Hence, the increase of the conductance measured through the TCT molecule in the final state appears due to both lower contact resistance with Cu(111) and increased transmission of the molecule itself. On the base of experimental findings and theoretical predictions, it can be speculated that any specific transport calculations would yield similar results.

4.6 Conclusions

In this chapter, an on-surface desulfurization reaction of the thiophene group embedded in the TCT molecule was presented. The two steps of the local desulfurization reaction can be distinguished by first applying a voltage pulse at large tip-sample distances. The first step is activated only by an electric field stimulus and triggers the TCT molecule into an intermediate state. The second step of the reaction is realized by applying a voltage pulse at shorter tip-sample distances, both creating the electric field in the tip-sample junction and injecting the electrons into the system. The direct reaction from the initial to the final state can be induced by applying a voltage pulse at short sample distances, similarly to the second step of the two-step pathway. Therefore, the direct reaction from the initial to final states involves combined stimuli of an electric field and an injection of electrons and it fills the requirements of both reaction steps of the two-step pathway at the same time. It was concluded that both the direct and the two-step reaction pathways are equivalent and yield the same reaction product.

The high-resolution STM and nc-AFM images revealed that the reaction results in breaking of the thiophene group, splitting of the S atom from the TCT molecule and forming of two covalent C-Cu bonds to the Cu(111) surface. The induced change of the molecular structure resulted in an improved mechanical anchoring of the molecule to the surface, as well as in a 50 % increase in the electrical conductance measured through the molecule. The desulfurization of the thiophene group can also be induced on a global scale by elevating the Cu(111) sample temperature to 330 K. Both global and local scale approaches result in mechanical and electrical anchoring of the TCT molecule. Taking into account that the thiophene functional group can be attached to a wide array of organic structures [235]–[239], a thiophene-Cu(111) system might be an alternative to thiol-Au electrode anchoring in the field of single-molecule electronics [240].

5 Hyperthermal reactions of Reichardt's Dye

The on-surface chemical reactions of organic molecules can be induced in local and global scales. In the previous chapter, two different approaches to desulfurization reaction were presented. The local one involved addressing single molecules with the STM tip and the global one involved an elevation of the temperature of the sample. The catalytic effect of metal support combined with the thermal energy of the surface resulted in spontaneous activation of the process on the whole substrate. Although thermal activation by the elevation of the sample temperature is the most common approach to on-surface chemistry [112], [241], other options are also available. One of the possibilities is to utilize the kinetic energy of the incident particle [242], e.g. in a controlled collision process of a gas phase molecule with the surface. In the regime of low kinetic energies, below 1 eV, the molecules land in a non-destructive manner [243]. In this case, the state of the resulting adsorbate depends on its intrinsic properties: chemical reactivity, bond stability, mechanical flexibility, and the properties of the surface: temperature, reactivity, catalytic behavior [244]. At high kinetic energies, more than 1 keV, the collision of atomic ions can no longer be described as an interaction only with the outer atoms of the surface, as the impact results in the penetration of more than one atomic layer of the substrate. A collision of molecular ions at this energy results in the destruction of the molecule or scattering without adsorption.

The events where ionized molecules collide with an energy in the intermediate regime (1-1000 eV) may induce selective bond breaking and on-surface reactions as the energy is high enough to surpass the activation energies [243]. Upon landing of the molecule, the energy needs to be dissipated in a short time, resulting in a non-equilibrium thermal process [245]. In addition, the energies of the hyperthermal processes are far larger than the available thermal energies provided by the surface (e.g. ~0.026 eV for 300 K). The distribution of the kinetic energy is not even and depends on the geometry of the molecules during the collision event [245]. Therefore, landing with high kinetic energy may surpass the reaction barriers not accessible through the on-surface induced thermal reactions and classic thermal equilibrium chemistry, leading to the acquisition of new structures and conformations of organic molecules [243], [246], [247]. Exploring this possibility is the main goal of the study presented in this chapter.

Molecular ion beams can be controlled and targeted, with desired kinetic energies, at metal surfaces using the electrospray ion beam deposition (ES-IBD) technique. It is capable of performing the soft (without alteration of the molecular structure) and reactive landing of both volatile and nonvolatile molecules, including large species. As the spectroscopic chemical analysis of the molecules on strongly adsorbing surfaces is challenging, the preferable way of analysis of the products of these reactions is to investigate them directly on the surfaces in real space. With this approach, realized by the SPM techniques, information about structure, morphology, abundance and chemistry of the resulting species can be obtained.

In this chapter, we present a study of the reactive landing of Reichardt's Dye (RD). The main goal is to explore the ability of the non-equilibrium process to unlock new reactions and reaction pathways. We intend to check, if the hyperthermal collision of RD with the Cu(100) surface yields species unobtainable by the means of thermal activation of RD adsorbed in the intact form on the same surface. First, we utilize ES-IBD to obtain the intact RD on Cu(100) and analyze its morphology. The thermal activation is carried out by annealing the substrate with soft-landed RD. The reaction products are identified with high-resolution STM and the Pauli repulsion nc-AFM imaging. In the next step, we perform ES-IBD reactive landing of RD on Cu(100) and investigate the obtained species again with combined STM/nc-AFM. The results presented in this chapter concerning the comparison of the structures obtained through both approaches indicate the existence of thermally unobtainable species after the hyperthermal collision, thus, they confirm the unique opportunities provided by ES-IBD reactive landing.

5.1 Electrospray ion beam deposition (ES-IBD)

The standard approach to an in-vacuum deposition of organic molecules is in-situ thermal sublimation (evaporation) and condensation at the targeted surface. Upon heating to sufficiently high temperature, volatile molecules enter the gas phase and are emitted from the evaporator cells. The molecules travel towards the surface directly, as in the vacuum they do not undergo collisions with the background gas and the mean free path is on the order of the size of the vacuum chamber itself. This relatively simple technique has been used for the deposition of the TCT molecules described in Chapter 4.

The thermal sublimation deposition technique is easy to implement, but it is also limited. One of the main drawbacks is that the thermal evaporation of fragile molecules cannot be carried out, as they will undergo fragmentation before reaching the sublimation temperature. This is observed for the majority of macromolecules, including those with biological importance, e.g. proteins and carbohydrates. Moreover, alternative deposition techniques based on solution processing, like spin coating or drop casting, lack the cleanliness and coverage control crucial for the single-molecule experiments. ES-IBD overcomes limitations of both thermal sublimation and solution-based methods, as it provides control over the type and quantity of the deposited substance, and is compatible with a wide range of organic molecules [248], [249].

5.1.1 Electrospray Ionization

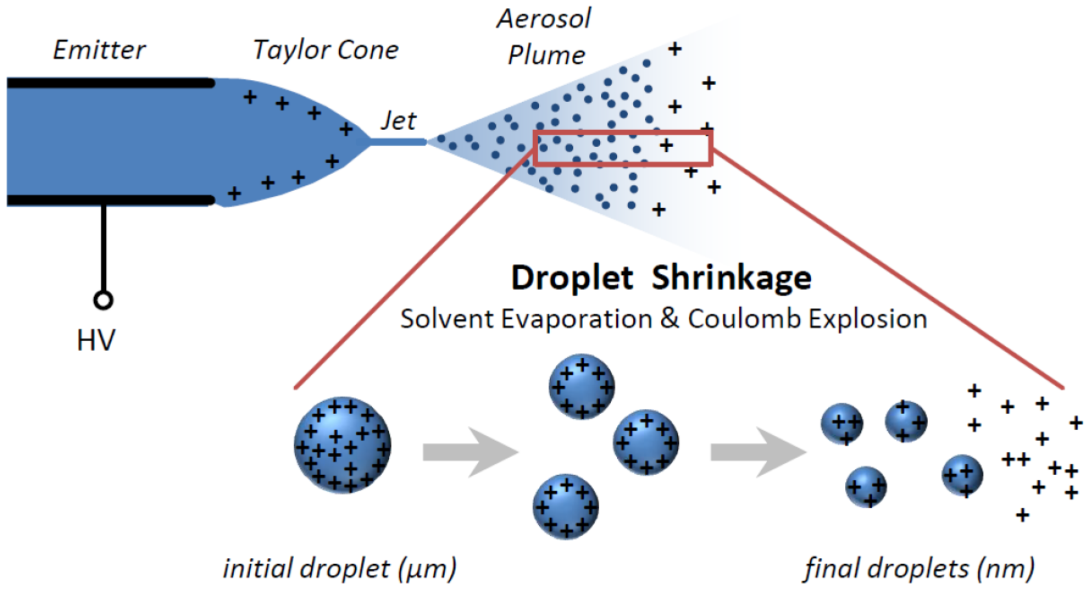

Figure 5.1 Electrospraying from a capillary. A Taylor cone formes at the opening of a capillary. A jet of accelerated ion clusters is formed, which shrinks and desolvates during the flight (after Rinke [250]).

In the ES-IBD technique, molecules are handled in the gas phase as intact molecular ions. They are obtained with the means of electrospray ionization (Fig. 5.1) [251]. It utilizes an emitter capillary with an opening of below 100 μm, into which the solution of molecules is fed. A high voltage is applied to the capillary and a Taylor cone is formed at its opening [252], from which small, highly charged droplets are emitted. The solvent is evaporated from the droplets, which eventually reach their Rayleigh limit. As the surface tension holding droplets together becomes weaker, the Coulomb repulsion becomes stronger and Coulomb explosions occur, quenching the smallest droplets [253]. This leads the system to a point, where the generation of completely desolvated ions is advantageous to reduce the repulsive forces. They reach it without fragmentation because the generation of the gas phase ions depends on the electric fields rather than thermal excitation. Electrospraying is usually performed in ambient conditions, but can also be carried out in a vacuum. The acquired ion cloud of intact molecular ions can be analyzed, e.g. with mass spectrometry, or further processed to perform deposition.

5.1.2 Experimental realization

The ion cloud is introduced, in form of a beam, into the vacuum chamber and travels through 2 mm apertures in six differentially pumped vacuum stages, at the end reaching UHV conditions (Fig. 5.2). During the flight, it is collimated and focused by ion optics. The beam passes through a mass selecting quadrupole, which allows bandpass m/z (mass to charge ratio) filtering [254]. The resulting composition of the beam is analyzed with a time-of-flight mass spectrometer

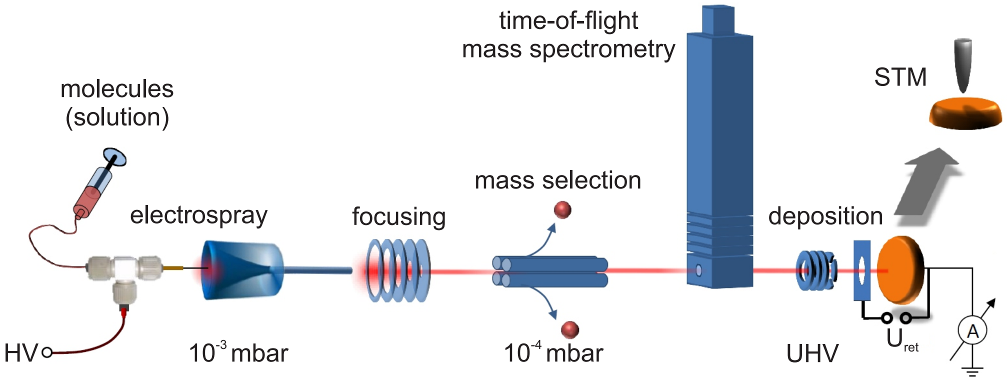

Figure 5.2 Schematic drawing of an ES-IBD technique. Starting vacuum of 10_{-3} mbar is pumped down to UHV 10_{-10} mbar in 6 differentially pumped stages.

(TOF-MS). The mass selecting quadrupole can be adjusted to pass only the desired molecule and charge state, ensuring a pure beam, which can be deposited on the surface. The high purity is especially required for the samples investigated by STM, as the on-surface identification of different species present in the non-uniform beam may be challenging.

5.1.3 Soft landing and reactive landing

The energy of the molecular ions colliding with the surface can be controlled with a voltage applied directly before arrival at the sample (U_{ret} in Fig. 5.2). An electric field is needed to slow down the beam in order to perform a soft landing, where the state of the adsorbate is not affected by the collision. The polarity of the applied field depends on the charge state of the molecule, e.g. positive bias at the sample if the molecules are in positive charge state. For reactive landing, the energy of traveling ions can be further increased (if it is not high enough already), by applying a field of reversed polarity (e.g. negative bias at the sample for positive charge states). The kinetic energy of the ions is measured with a retarding grid detector placed before the sample.

5.1.4 Vacuum suitcase

After the deposition, the sample with the desired adsorbates can be transferred to the STM/nc-AFM. In order to transfer it without breaking the UHV and thus contaminating the surface, a vacuum suitcase is used, manufactured by *Ferrovac* (Fig. 5.3). It consist of a small chamber (**1**) equipped with a hand UHV valve (**2**) and is pumped by a lightweight *NexTorr* ion pump (**3**, in red), reaching pressure in the low 10^{-10} mbar regime. The sample is held in the chamber at the end of a horizontal manipulator (**4**). In addition, a copper cooling shield is present, which can be cooled from the top with liquid nitrogen (**5**). It prevents radiative heating of the sample and allows for transport at temperatures around 100 K. As the depositions described in this chapter were carried out on a sample kept at room temperature, it did not require cooling of the suitcase (for details of the cold-transfer process, see Chapter 6, Section 6.5).

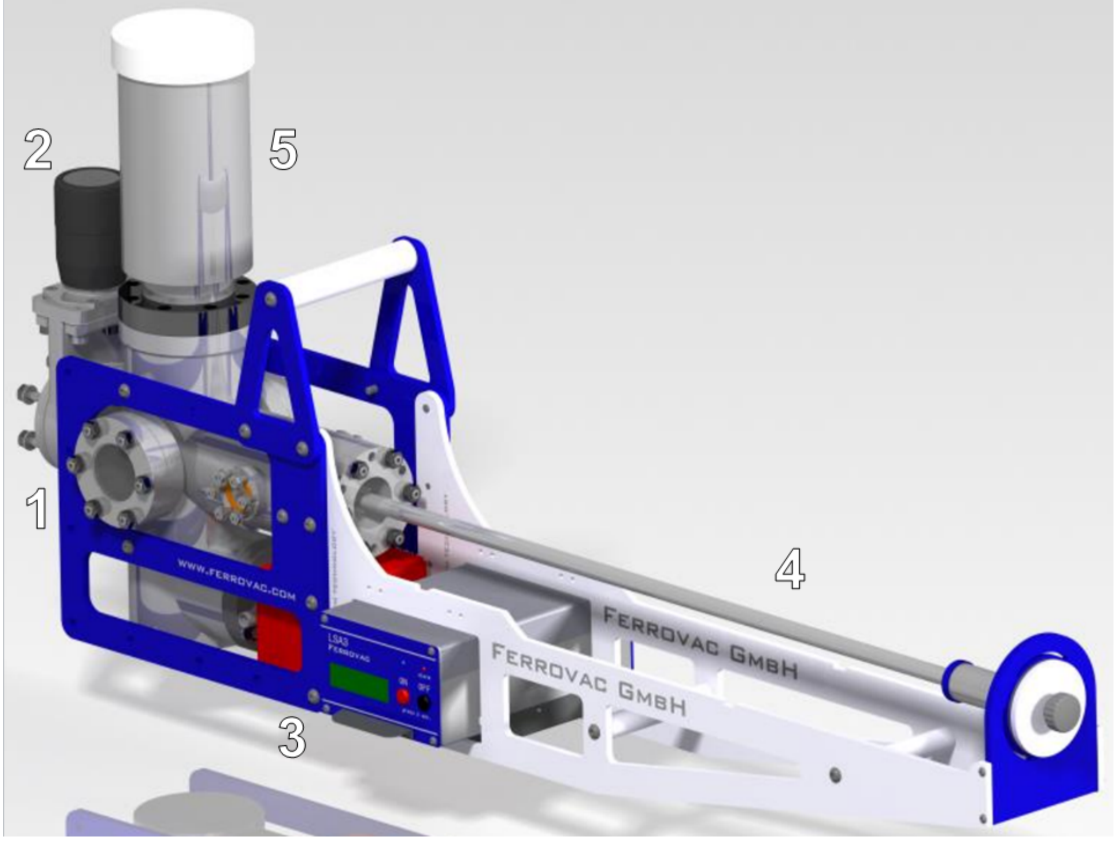

Figure 5.3 3D image of a vacuum suitcase, provided by *Ferrovac*. **1** - suitcase chamber; **2** - UHV hand valve; **3** *Nextorr* ion pump; **4** - horizontal manipulator; **5** liquid nitrogen crostat.

The transfer procedure starts with attaching a closed and pumped suitcase to a load-lock chamber. The load-lock is then pumped. Upon reaching the HV or UHV conditions, the valve separating load-lock from the ES-IBD preparation chamber is opened, followed by opening the valve between the suitcase and the load-lock **2**. The sample is picked up from the ES-IBD manipulator with the suitcase manipulator **4**, which is then retracted back into the suitcase chamber. Both valves are then closed, the load-lock chamber is again vented and the suitcase can be transported to the STM/nc-AFM. There, the whole process is reversed and the sample is moved from the suitcase into the STM/nc-AFM preparation chamber.

5.2 Reichardt's Dye - model system and sample preparation

As a model system for the investigation of the effects of hyperthermal deposition, we use Reichardt's Dye (RD) molecule (Fig. 5.4). Its structure is composed of phenyl rings, with an exception of the central pyridine ring. Moreover, one of the phenyl rings is functionalized with an O atom. Already in the gas phase, RD has an intrinsic electric dipole (± 0.2 e^- at the N and O atoms), while the molecule as a whole stays neutral. This dipole is of potential interest for the reactive landing, as it may influence the surface-molecule interaction, including the reactivity. The simulated conformation of RD (*Avogadro* software, Fig. 5.4 b), c) and d)) reveals that the molecule is not planar in the gas phase and is twisted at the middle C-N bond. This suggests partly planar adsorption of the molecule on metal surface with part of the structure tilted out of the plane. Each of the functional groups of RD is labeled (Fig. 5.4 a)) and they will be referred by the respective labels.

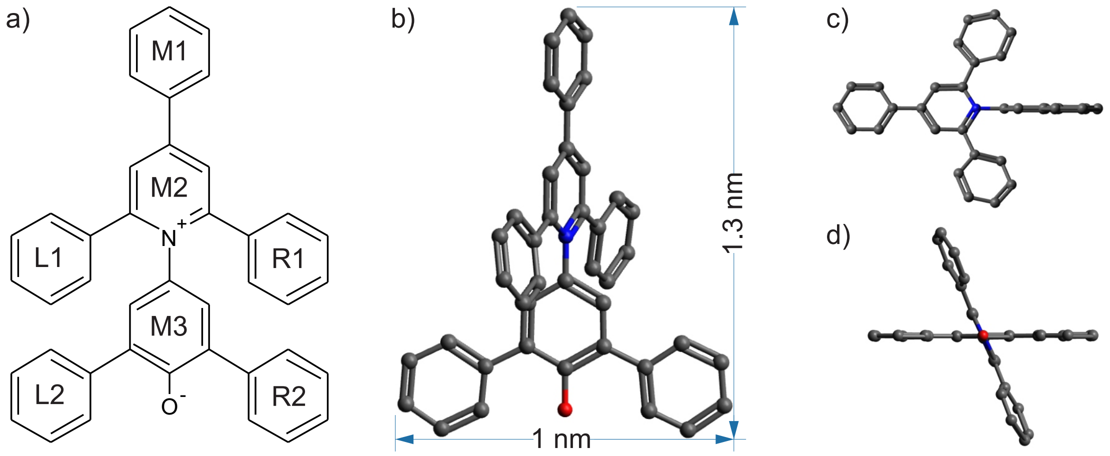

Figure 5.4 a) Chemical structure of Reichardt's Dye. Local charges are present at N and O atoms already in the gas phase, giving a rise to an intrinsic dipole. Each parts of the structure will be further referenced as indicated at the graph, i.e. three middle moieties as M1, M2, M3, two on the left as L1, L2 and two on the right as R1, R2. **b)**, **c)** and **d)** Gas phase conformation, top view, side view, back view.

The RD molecules are deposited by ES-IBD from a 0.1 mM solution, with a 3:1 mixture of ethanol and H_2O used as the solvent, onto the Cu(100) surface (with predeposited NaCl islands) in a positive +1 ion mode. A proton is attached to the O atom of the RD molecule, leading to an effective positive charge at the N atom. This state of RD during the ES-IBD is confirmed with TOF mass spectrometry. The composition of the beam is controlled with the mass filtering quadrupole, ensuring high cleanliness. The deposition is carried out at 10^{-10} mbar. For the soft landing, the kinetic energy of the RD beam is tuned to not exceed 5 eV upon the collision. The hyperthermal landing is carried out in an almost identical manner, without applying the U_{ret} retarding voltage, which is responsible for lowering the kinetic energy of the ions, and the molecules collide with the Cu(100) surface with the kinetic energy of ~30 eV per ion.

For both soft and reactive landing of the RD molecules on the Cu(100) surface, the sample is transferred to the 4 K STM/nc-AFM in the vacuum suitcase. During the transfer, the sample spends ~2 hours in 10^{-10} mbar and, when it is moved through the load-lock, ~1 min in 10^{-8} mbar. In the preparation chamber of the 4 K STM/nc-AFM, it is briefly warmed up to 50 ^{o}C, in order to desorb the possible contaminants, adsorbed during the procedure. After that warm up, the sample is inserted into STM in the cryostat.

5.3 Soft landing of RD

The overview image of the sample after the soft landing is depicted in Fig. 5.5 a). The coverage is approximately 10 % and the majority of the RD molecules have the same topographic appearance (Fig. 5.5 b)). They are symmetric with respect to the long axis of the molecule, with one, central feature (**1**), two protrusions at the opposite end of the molecule (**3**) and two middle features of highest intensity (**2**). The topographic heights (Fig. 5.5 c)) indicate that feature **1** corresponds to **M1** adsorbed in flat manner and features **3** to **L2** and **R2**, also adsorbed in planar geometry. Following these assumptions, the protrusions **2** correspond to **L1** and **R1** tilted upwards. The inability to adsorb in an entirely flat geometry was already indicated by the conformation of the molecule in the gas phase. The most favorable adsorption geometry of the intact RD molecule on the Cu(100) has been calculated theoretically in collaboration with Andrea Floris, Martina Stella and Allesandro De Vita (Fig. 5.6).

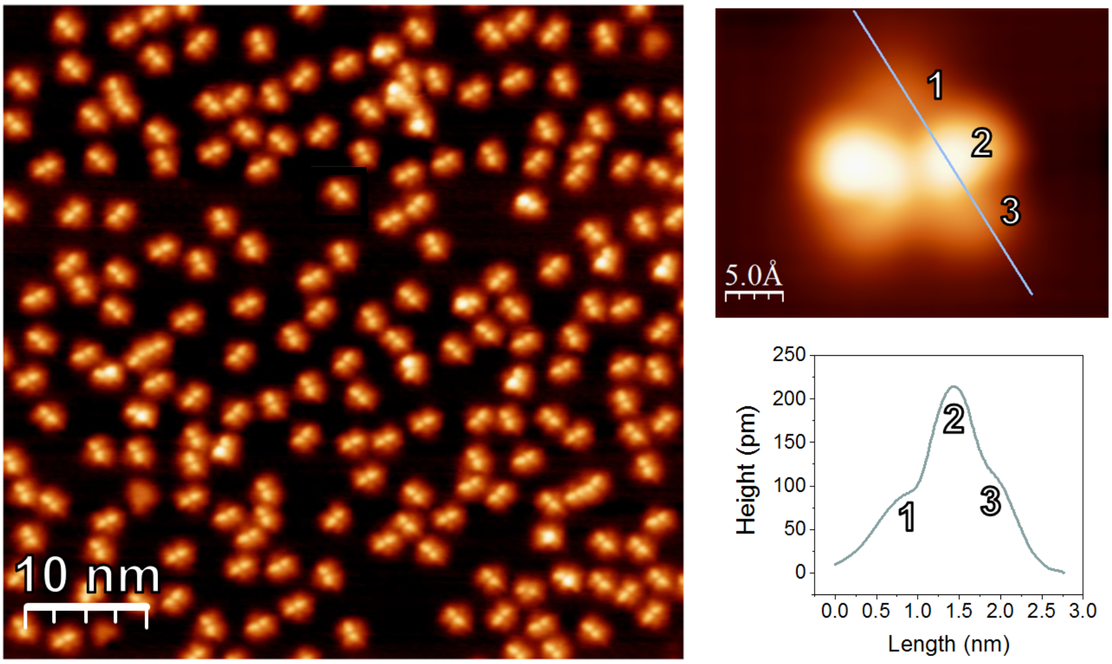

Figure 5.5 Intact RD molecules on Cu(100)C. **a)** Overview image. **b)** Single molecule with three types of distinct features. STM parameters: constant current mode, 10 pA, 1 V, metal tip. **c)** Line profile corresponding to line in b).

According to the calculations, the **L1** and **R1** phenyl rings are twisted out of the plane of the backbone and are not parallel to the surface, as seen as the bright feature **2** in the STM topography. The other aromatic groups adsorb parallel to the surface, which is in the agreement with the interpretation of the topographic appearance. Moreover, the calculations indicate that the RD molecules are coordinated to Cu(100) by the O atom. A similar mechanism has been already observed for a molecule with similar motifs [255].

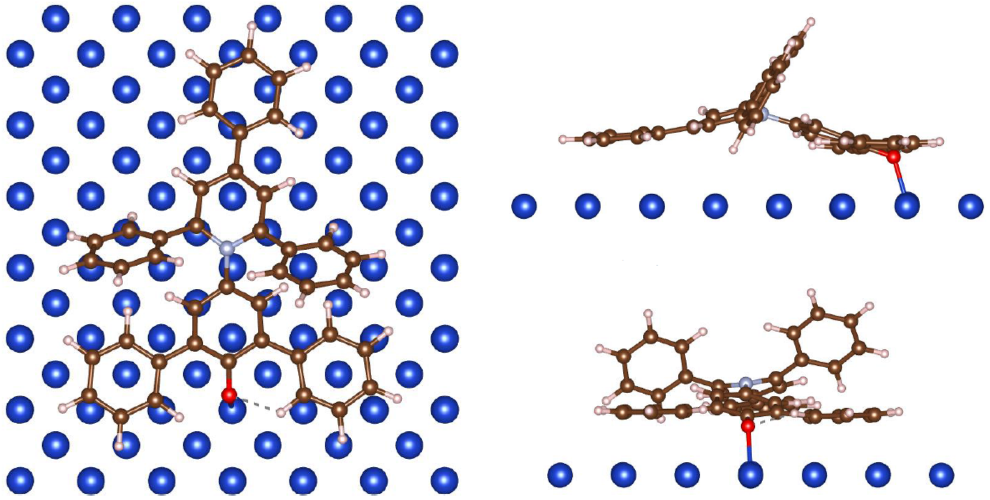

Figure 5.6 Optmized geometry of the RD molecule on Cu(100).

As an additional confirmation, we performed nc-AFM Pauli repulsion imaging. The result is presented in Fig. 5.7. The image corresponds to the top part of the topography shown in Fig. 5.6 a). As the molecule is not planar in its adsorption geometry, the nc-AFM frequency shift image was recorded with the STM current feedback enabled. In this mode, the tip follows the contour of a constant density of states, while simultaneously recording the frequency shift. The image confirms that feature **1** is corresponding to planar **M1**. Upon reaching feature **2**, CO at the tip apex is destabilized, leading to a tip change which disrupts the image. This occurs due to the interaction with a part of the molecule which is not fulfilling the stability requirement of the Pauli repulsion imaging (see Section 3.4). This part is flexible and therefore capable of strong, dynamic interaction with the CO molecule adsorbed at the tip apex. As a result, an artifact in the image was produced (**2** in Fig. 5.7). The CO molecule was knocked off from the tip apex and the image acquisition was stopped. This observation is also in agreement with the interpretation of high intensity features **2** as upstanding phenyl rings, not stabilized by direct interaction with the underlying Cu(100) surface.

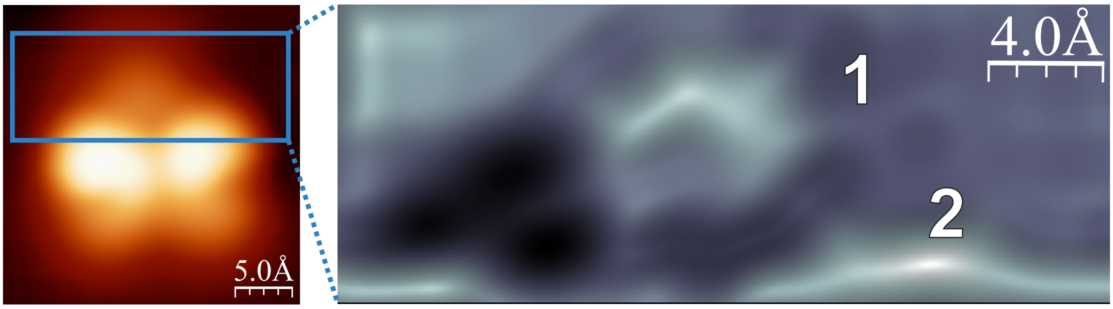

Figure 5.7 Constant current Pauli repulsion image of intact RD molecule on Cu(100). Planar phenyl ring is imaged (**1**, after which the CO molecule at the tip apex get destabilized by interaction with upstanding phenyl rings, which leads to artifact **2**).

In summary, we can assume that the conformation of an intact RD molecule is mostly planar, with the phenyl rings **L1** and **R1** tilted upwards. We denote this species as α.

5.4 Reactions induced thermally

In the next step, we thermally induce the reaction of soft landed RD and investigate the obtained structures. The Cu(100) sample with the intact molecules is annealed at ~100 ^{o}C for 10 minutes. As a result, two new molecular species are observed (Fig. 5.8) together with a significant decrease in the presence of the intact RD, indicating a chemical reaction of the RD molecules. As both of the new species appear smaller and have a lower topographic height, we can assume decomposition of the original structure.

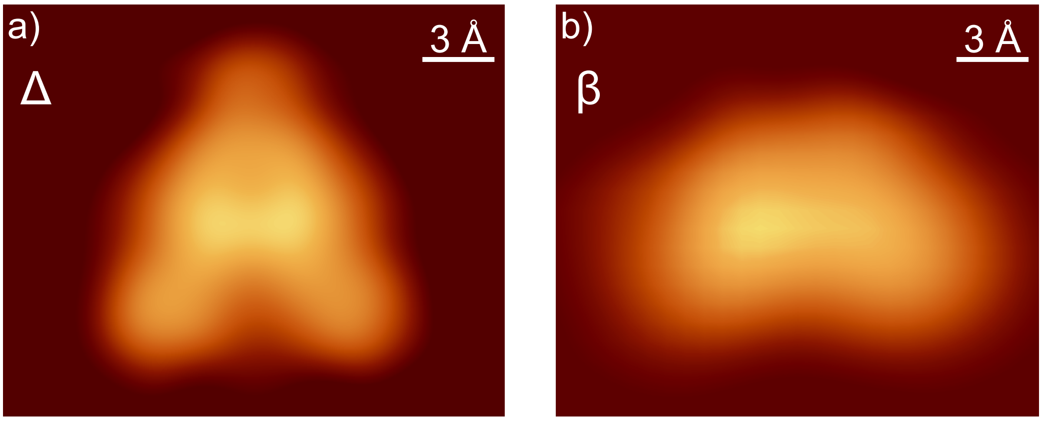

Figure 5.8 Products of thermally induced reaction. **a)** Δ triangular structure with maximum apparent height of ~100 pm, the shape indicates that it corresponds to relaxed upper fragment of the α species. **b)** β structure, with maximum apparent height of ~100 pm. The notch at the bottom part of the image may correspond to similar notch in the lower fragment of the α species. STM parameters of both images: constant current mode, 10 pA, 1 V, metal tip.

The species Δ (Fig. 5.8 a)) has a triangular appearance with a height of ~100 pm and is symmetric, similarly to the α species. A small depression is noticeable at the lower part of the structure. On the basis of its topographic appearance, one can assume that it corresponds to the upper fragment of RD. This assumption has been confirmed by the constant height Pauli repulsion imaging (Fig. 5.9).

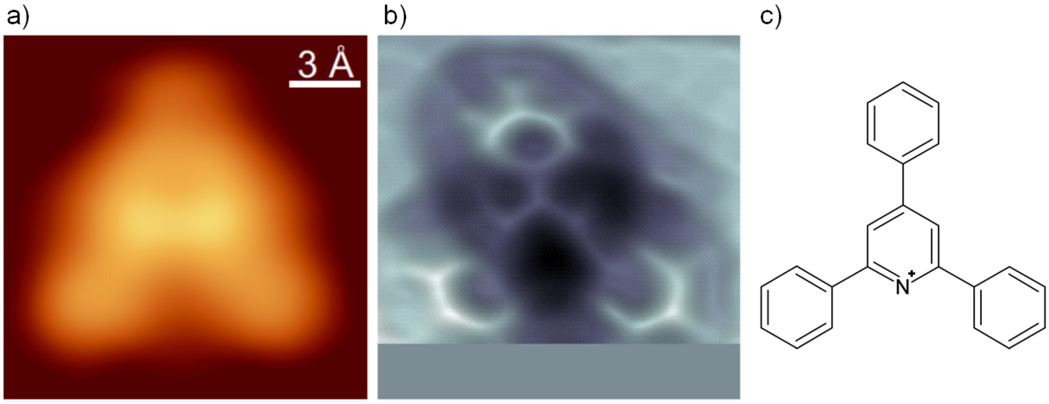

Figure 5.9 Pauli repulsion imaging of the Δ species. **a)** STM topography. **b)** Constant height frequency shift image. Three outer phenyl rings are resolved, with partly visible middle, N-modified ring. **c)** The assumed chemical structure, with the N atom coordinating the molecule to the Cu(100) surface.

In the constant height frequency shift image (Fig. 5.9 b)), three phenyl rings (**M1**, **L1**, **R1**) are clearly resolved. Moreover, a part of the **M2** pyridine is also distinguishable. At the supposed position of the N atom of the **M2** pyridine, a depression is observed. It may appear due to the coordination of the N atom, now with one open bond, to Cu(100). The N atom might be pulled towards the surface by chemisorption or strong physisorption, and thus, during constant height Pauli repulsion imaging, it may be farther from the tip. At higher distances between the object and the tip, a less repulsive potential is detected, explaining the inability to resolve the part of **M2** that is closer to the surface (see Section 3.4 Chapter 3). This is additionally confirmed by the contrast of the frequency shift at **L1** and **R1**, which are clearly pointing upwards at the outer side and downwards at the sides where the bonds to **M2** are present. Hence, Δ is identified as an upper fragment of α split at the C-N bond between **M2** and **M3**.

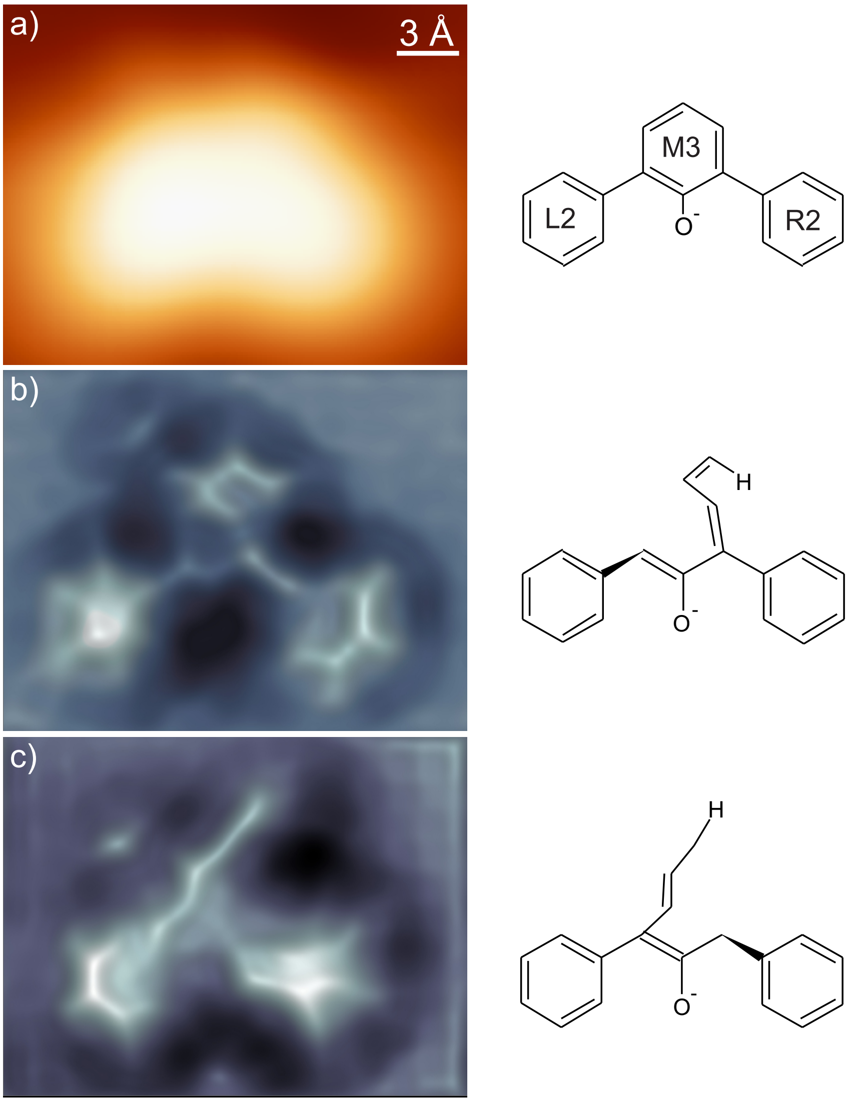

Figure 5.10 Pauli repulsion imaging of the β species. **a)** STM topography, with corresponding part of the RD molecule. **b)** Constant height frequency shift image 1. Two phenyl rings are resolved, of which one is distorted. The **M3** group is ruptured into a semi-free carbon chain. On the right an interpretation of the structure is presented. **c)** Constant height frequency shift image 2, representing different adsorption of the ruptured phenyl group.

A better understanding of the structure of the β species was also obtained with the help of the Pauli repulsion imaging technique (Fig. 5.10). The frequency shift images (Fig. 5.10 b) and c)) revealed that β part is related with the bottom part of the intact RD molecule, although the structure is altered by the fragmentation reaction. Two intact phenyl groups, **L2** and **R2**, are resolved, one slightly distorted (**L2** in b), **R2** in c)). The new conformation of this moiety is not easy to interpret, however, we may assume that this change is associated with structural modification of the **M3** phenyl group. It appears that one of the C-C bonds of **M3** is broken, opening the group and leading to a creation of a flexible alkyl chain, i.e. an "unfolded" **M3** ring. A semi-free alkyl chain should have more than one possible adsorption geometry on the surface. This can be confirmed by resolving more than one conformation of the broken phenyl ring, each with the same topographic appearance in the images obtained with the STM scanning mode (Fig. 5.10 a)). The interpretations of the obtained frequency shift images are presented next to them in Fig. 5.10 b) (semi-folded alkyl chain) and c) (straighten alkyl chain). A detailed understanding of the chemical structure of β would require additional theoretical support, in particular, if we wish to reveal the mechanism of the rupture of **M3** and account for all possible isomers. Despite this, the analysis of the frequency shift images confirms that β originates from the bottom fragment of α with an open **M3** phenyl ring.

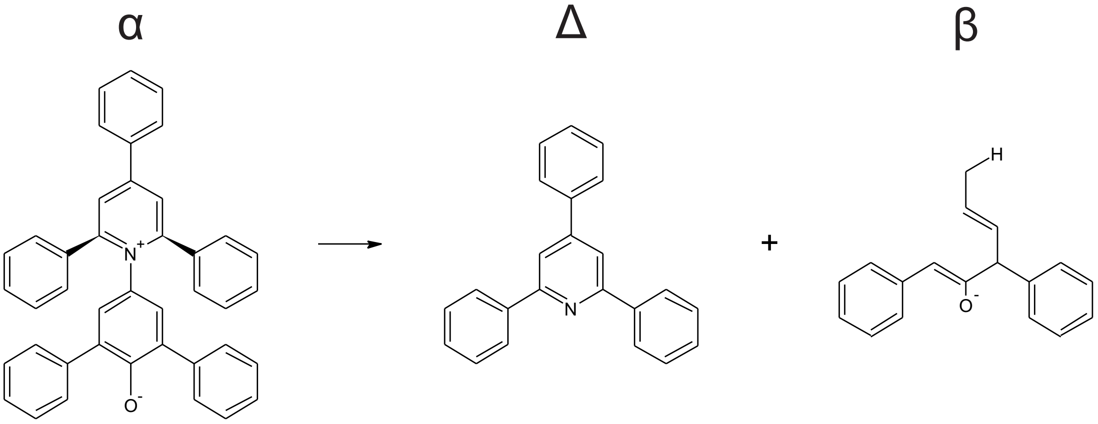

Figure 5.11 Products Δ and β of the thermal decomposition of α.

With all products of the thermally induced reaction identified, we can summarize the process (Fig. 5.11). The C-N bond between **M2** and **M3** breaks, which results in two fragments - Δ and β. This may occur due to the fact that the C-N bond outside of phenyl group is one of the weakest in the RD structure (where breaking one of the 5 outer, unmodified phenyl groups would require higher thermal energies or presence of the highly catalytic factors) [256]–[258]. What is not yet understood is the effect of the local charging of the N atom on the stability of the bond. We can speculate that the interaction of the charged atom with the underlying surface is stronger, leading to elongation of surrounding bonds, among them the C-N bond, and lowering the energy barrier for the dissociation. Another, purely speculative possibility, is that a local charge in close vicinity to the C-N bond influences the distribution of the electrons participating in the bond, also lowering the energy barrier for bond breaking. Nevertheless, it is reasonable to assume, that even without the possible catalytic effect of this charging, the aforementioned C-N bond would still be dissociated before the rupture of the phenyl and pyridine rings.

After the reaction, the two phenyl groups **L1** and **R1** of α, now part of Δ, are no longer spherically hindered and change their adsorption geometry to planar. After that, we are able to resolve them with the Pauli repulsion imaging technique, in contrast to the experiments of the intact molecule (Fig. 5.7).

The **M3** phenyl ring of the β fragment underwent additional structural changes, attributed to the rupture of the ring at one of the *ortho* C atoms, with respect to the bottommost C atom. As a result, the broken phenyl group becomes an alkyl chain with additional degrees of freedom, allowing for a range of adsorption geometries, of which, two examples are given in Fig. 5.10. We can speculate that the dissociation of one of the inner bonds of this particular phenyl ring is possible due to the disruption of the electron delocalization resonance by the attached functional groups [128].

5.5 Reactions induced by hyperthermal collisions

After the hyperthermal collision of the RD molecules with Cu(100), four species are present: intact α (all of which would have been decomposed after sufficiently long thermal annealing), fragments Δ and β, as well as a new species, which, because of its resemblance to the intact molecule, was labeled as α' (Fig. 5.12).

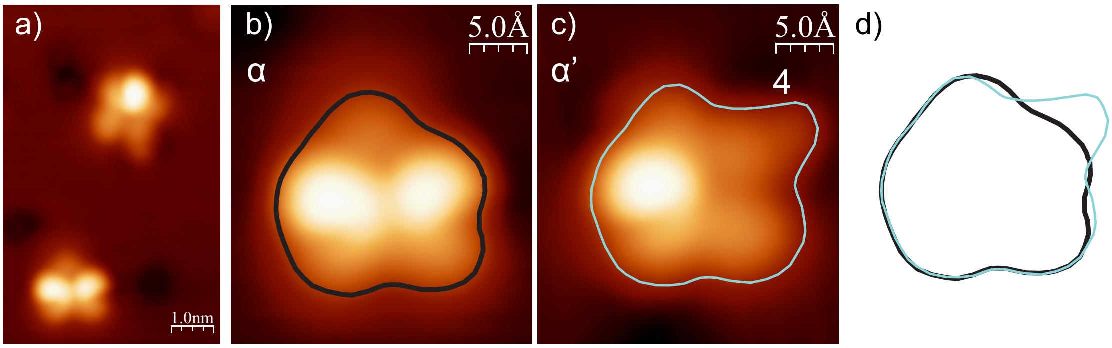

Figure 5.12 New species of the RD acquired through the hyperthermal landing. **a** The intact species α and new species α'. STM image parameters: constant current, metal tip, 10 pA, 1 V. **b)** α with the shape contour. **c)** α' with the shape contour. **d)** Overlap of the shape contours indicating the topographic differences.

Comparison between constant current topographies of α and α' conformations of RD (acquired within the same image, Fig. 5.12 a)), revealed that the majority of the structure of α is not affected. The appearance of α' follows both the topographic height and the shape of α. The only difference is the disappearance of one of the tilted phenyl rings (**L1**/**R2**). The corresponding feature in α', marked **4**, exhibits a topographic height of ~100 pm (in the range of planar phenyl rings) and a shape which is extending over the contour of the α species (Fig. 5.12 d)). This is a strong indication that a structural or conformational change has occurred at one of the tilted phenyl rings without alteration of the rest of the structure. The Pauli repulsion imaging revealed that the modified part of the structure is not entirely stable on the surface and vibrates in the *XY* plane when a repulsive force is applied. This renders it impossible to resolve with nc-AFM high-resolution techniques. The constant current imaging performed after the unsuccessful try of the Pauli repulsion imaging revealed that the topographic appearance of **4** has changed (Fig. 5.13 b)). It became more parallel to the rest of the structure, while previously it was sticking out in a perpendicular conformation. The comparison of the contour of these conformations indicates that the change concerns only the modified phenyl ring (Fig. 5.13 c)). Moreover, both versions of α' are observable on the surface directly after reactive landing.

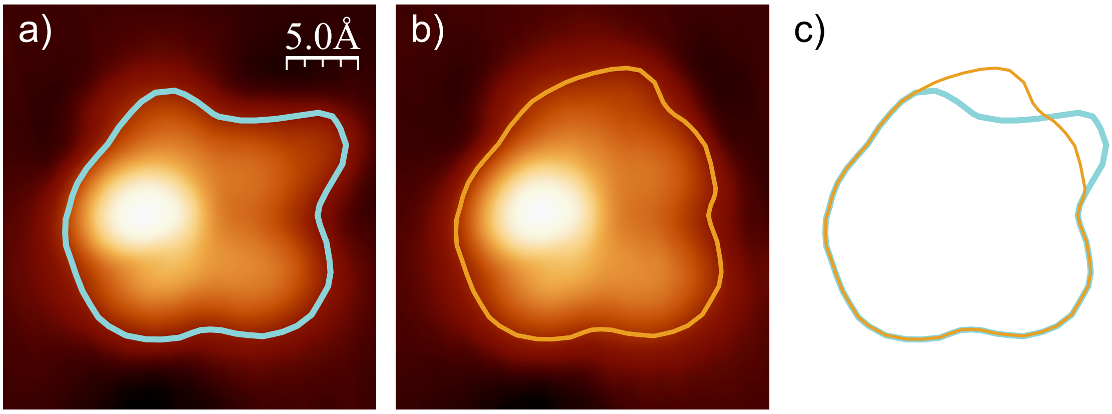

Figure 5.13 Tip induced modification of the α' conformation. The conformation depicted in the image a) was modified into the conformation depicted in the image b) during the nc-AFM measurements, due to the close proximity of the tip to the adsorbate. STM image parameters: 10 pA, 1 V. **c)** Comparison of the contours indicating that the change occurs only at the modified phenyl group.

In order to deduce the difference between the α and α' species, a few facts have to be considered. Overlay of their contours (Fig. 5.12) and interpretation of the topographic appearance of α allows us to assume that feature **4** is associated with **L1** or **R1**. In the intact conformation, they are tilted upwards, as indicated by the simulations and the experiment (Fig. 5.6). Furthermore, no other geometry of unaltered RD has been observed. This suggests, that **4** in α' appears due to the structural modification of a certain part of α rather than a purely conformational change, although the latter option cannot be decisively excluded. By its topographic height it resembles the **M1**, **L2** and **R2** phenyl rings adsorbed in a planar manner. Moreover, **4** is semi-flexible in the *XY* plane and it can be switched between two different geometries, leading to two conformations of α' (Fig. 5.13). This allows us to speculate that part of the structure corresponding to **4** has no stable adsorption sites in close vicinity. If **L1** or **R1** were broken into a semi-free alkyl chain, it would be more probable for them to achieve a stable adsorption geometry on Cu(100), even in close vicinity to the rest of the molecule. Therefore, it would be possible to image the structure of **4** with the Pauli repulsion imaging, like in the case of modified **M3** in the β species. Therefore, we propose a structure, which involves breaking one of the inner C-N bonds of the **M2** pyridine group (Fig. 5.14). This structural change would possibly render one of the upstanding phenyl rings able to change its adsorption geometry, yet without providing full on-surface stability as in the case of opening this specific group into an alkyl chain. Molecular dynamics simulations of a collision process of an RD ion with the kinetic energy of 30 eV, done in collaboration with Kelvin Anggara, indicate that it is indeed possible to break one of the inner bonds of the pyridine group **M2** without damaging any other part of the RD molecule. Although this interpretation of the α' structure contains uncertainties (e.g. charge state of the N atom after the potential rupture, the interaction of atoms with now open bonds with the surface), it embodies significant differences between α' and previously observed species.

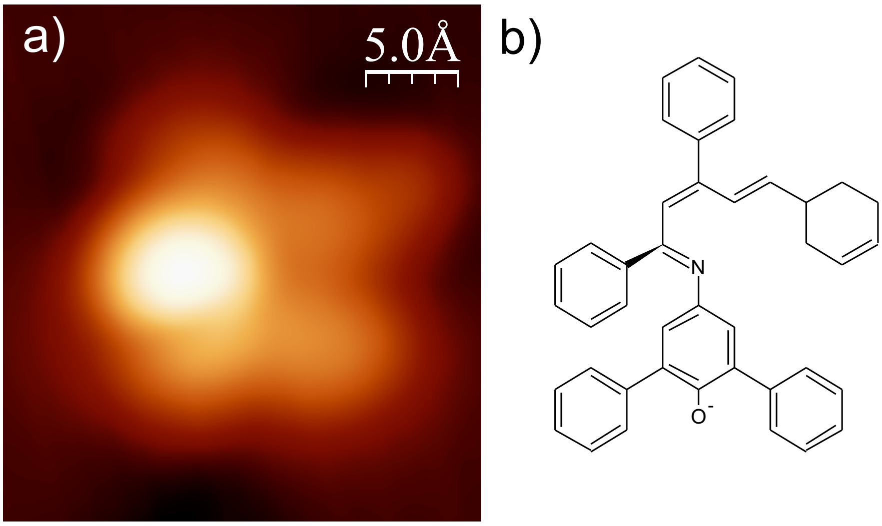

Figure 5.14 Proposed structure of the α' species. a) STM image of α'. **b)** Proposed chemical structure.

5.6 Conclusions

In this chapter, we presented a proof-of-concept study of chemical reactions realized by the hyperthermal collision. Utilizing ES-IBD we deposited the Reichardt's Dye molecules, first via soft landing. As the STM/nc-AFM studies revealed, thermally activated reactions of the soft landed molecules involve scission of the middle C-N bond (Fig. 5.15) and splitting of the intact molecule into two fragments, α and β. In the next step, a reactive landing was performed, where the molecules of the same type collide with the Cu(100) at 30 eV kinetic energy. The two aforementioned fragments were also created with hyperthermal reactions, as well as a new species α', not obtainable through thermal activation. We concluded the structure as the modified RD molecule, which has one of the inner C-N bonds broken at the middle pyridine group. Dissociation of this bond results in the change of the geometry of one of the non-planar (in the intact molecules on the surface) phenyl rings.

The STM/nc-AFM investigation of the on-surface reaction products, assisted by the DFT and molecular dynamics simulations, allowed identification of the differences between the obtained species. Still, some of the questions are open, and certain details of the structures have yet to be resolved (like charge states of the N and O atoms on the surface, the interaction of the atoms with open bonds to the surface and geometries of the adsorption). Further investigation, as well as theoretical analysis and simulations, are necessary to elucidate the structure and geometry of the reacted species. Nevertheless, the STM/nc-AFM analysis proves that the reactive landing opens the novel, non-equilibrium reaction pathways (Fig. 5.15). Therefore, as we control the collision energy in the ES-IBD process, we can influence surface-adsorbate interaction and chemistry. The STM/nc-AFM technique has proven to be a powerful tool to investigate the products of the reactive landing, providing unique insight into the molecular structure.

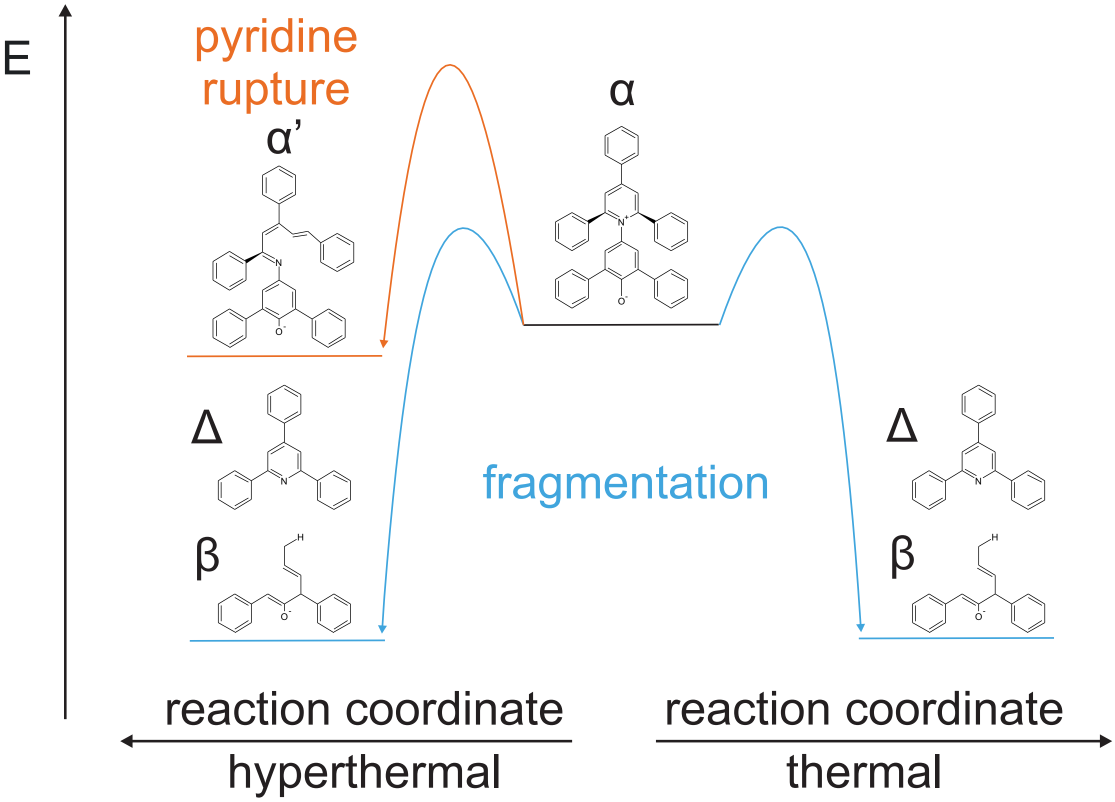

Figure 5.15 Schematic energy diagram representing the differences between thermal and hyperthermal activation of the Reichardt's Dye molecules. Annealing of the sample results in the fragmentation of the structure. The hyperthermal landing, except inducing the same fragmentation on part of the molecules, additionally allows crossing higher energy barriers and following different chemical reactions. This occurs due to the local and temporal dispersion of the kinetic energy into the thermal/vibrational form. As a result, new structures are observed, unobtainable by means of thermally activated reactions.

6 Carbohydrates on metal surfaces

The possibility of precise and controlled deposition of chargeable and soluble molecules provided by ES-IBD drastically improves the applications of SPM techniques. The on-surface studies of biologically relevant species and systems were previously limited by sample preparation. The majority of biomolecules are not volatile and, as mentioned in the previous chapter, drop casting/spin coating does not yield a sample quality that enables investigation with nanoscale precision. Nowadays, precise STM studies of larger biomolecules are conducted on samples prepared with ES-IBD, including the investigation of amino acids [156], [259], peptides [250], [259]–[261] and proteins [156], [250], [262]. Thanks to this possibility, the STM/nc-AFM studies may contribute to the field of molecular biology and its subcategories: genomics, proteomics and glycomics.

Glycomics is a subset of molecular biology, which aims at the identification, understanding and quantification of the carbohydrates that play a role in living organisms both in pure and conjugated forms, i.e. the glycome, named analogously to the genome [20], [263]. Apart from the basic role of an energy source (glucose), glycans take part in a vast number of biological processes, including the majority of cell's surface interaction, like the immune response, transfers via membranes and blood type determination [20], [264]–[266] (Fig. 6.1). In contrast to the genome and the proteome, the glycome is not as well understood. One reason is that it is not hardcoded in the DNA, meaning that the structure of synthesized carbohydrates depends not only on synthesizing genes and proteins but also on the microenvironment (e.g. temperature, pH) during the process [264].

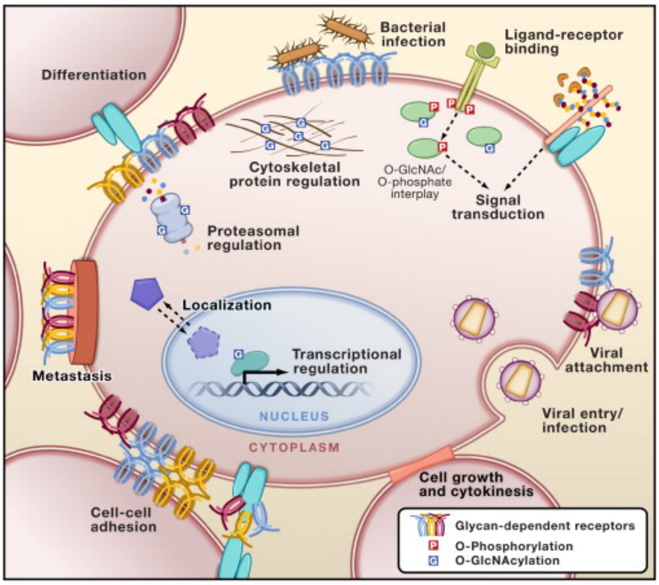

Figure 6.1 Roles of glycans and glycoconjugates in the cell's interface proccesses (from Hart and Copeland [20]).

Moreover, the glycans are often covalently bond to other biomolecules, like lipids and proteins, which modify their functionality. At least 50 % of all polypeptides are modified by glycans [267], which means that glycomics also aims to understand the interaction of carbohydrates with other molecules. This drastically widens and complicates the scope of the field (e.g. at least 41 types of linkages between carbohydrates and proteins exist) [268]. Lastly, the complexity of the inner structure of carbohydrates greatly exceeds amino acids. While single amino acids always bind together in a linear manner (peptides), carbohydrates can form branched sequences. Each monosaccharide contains up to 5 hydroxyl groups, which can be used to form a glycosidic bond to other monosaccharide units [21]. These factors, combined with a lack of advanced analysis techniques, are reasons behind the underdevelopment of the glycomics in comparison to the fields of genomics and proteomics [20]. The analysis of the inner structure of glycans still poses a significant challenge. Single features can be identified by spectroscopic methods, but full identification is harder to achieve. It may be possible to address the issue of branching by real space imaging techniques that directly access the structures of the investigated systems. The identification of the branching geometry of the oligosaccharide with a less material demanding method might reduce the overall time and material cost requirements. Taking into account the current varieties of sample preparation by ES-IBD and analysis with combined STM/nc-AFM, we decided to explore real-space imaging of glycans.

In this chapter, we explore combined STM/nc-AFM as a technique to resolve the structure of model oligosaccharides, consisting of five and six mannose units (man5mer and man6mer). The main experimental goal is to identify, in real space, the differences between linear and branched mannose polymers, i.e. to identify the branching points. The carbohydrate molecules were deposited on metal surfaces with the ES-IBD technique. We observed repeatable features in clusters of linear man5mers on Cu(100) and obtained more distributed, less clustered structures, with low-temperature ES-IBD on Cu(111). We assume, that the most often observed features correspond to double mannose entities. On the base of this assumption, we can identify the structures of less clustered molecules. Moreover, the first experiments with the branched man6mer yielded promising results. The observations and analysis of both linear man5mer and branched man6mer molecules on metal surfaces encourage further experiments, utilizing the STM and nc-AFM structural analysis to a full extent. Following these results, the ES-IBD, together with combined STM/nc-AFM techniques, starts to appear as a complementary tool in molecular biology.

6.1 Structural complexity of glycans

Similarly to proteins and genes, glycans are compounds consisting of smaller building blocks called monosaccharides [269]. The basic example of such a building block is D-glucose (L-carbohydrates will not be considered in this chapter, as the majority of carbohydrates occurring in nature are d-enantiomers). Its chemical structure in the biologically relevant pyranose cyclic form is depicted in Fig. 6.2. Two anomers of each carbohydrate exist, alpha and beta, different by the relative position of the -OH group at the first C atom position, marked with an orange loop (Fig.6.2).

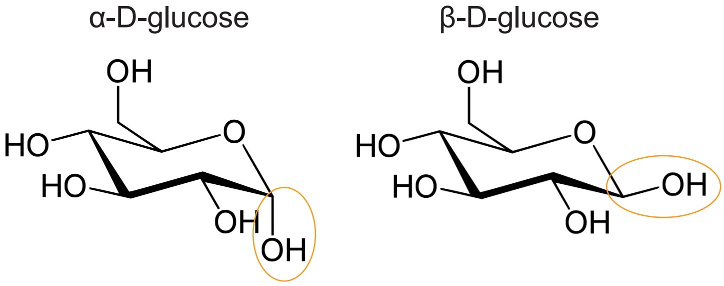

Figure 6.2 Chair representation of the α and β D-glucose molecule anomers. The difference between structures is marked with an orange loop.

Monosaccharides can form oligo- and polysaccharides through condensation and formation of glycosidic bonds (Fig. 6.3). Any of the hydroxyl groups can be used to form the bond with another monosaccharide, leading to theoretically 25 possible glycosidic bonds between two basic building blocks of a glycan. Each of them has a stereocenter, which influences the molecular properties [270]. Another level of complexity can be added when more than one hydroxyl group of a single monosaccharide form a glycosidic bond. This leads to the possibility of creating branched structures (Fig. 6.4).

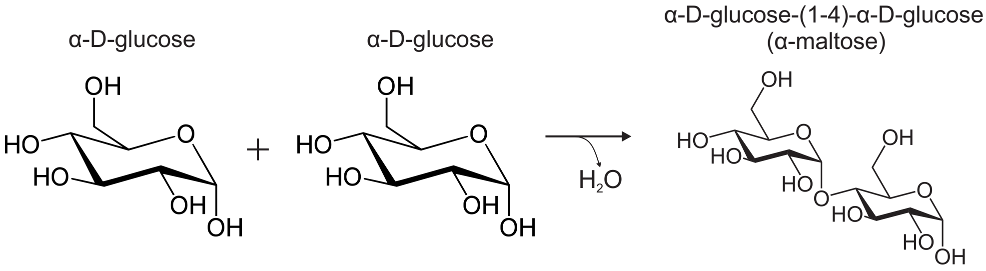

Figure 6.3 Glycosidation reaction of two α-D-glucose molecules. The geometry of the bond depends on the geometry of the -OH groups forming the bond.

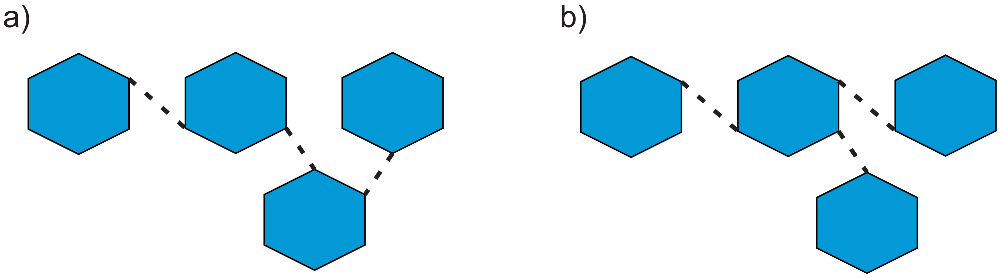

Figure 6.4 Branching of polysaccharides. **a)** Polysaccharide consisting of 4 monosaccharides connected in linear manner. **b)** Polysaccharide with branching point at the third unit. The molecule has the identical mass and composition as the linear polysaccharide from a).

The branching phenomenon extends the spectrum of possible carbohydrate structures and also renders the analysis of them significantly harder than the analysis of peptide-based molecules (in which amino acids are always connecting in a linear manner [271]). Majority of the monosaccharides are isomers (e.g. glucose, galactose, mannose, altrose, allose, talose), therefore, glycans performing vastly different functions may have identical mass and sum formula. Therefore, the identification of all of the structural features becomes more difficult with both the number of branching points and the size of the molecule itself [271].

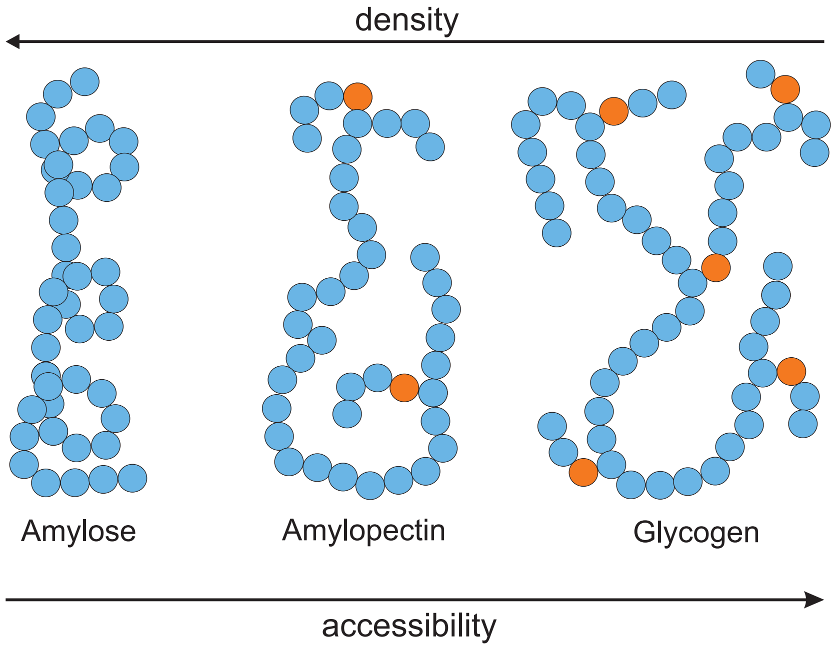

Figure 6.5 Linear (amylose) and branched polymers of glucose (amylopectin and glycogen). Units marked with orange color are linked to the main chain by 1→6 glycosidic bonds.

The polymers of glucose are an example of how the properties and functionalities of glycans, which consist of the same type of building block are influenced by branching (Fig. 6.5). Starch, which functions as energy storage in plants, is a mixture of linear amylose and branched amylopectin [272]. Amylose is a linear glucose polymer, where units are connected with 1→4 glycosidic bonds. Amylopectin is branched through additional 1→6 bonds occurring every 24-30 glucose units [273]. Even more branched form of poly-glucose exists, called glycogen, where 1→6 bonds occur every 8 to 12 glucose units. This polysaccharide functions as energy storage for animals. The more branched the poly-glucose is, the easier it is to degrade into a processable form, as enzymes have more access points. On the other hand, linear amylose has the highest density, allowing for the storage of more energy in a smaller volume. The mixture of amylose and amylopectin is a source of long-term energy, allowing for sustained vegetation. Glycogen is a source of easily accessible energy, although quickly depleting, as it is needed for performing more dynamic life functions of animals. This example shows the influence of branching on the relatively simple system of one type of monosaccharide and two types of glycosidic bonds. In more structurally varied glycans, the influence might be even stronger [264].

Glycans are an extremely diverse group of organic molecules and even the smallest structural differences may lead to altered chemistry and a different function in a living organism. This short section is only a small window into the complexity of polycarbohydrates. Starting from a wide selection of building blocks, through branching and various linkage types, to forming a glycoconjugate, the complexity of glycans results in almost a million unique molecules and conjugates [20]. Despite glycans fulfilling crucial roles in the development of drugs and vaccinations, their structure has not yet been fully understood [21]. This means, that certain analysis techniques, like standard MS, are not sufficient, and novel methods are needed [20], [21], [271], [274], [275], including possible real-space imaging of branched glycans.

6.2 Methods in the structural analysis of glycans

Due to the complexity of glycans, standard analysis methods are often not able to distinguish between the different types of polysaccharides. As an example, MS, measuring the mass-to-charge ratio, would recognize α- and β-maltose (Fig. 6.3) as the same molecular species. Similarly, if one of the glucose molecules would be replaced with galactose, creating a lactose molecule, the mass-to-charge ratio also would be identical. The field of glycomics inherently requires techniques able to distinguish molecular species not only on the base of their composition, but also on the base of the relative geometry of the hydroxyl groups (to identify building blocks), position of glycosidic bonds (to identify which groups are used to form the linkage) and stereochemistry of the bond itself (to asses the final molecular geometry) [271].

Typically, elucidating the complex structures of a glycan is obtained through the combined use of NMR and MS. MS can be used to determine the size of the molecule, i.e. the number of building blocks, while NMR can provide information about connectivity and geometry of glycosidic bonds. The acquisition speed and high-resolution data produced by MS renders it a perfect starting technique. Positions of the glycosidic bonds can be determined not only with NMR but also by using MS coupled with selective chemical modifications of the investigated molecules. Another possibility is to use tandem quadrupole time-of-flight mass spectrometry (Q-TOF-MS) [16], [17], [276], [277]. The information of the bond's stereochemistry (as well as the other details already accessible by various MS techniques) can be acquired via elaborate NMR experiments. The full pathway to complete identification of a structure of a glycoprotein will not be described herein, as it is beyond the scope of this thesis. A basic workflow, presenting the complexity of such a pathway, is depicted in Fig. 6.6. For a better description and understanding of the techniques and concepts presented in this scheme see Mariño *et al.* [19]. One of the inherent characteristics of this procedure, often involving destructive techniques, is the requirement of a high amount of the analyte, typically more than 1 mg [19], [271]. Considering that many of the investigated systems are directly obtained from living organisms, acquisition of this amount might be problematic or even impossible, limiting the applicability of the full structure determination procedure to purely synthetic glycans or glycoconjugates.

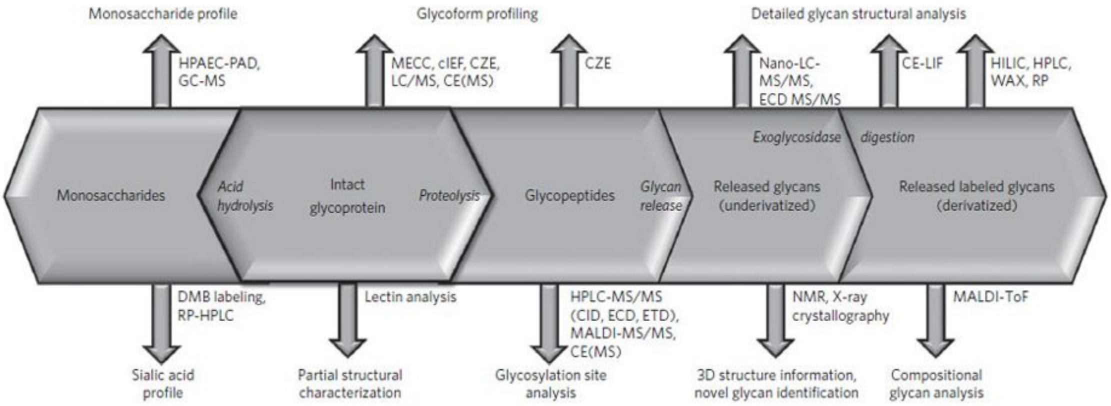

Figure 6.6 Diagram representing steps in procedure of the determination of a full structure of a glyconjugate (Mariño *et al.* [19]).

The issue of the molecule's availability can be circumvented with techniques that are sensitive to all of the structural discrepancies. One of the techniques, allowing such an experiment, is ion-mobility mass spectrometry (IM-MS) [271], [278]–[280]. In this technique, the molecular ions are traveling under the influence of electric fields through a tube filled with a chemically inert gas. The species collide with particles of the inert gas of different frequencies, thus, changing the drift time through the tube. As a result, species of the same mass and composition can be distinguished without resorting to time-consuming and destructive techniques. The drift time can be expressed as a collision cross section (CCS), which is rotationally averaged and independent of the instrument parameters. An example of a structural investigation of glycans using IM-MS is given by Hoffman *et al.* [271]. The method is capable of differentiating between glycans that vary by the position of a single glycosidic bond, as well as between molecules with a single exchanged α/β anomer. On the other hand, it was not proven to be able to distinguish isomers with non-identical monosaccharide composition. Moreover, drift times of molecules with more than one structural difference could be similar, which indicates that the analysis of longer and possibly branched oligosaccharides will pose a significant challenge.

The elucidation of the structure of longer, more branched and overall more complicated glycans, cannot be achieved with a single method. The topic of glycan identification has to be addressed with a set of complementary techniques aimed at certain aspects of the structural complexity. They have to be supported by constantly updated and accessible databases that allow for fast comparison of acquired results [21]. Potentially, the branching aspect can be addressed by a combined STM/nc-AFM approach, assisted by ES-IBD. We explore the possibility to analyze glycans in real space in cooperation with the group of prof. Peter Seeberger from Max Planck Institute of Colloids and Interfaces in Potsdam [281]. Their research is focusing at elucidation of the role of glycans in living organisms, identification of their fine structural details, and synthesis of synthetic carbohydrates. With the help of their expertise, we were able to select a proper carbohydrate model system and deposit chosen molecules onto the metal surfaces via ES-IBD. In Chapter 5 we have proven the capability of resolving the structure of molecules prepared by ES-IBD. Here, we do not try to identify the species in the smallest details, as part of the structural features of oligosaccharides adsorbed on surfaces might be not accessible (e.g. geometry of a glycosidic bond). The main goal is to identify the overall sequence and conformation of the molecule, i.e. number of monosaccharide building blocks and positions of the branching points. In order to do that, we compare two model systems consisting of the same monosaccharide units and differing only by the branching in one of the species.

6.3 Oligomers of mannose as a model system

As a model system to test the capability of STM/nc-AFM as a tool to structurally analyze glycans, we chose oligomers of mannose. The two investigated synthetic structures (man5mer and man6mer) are depicted in Fig. 6.7.

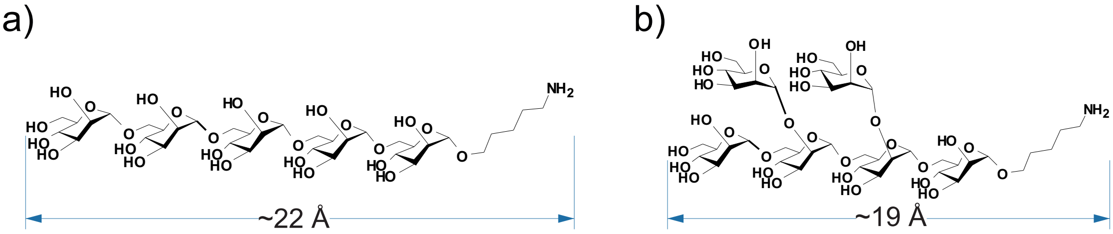

Figure 6.7 Linear man5mer (a) and branched man6mer (b) structure.

The first structure consist of five α-mannose monosaccharide units, connected with 6→1 glycosidic bonds (Fig. 6.7 a)). One end of the molecule has an alkyl chain with a terminal amine, a residue of the synthesis process [271], [282]. The uniform composition should simplify the identification of the basic structural features (as they should appear identical). The second species includes two branching points (Fig. 6.7 b)). Four mannose units are again connected linearly through 6→1 glycosidic bonds, but at the second and the third units, branching points are present in the form of an additional 2→1 glycosidic bond to another α-mannose units. Comparison between two species of the same, uniform composition, allows us to focus on the branching. Analysis of both structures separately may possibly result in the identification of the topographic features corresponding to monosaccharide building blocks and in the localization of the branching points.

6.4 Linear pentamers on Cu(100)

The linear man5mer molecules are soft landed on Cu(100) using the ES-IBD in the negative -1 mode. The Cu(100) surface was chosen to minimize the diffusion of the molecules. Glycans, due to the structural flexibility of both the glycosidic bonds and monosaccharide units, can diffuse on the surface. Due to that, clustering may occur, complicating the analysis. The easiest to analyze are straight, planar and non-clustered structures, like in the case of the TCT and RD molecules presented in Chapters 4 and 5.

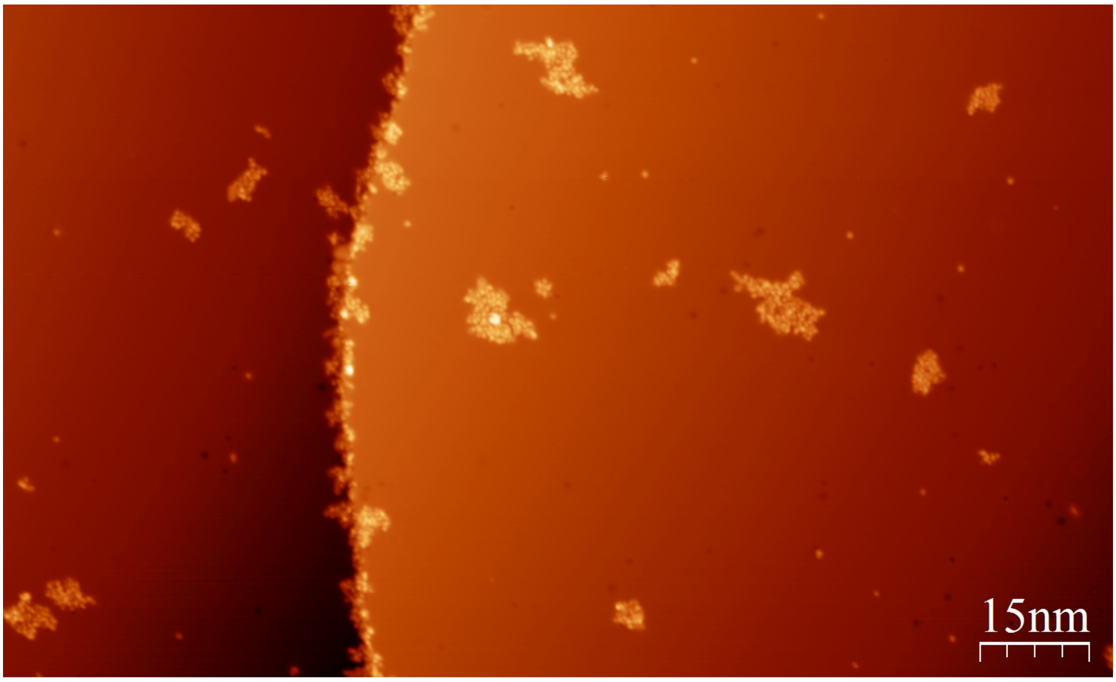

Figure 6.8 Linear man5mer molecules on Cu(100) - overview image. The man5mer molecules are clustered into structures often exceeding 10 nm size. Smaller clusters can be seen attached to both side of an atomic step edge. Image parameters: constant current, 100 pA, 100 mV.

After the deposition, the sample is transferred to STM using a vacuum suitcase, as described in Chapter 5. The overview image (Fig. 6.8) reveals that the structural properties of the man5mer indeed lead to a diffusion process and the man5mer molecules are clustered into irregular structures. Moreover, the diffusion leads to the adsorption of the man5mer onto both low and high side of the atomic step edges. Despite the irregular character of the clusters, organized assemblies are observed among them, of which, examples are given in Fig. 6.9. The assemblies consist of a row of asymmetric protrusions smaller than 1 nm (**A**). Next to it, triangular features are distinguishable (**B**), consisting of two symmetric, dumbbell shape protrusions and one asymmetric. The same pattern, with varied length, is repeated in different clusters, leading to an assumption that the observed protrusions are associated with the building blocks of the man5mer molecule, i.e. mannose units or alkyl chains. The detailed analysis of observed assemblies will be presented in section 6.6. In order to obtain single man5mer molecules, allowing for possible better understanding of its topographical appearance, the clustering effect has to be minimized. One possibility of addressing this issue is to lower the temperature of the sample during the deposition, as lowering the thermal energy should minimize the probability of crossing the energy barriers in the diffusion process.

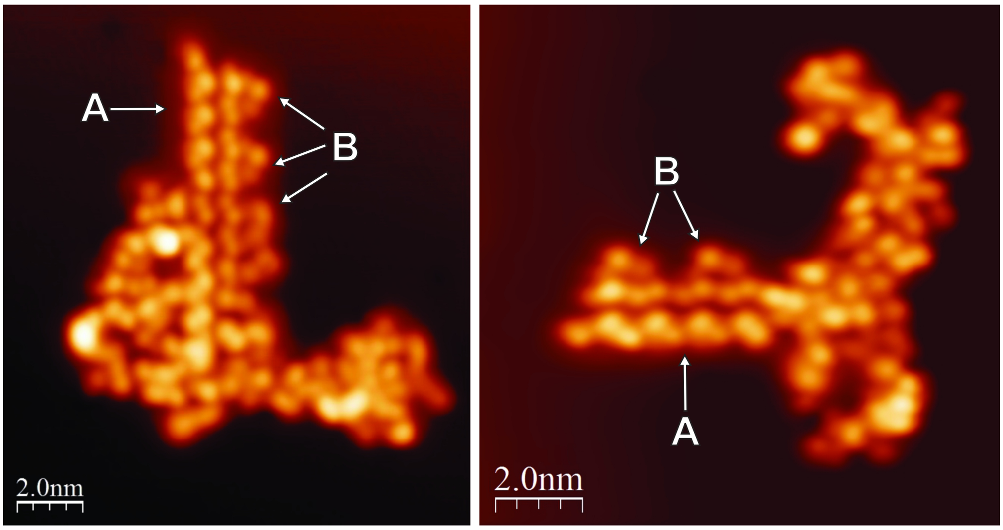

Figure 6.9 Clusters of man5mer on Cu(100) exhibiting semi-organized substructure. Near identical substructures are observable in clusters of different size and characteristic. Image parameters: constant current, 100 pA, 100 mV.

6.5 Linear pentamers on Cu(111)

In order to address the clustering issue, we perform ES-IBD on the Cu(111) surface kept at ~150 K. Using the built-in cooling system of the ES-IBD device manipulator, the sample is cooled down to around 150 K with LN_2. After the deposition, it is transferred to the 4 K STM/nc-AFM with a cryo-vacuum suitcase, which keeps the low temperature (also using LN_2). Accordingly, the manipulator of the 4 K STM/nc-AFM is cooled down with liquid nitrogen, keeping the sample at similar temperatures during the last step of the transfer chain, after which it is put into the cryostat. After the cold deposition/transfer procedure, the sample is covered with a mobile contaminant, forming semi-stable islands, as depicted in Fig. 6.10 a). In this state, the man5mer molecules were not observable. It can be assumed that the contaminant is the remnant of the transfer process, thus, the sample has to be heated sufficiently high to desorb it from the surface. Therefore, it is warmed up to 220 K, as this temperature should result in the desorption of the contaminant, but not yet induce strong diffusion of man5mer. As a result, a surface with smaller, more distributed man5mer clusters is obtained (Fig. 6.10 b)).

Among different clusters, a few have sizes that may correspond to structures composed of one or two man5mer molecules. The species depicted in Fig. 6.11 a), consist of two asymmetric protrusions at the ends of a structure consisting of four smaller, symmetric protrusions. This bears a resemblance to the two entities in triangular feature **B** observed in man5mer clusters after the room-temperature deposition on Cu(100) (Fig. 6.9). Fig. 6.11 b) depicts a smaller species, which is composed of two entities and two terminals, one of higher topographic appearance, one of lower. In contrary to organized assemblies encountered on Cu(100), no long-range structural repetition is observed. This leads to the assumption that non-clustered, possibly single or double man5mer molecules, are observed with more available adsorption geometries. Observed features will be analyzed in detail in the next section.

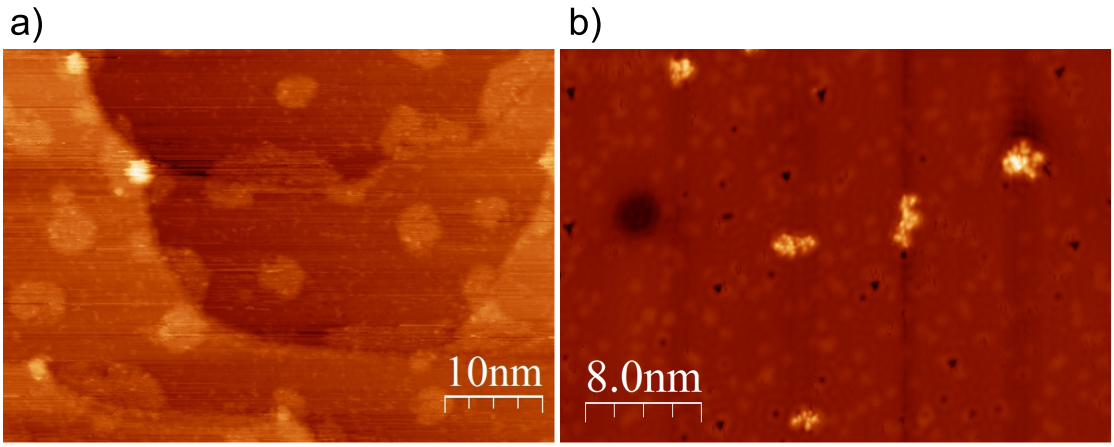

Figure 6.10 **a)** Contamination on the Cu(111) surface after the cold transfer. Mobile contaminants are forming semi-stable islands which distort the tip apex during the scanning. **b)** Overview image of the man5mer molecules on the Cu(111) surface after warming up to 220 K. Image parameters: constant current, 10 pA, 1 V.

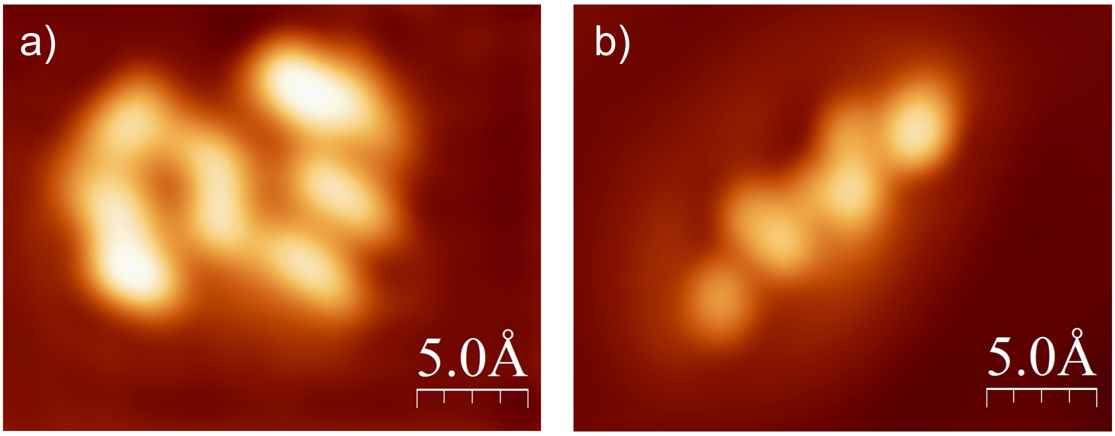

Figure 6.11 **a)** and **b)** Examples of nonclustered man5mer molecules on Cu(111). Image parameters: constant current, 10 pA, 1 V.

6.6 Analysis of the linear man5mer topography

In order to gain a better understanding of the man5mer topography, we measure the size of repeatable features and compare them with the estimated sizes of monomers and dimers of mannose. The sizes of the topographic features have been obtained by measuring and averaging 5 examples of each feature. It yielded the error of ±0.5 Å for the planar dimensions and ±1 Å for the height. The values obtained for the three most common features of the Cu(100) clusters are depicted in Fig. 6.12. The symmetric feature **1** (*7*x*3* Å) forms a triangular assembly with asymmetric **2** (*9*x*3.5-4.5* Å). The neighboring row consists of the asymmetric features **3** (*8*x*3-5* Å). The topographic height for the observed protrusions ranges from *9* Å for the lower parts, up to *13* Å for the highest parts.

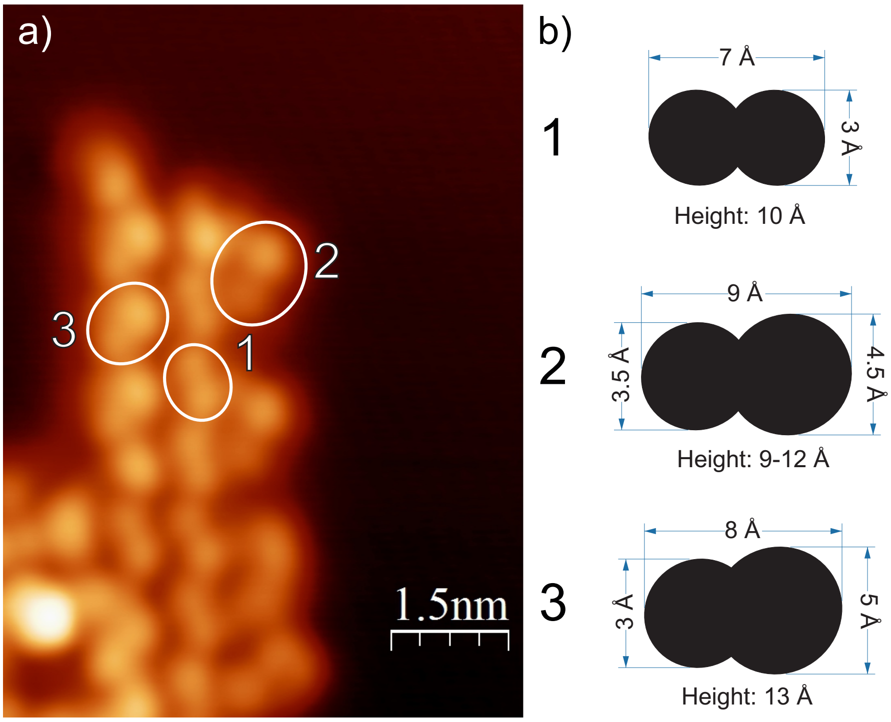

Figure 6.12 Topographic size of the three types of features observed on Cu(100), each repeating itself in the semi-organized rows. Image parameters: constant current, 100 pA, 100 mV.

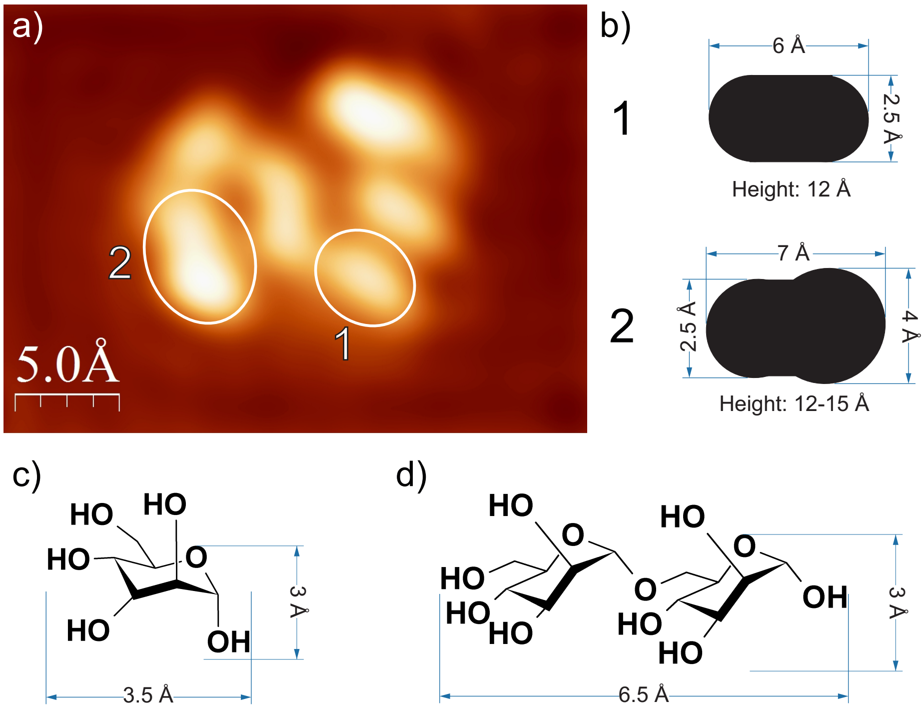

Figure 6.13 The analysis of the topographic features of the nonclustered man5mer molecules on Cu(111). **a)** Investigated structure. Image parameters: constant current, 10 pA, 1 V. **b)** Measured size of the features observed in a). **c)** and **d)** The size of mannose monomers and dimers in the gas phase.

Adequate analysis has been performed for the non-clustered species presented in Fig. 6.11 a) and are depicted in Fig. 6.13. The symmetric feature **1** (*6*x*2.5* Å) is appearing in the 2:1 ratio with asymmetric **2** (*7*x*2.5-4* Å). Both the ratio of the appearance and the ratio of size between **1** and **2** indicate that they may correspond to the features **1** and **2** observed in the clusters on Cu(100). Moreover, we estimate the size of the mannose monomers and dimers in the gas phase (with *Avogadro* software), obtaining *3.5*x*3* Å and (*6.5*x*3* Å), respectively.

A comparison of the measured size of the topographic appearances of man5mer features with the gas phase size estimation may hint which parts of the man5mer are observed directly. The summary of these values is presented in Table 6.1. The estimated size for a single mannose unit is too small to correspond to the most repeating features **1**. On both Cu(100) and Cu(111), they may be interpreted as mannose dimers, what is indicated by their sizes (light blue shading in the table). Moreover, the smaller part of the asymmetric protrusion **2** is comparable with **1** on both surfaces, indicating that **2** comprises of one mannose unit and one other entity (most probably an alkyl chain with an amine group). These interpretations are supported by the fact that the features **1** and **2** appear in a 2:1 ratio, yielding five mannose units and one alkyl chain, thus, a full man5mer molecule. The asymmetric entity **3** cannot be directly interpreted and most likely corresponds to a different conformation of the parts of man5mer. It is stabilized only in clusters and does not appear in isolated molecules.

Feature	1 Cu(100)	2 Cu(100)	3 Cu(100)	1 Cu(111)	2 Cu(111)	man	2-man
Length	7	9	8	6	7	3.5	6.5
Width	3	3.5-4.5	3-5	2.5	2.5-4.5	3	3
Height	10	9-12	13	12	12-15	-	-

Table 6.1 Comparison of linear man5mer features. All dimensions are given in Å. Light blue shading indicate features possibly corresponding to mannose dimers.

The conclusions drawn from the analysis of the observed topographic features allow us to assume that the structures depicted in Fig. 6.11 a) and b) correspond to two man5mer molecules and one man5mer molecule, respectively (Fig. 6.14). In b) and d), the two mannose dimers are located in the middle of the molecule, splitting the fifth mannose unit and the alkyl chain into two separated topographic features.

The interpretation of the STM topographic images of the man5mer molecules adsorbed on Cu(100) and Cu(111) is not definite and only indicates the positions of the building blocks without providing fine details of the structure. In order to reveal these details, the support of MD or DFT simulations is required. These techniques, due to the high flexibility of man5mer (and of all glycans) structure, are far from trivial and also might not provide conclusive results. Nevertheless, the topographic appearance of the basic building blocks of the on-surface man5mer molecules was revealed and analyzed, significantly improving the understanding of the conformation of the linear man5mer molecules on metal surfaces.

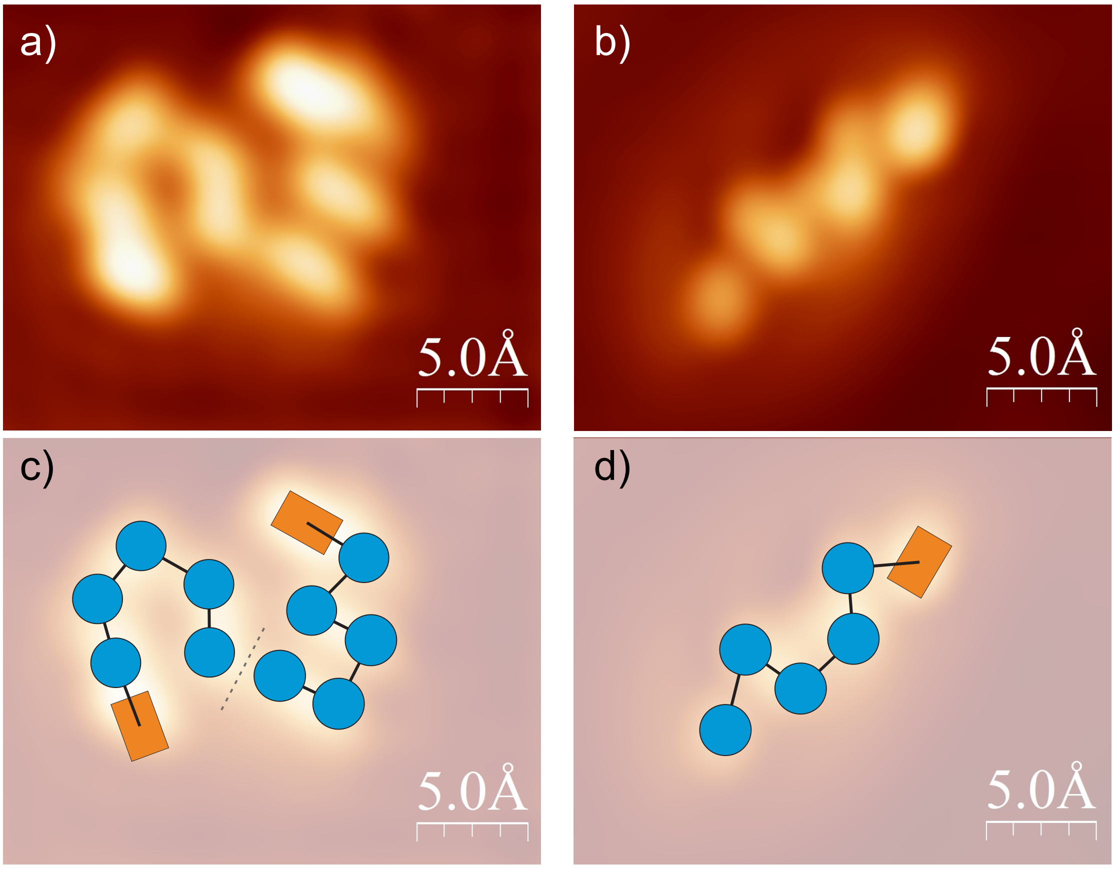

Figure 6.14 **a)** and **b)** Examples of nonclustered man5mer molecules. **c)** and **d)** Interpretation of the structures in a) and b). Orange rectangles correspond to the NH_2 terminated alkyl chain, blue circles to single mannose units. Image parameters: constant current, 10 pA, 1 V.

6.7 Branched hexamers on Cu(111)

The man6mer molecules were deposited with ES-IBD onto the Cu(111) surface held at room temperature. The molecules are clustered, however, not as strong as linear man5mer on Cu(100), despite the fact that Cu(111) is less coordinating (Fig 6.15). This may indicate that the two branching points render the man6mer structure less flexible, thus, weakening the diffusion. A similar effect was mentioned in section 6.1; as less branched polymers of glucose fold easier, this results in a higher density of their crystal forms.

Similarly to linear man5mer clusters on Cu(100), we have observed the organized assemblies that were adjacent to disorganized clusters (Fig. 6.16 a)). The repeating substructure consist of one topographically high protrusion **A**, Y-shaped uniform feature **B** and two round, low intensity protrusions **C** (Fig. 6.16 b)). The topographic height and type of these features resemble the structure of a single man5mer molecule depicted in Fig. 6.14 b) and d), i.e. one round protrusion of high intensity, the middle of the molecule with uniform topography and a feature of low intensity. In order to interpret the observed man6mer structure, we followed results achieved in the analysis of the linear man5mer. As depicted in Fig. 6.16 c), we interpret

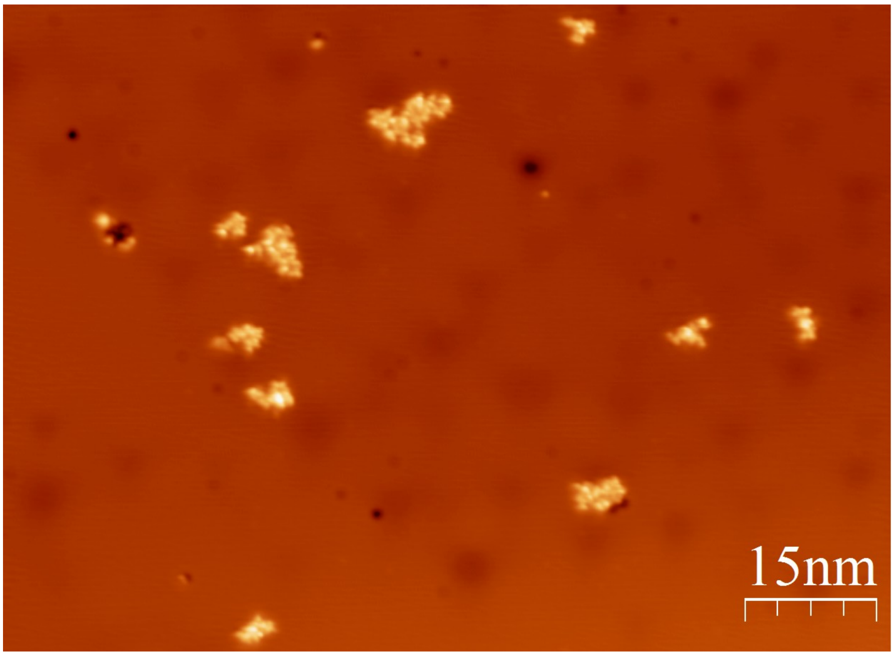

Figure 6.15 Overview of branched man5mer molecules on Cu(111). Clustering is observed, although it is less prominent than the clustering of linear man5mer molecules. Image parameters: constant current, 10 pA, 1 V.

the high-intensity lobe **A** as a folded alkyl chain, Y-shaped feature **B** as an assembly of four mannose building blocks and protrusions **C** as two individual mannose units. According to this interpretation, we can approximate the position of the branching points at the second and third mannose units (counting from the amine group). This is the first strong indication that we are indeed able to resolve the branched structure of glycans with STM.

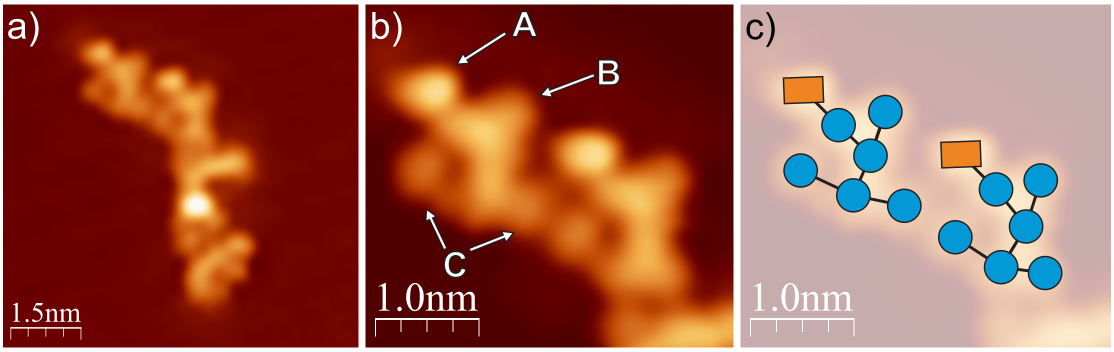

Figure 6.16 a) Substructure observed in man6mer clusters. **b)** Zoom of the structure depicted in a). **c)** Interpretation of the structure in b). Orange rectangles correspond to the NH_2 terminated carbon chain, blue circles to single mannose units. image parameters: constant current, 10 pA, 1 V.

The results presented in this section are preliminary and, as well as the results concerning the linear man5mer glycans, are part of an ongoing project. The interpretations of the observed topographic appearances are only propositions, which possibly indicate the structural differences between linear and branched glycans. We expect that in the course of the next experiments, we will be able to use the SPM techniques to localize the branching points with even higher certainty and perform precise quantitative analysis of the carbohydrate sequence, i.e. the number of the building blocks in each branch. In the next steps, we intend to check if the assemblies of different organized geometries are present along with the man6mer clusters, as well as to obtain single branched man6mer molecules, utilizing the cold ES-IBD technique. Furthermore, as the Pauli repulsion imaging has been already used to resolve the submolecular structure of bigger molecules prepared with ES-IBD (Chapter 5), we plan to utilize this technique to gain an even better understanding of the structural nuances of branched glycans. We have obtained the first, proof-of-concept image of an irregular cluster of the branched hexamers of mannose. Mannose units can be located in the observed structure, confirming the possibility of the Pauli repulsion imaging of carbohydrates (blue circle in Fig. 6.17). The same technique may also be applied to the linear pentamers.

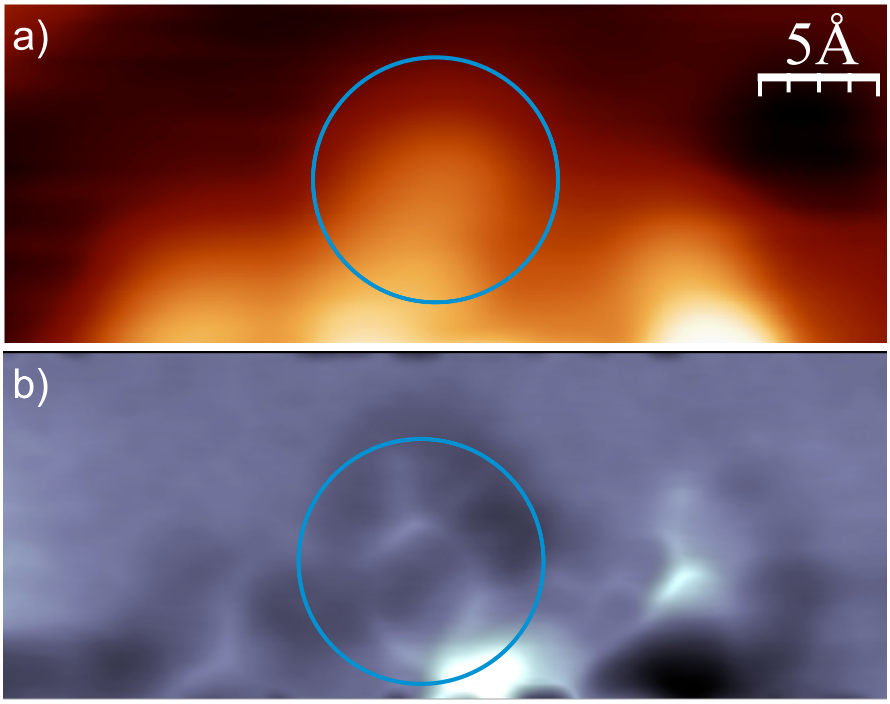

Figure 6.17 Pauli repulsion imaging of an irregular cluster of branched hexamers of mannose. **a)** Constant current STM image of an edge of a cluster, set point: 10 pA, 1 V. **b)** Frequency shift image of the area depicted in a), with the same scale. Features resembling single monosaccharides are resolvable (an example is marked with a blue circle).

6.8 Conclusions

In this chapter, we presented the first results of an ongoing project that aims to resolve the branched structures of carbohydrates. The main goal of this research is to evaluate combined STM/nc-AFM techniques (assisted by ES-IBD) as a complementary technique in the structural analysis of glycans. The real-space imaging performed by the SPM methods may provide information inaccessible (or accessible with high material cost) with MS and NMR. This is especially promising for the investigation of the branched structures of this group of biologically relevant molecules. In order to test this capability, we focused on the linear and branched polymers of mannose. We investigated both clustered and non-clustered linear man5mer molecules. In both types of observed structures, we identified topographic building blocks, which we assume to be mannose dimers, mannose-alkyl chain entities and, rarely, single mannose units. The information about the topographic appearance of linear polymers of mannose adsorbed on metal surfaces allowed us to begin the investigation of branched man6mer molecules. In the obtained clusters, we observed repeating features, and on the base of previously gained information, we were able to estimate the structure of the features and possibly identify the branching points.

Despite the preliminary character of the results and the analysis, they have confirmed that the combined STM/nc-AFM technique is a promising approach for the structural analysis of glycans. Moreover, it emphasized the crucial role of the ES-IBD technique for the preparation of samples yielding high-quality results. Based on these experiments, the project will be continued, possibly bringing attention in the field of glycomics to the real-space imaging approach.

7 Summary and outlook

Development of combined STM/nc-AFM instrument

During the course of this thesis, we developed a combined STM/nc-AFM instrument operating at liquid helium temperature and under UHV conditions. The performance of the machine has been optimized, profiting from the low noise environment at the Precision Lab of Max Planck Institute for Solid State Research. We obtained a vibration level below 1 pm that allows even the most precise experiments, such as the Pauli repulsion imaging. The ability to image surfaces with the atomic resolution was proven for both metallic surfaces and thin insulator layers. Moreover, the instrument is now fully capable of performing simultaneous and decoupled STM and nc-AFM measurements. The submolecular resolution nc-AFM images of pentacene structural analogs were demonstrated as a proof of its capabilities.

The samples containing organic molecules, which were not volatile or stable during thermal deposition, were prepared with ES-IBD and transported to the 4 K STM/nc-AFM via the vacuum suitcase. In the long term, the low-temperature deposition could be integrated with the 4 K STM/nc-AFM instrument with a mobile ES-IBD station designed for *in-situ* deposition on the substrates located directly in the 4 K STM/nc-AFM. Using one of the existing tip-sample junction access ports, a beam of the intact molecular ions could be guided into the instrument's head, where the sample is localized. The instrument is equipped with additional wiring, which could be used for the integration of the ion optics necessary for guiding the beam in the measurement chamber. The bigger challenge would be the construction of the miniaturized and mobile ES-IBD station itself. Integration of these devices would allow for deposition of bigger molecular species directly at the sample at ~ 10 K, thus, strongly limiting the diffusion of surface adsorbates due to the low temperature of the substrate. Furthermore, potential contamination problems occurring due to the transfer of the samples via the vacuum suitcase and load-locks could be avoided with this approach.

On-surface desulfurization of thiophene functional groups

The removal of sulfur from organic compounds bears significant importance in the petroleum industry. Especially, the field of heterogeneous catalysis of the raw fuels can profit from finding new desulfurization reaction pathways that utilize the catalytic properties of metal surfaces. Here, the on-surface desulfurization reactions of thiophene moieties embedded in the TCT molecules were investigated with STM and nc-AFM. TCT is a structural derivate of pentacene and its tetracene part exhibits similar stability on metal surfaces, which allowed the high-precision research concerning the chemistry of the thiophene group. We introduced two different approaches for the on-surface desulfurization of TCT on Cu(111) surface: global and local. In the global approach, we triggered the reaction with the elevation of the temperature of the sample up to 330 K, forcing all of the TCT molecules on the sample into a desulfurized state. In the second, local approach, we showed the possibility of addressing the individual thiophene moieties with an STM tip. Utilizing the electric field as the driving stimulus, we were able to follow the two elementary steps of the reaction. With the high-resolution STM and submolecular nc-AFM imaging, we resolved the molecular structures of both intact and reacted TCT molecules, confirming that global and local pathways result in the same desulfurized species. Apart from the removal of the S atom, the reaction resulted in anchoring of the molecules to the Cu(111) surface via direct C-S bonds. We have observed 50 % increase in the electric conductance measured through the molecule after the reaction, as compared to the intact TCT species.

The electric field driven reaction is of potential interest also outside the SPM field. The role of the electric field in the chemistry of organic molecules is yet to be fully understood and has been recently studied by other groups, where it was used to enhance the catalytical activity during the chemical reactions [283]–[285]. In our study, the electric field is the main stimulus to activate a desulfurization process. That suggests, that the role of the electric field in organic chemistry might be even broader, appearing as a novel approach for future studies.

The other, equally interesting outcome of this study, is the effect of the desulfurization reaction on the electronic and mechanical properties of the TCT molecule and its interaction with the underlying surface. The increase in mechanical stability and electric conductance suggests that the Cu(111) - thiophene reactions can be used to anchor organic molecules to metal electrodes for single-molecule electronics. The anchoring effect of thiophene groups has previously been studied, although the anchoring occurred only through adsorption and without modification of the inner chemical structure [286]. The formation of double covalent bonds by disruption of the thiophene functional group without an alteration of the rest of the structure brings a new perspective and provides an alternative technique to most widely used gold-thiol anchoring [240], [287]. Similarly to the thiol group, the thiophene moiety can be attached to any organic molecule in a controlled way [288], which emphasizes possible universality of this technique. Moreover, as proven by our research, the reaction does not affect the rest of the structure. Thus, the core molecules fulfilling the role of electronic circuit elements might not be affected. Moreover, the full control of the process is acquired in the range of easily accessible temperatures (below 250 K - no reaction, above 320 K - all thiophene groups reacted).

We suggest a follow-up study of the desulfurization reaction that could be realized with classical break junction approach. Usually, in this technique, the molecules are delivered to a junction consisting of two gold electrodes by flushing a molecular solution through it. This often results in adsorption of more than one molecule in the junction, if all of them have reactive anchoring groups. A test system for the thiophene desulfurization anchoring can consist of planar, π-conjugated molecules, terminated with two thiophene groups (Fig. 7.1). All of the suspended molecules could be then bonded by the temperature elevation. Alternatively, if bond formation in this system follows the same principle as in the STM experiments, the reaction could be induced selectively with an electric field. With a sufficient electric field, a single molecule placed at the narrowest point of the gap could be anchored. The rest of the molecules could be later removed, resulting in a controlled formation of a stable, explicitly single-molecule junction. The need for anchoring techniques different from the spontaneous formation of thiol-gold bonds has been already expressed [240] and the thiophene-copper system is one of the possible alternatives.

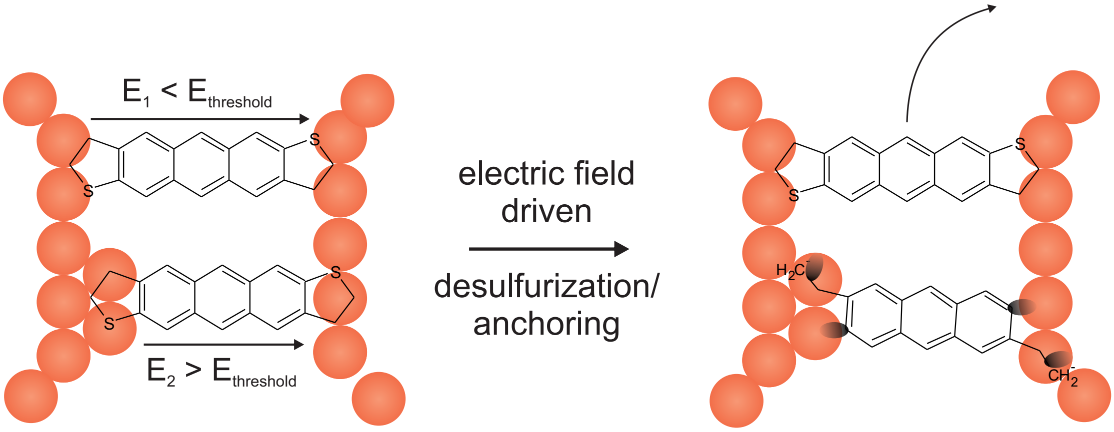

Figure 7.1 Idea of using the desulfurization of the thiophene moiety as an anchoring technique for single-molecule electronics. First, by flushing a molecular solution through the system, more than one molecule can be placed at the junction. As the anchoring reaction can be driven with the electric field between the electrodes, it is possible to induce only for the molecules suspended at the narrowest gap (as the field there would be the highest). The non-anchored molecules could be removed afterward, leading to a controlled creation of a truly single-molecule junction. The reaction can be also triggered thermally. In this case, both depicted molecules would be firmly anchored to the electrodes.

Hyperthermal reactions of Reichardt's Dye

Hyperthermal collisions of particles with surfaces offer an alternative approach to the on-surface chemistry of organic molecules, overcoming the limitations of the thermally induced processes. Upon collision, the kinetic energy of incident particles disperses in extremely short times (ps range). If the kinetic energy is high enough, it can be exploited to acquire thermally unobtainable states of organic molecules. We utilized ES-IBD to deposit the Reichardt's Dye (RD) molecules onto a Cu(100) surface, while simultaneously controlling their kinetic energy. In order to explore the possibility of acquiring new states, we first studied the thermally activated reactions carried out on the soft landed, intact molecules (kinetic energy below 5 eV). The investigation was carried with STM and nc-AFM, allowing for structural identification on the surface after the collisions. Thermally activated RD molecules were fragmented into two completely separated species. The fragmentation reaction involved breaking the middle C-N bond, which is the weakest in the structure. With the hyperthermal approach (kinetic energy ~30 eV), a new species was obtained, assumed to originate in the rupture of the middle pyridine unit, without scission of the weakest C-N bond. After the hyperthermal collisions, we found both intact and fragmented RD molecules, which suggests that the occurrence of the new states also depends on the geometry of the molecule during the highly energetic collision.

The hyperthermal collision of RD with Cu(100) resulted in the creation of a new molecular species, representing a novel approach to reaction kinetics. Our results show that high energy collisions allow for the crossing of high reaction barriers without inducing reactions with lower activation energy because we observed the breaking of the pyridine group of the RD molecule without fragmentation of the whole structure. This proves the concept of using the hyperthermal collisions as a way to acquire thermally inaccessible states in a non-equilibrium manner. We expect that more hyperthermally induced reactions can be found. The high precision, versatility and high output of the ES-IBD technique combined with control of the kinetic energy of the incident particle could be used as a fabrication method for devices based on functional molecules [289].

Carbohydrates on metal surfaces

Carbohydrates are biologically relevant molecules that exhibit structural complexity surpassing those of amino acids, peptides and proteins. The field of glycomics that focuses on identification, qualification and understanding of carbohydrates' roles in living organisms is underdeveloped as compared to proteomics and genomics, despite equal importance of all of these fields. One of the aspects that complicates the structural analysis of carbohydrates, slowing down the progress of glycomics, is their branching, as they can polymerize in a nonlinear manner. The identification of branched structures with standard methods like MS and NMR is difficult and has a high material cost. Elucidation of carbohydrate structure, often consisting of isomeric monosaccharide building blocks, requires a series of measurements aiming at different aspects of their structure. Each of these measurements requires another batch of the analyte, rapidly increasing the overall material cost, often to values inaccessible for the majority of carbohydrates, i.e. above 1 mg. A potential alternative is offered by the real space imaging approach that can be realized with the STM and nc-AFM techniques capable of identifying the molecular structure by analyzing single molecules. In an on-going project, we investigate, whether STM and nc-AFM imaging are capable of providing complementary information concerning the numerical sequence of investigated molecules: localizations of the branching points and the number of the monosaccharide building blocks in each branch.

In order to achieve this goal, we study linear and branched oligosaccharides separately and compare the results. All of the samples were fabricated by ES-IBD soft landing. First, we investigated both clustered and nonclustered linear pentamers of mannose on Cu(100) and Cu(111). We identified the basic features in the topographic appearance of the investigated oligosaccharide as consisting of two mannose units. We were able to estimate the adsorption geometry of the molecule up to the single building block level. Next, we moved to the hexamers of mannose, with two branching points at the second and third units of the main branch. Based on the information gained from the topographic investigation of linear oligosaccharides, we located the two branching points in the branched structures on Cu(111). Although the results are preliminary, they show the potential of the combination of STM/nc-AFM and ES-IBD to become a complementary approach to the structural analysis of carbohydrates.

We plan to continue this project with the following experiments. First, we intend to further experiment with the Pauli repulsion imaging and to apply this technique for both the branched and linear molecules. Next experiments with branched oligosaccharides deposited in low temperatures will be carried out, in order to acquire non-clustered branched molecules. Additionally, the system could be switched to oligosaccharides consisting of glucose units. They exhibit hydrogen bonding between each glucose monosaccharide, reducing their flexibility [290] and leading to a smaller number of available conformations on the surface, weaker diffusion processes, and thus, less clustered structures.

In the far future, after completing the proof-of-concept study, we may extend the investigation of carbohydrates handled by ES-IBD to blind tests. The goal would be to analyze "unknown" oligosaccharides only on the basis of the mass spectrometry results (yielding information about the total number of monosaccharide units) and the STM/nc-AFM imaging. If the branching sequence could be directly identified with the real space imaging, it would serve as a final proof that this set of methods could be used as a complementary approach for identification of biologically relevant carbohydrates.

Bibliography

[1] M. O. Byrd and C. J. Ohrenberg, “The Use of Ammonia as a Qualitative Test for Determining When Solid Copper Has Completely Precipitated from Aqueous Solutions Containing Copper(II) Ions,” vol. 75, p. 8, 2017.

[2] H. A. Laitinen, “History of analytical chemistry in the U.S.A.,” *Talanta*, vol. 36, pp. 1–9, Jan. 1989.

[3] J. D. Watson and F. H. C. Crick, “Molecular Structure of Nucleic Acids: A Structure for Deoxyribose Nucleic Acid,” *Nature*, vol. 171, pp. 737–738, Apr. 1953.

[4] J. R. Yates and J. R. Yates, “Mass spectrometry: From genomics to proteomics,” *Trends in Genetics*, vol. 16, pp. 5–8, Jan. 2000.

[5] L. Hahn, A. Hermannsdorfer, B. Günther, T. Wesp, B. Bühler, U. Zschieschang, H. Wadepohl, H. Klauk, and L. H. Gade, “(Oligo-)Thiophene Functionalized Tetraazaperopyrenes: Donor–Acceptor Dyes and Ambipolar Organic Semiconductors,” *The Journal of Organic Chemistry*, vol. 82, pp. 12492–12502, Dec. 2017.

[6] C. Scotter, “Use of near infrared spectroscopy in the food industry with particular reference to its applications to on/in-line food processes,” *Food Control*, vol. 1, pp. 142–149, July 1990.

[7] D. J. Gardiner and P. R. Graves, eds., *Practical Raman Spectroscopy.* Berlin Heidelberg: Springer-Verlag, 1989.

[8] P. J. Hendra and P. M. Stratton, “Laser-Raman spectroscopy,” *Chem. Rev.*, vol. 69, pp. 325–344, June 1969.

[9] M. Ladd and R. Palmer, *Structure Determination by X-Ray Crystallography: Analysis by X-Rays and Neutrons.* Springer US, 5 ed., 2013.

[10] M. T. B. Clabbers, E. van Genderen, W. Wan, E. L. Wiegers, T. Gruene, and J. P. Abrahams, “Protein structure determination by electron diffraction using a single three-dimensional nanocrystal,” *Acta Crystallographica D Structural Biology*, vol. 73, pp. 738–748, Aug. 2017.

[11] M. T. Weller, P. F. Henry, V. P. Ting, and C. C. Wilson, “Crystallography of hydrogen-containing compounds: Realizing the potential of neutron powder diffraction,” *Chemical Communications*, no. 21, p. 2973, 2009.

[12] K. Fucke and J. W. Steed, “X-ray and Neutron Diffraction in the Study of Organic Crystalline Hydrates,” *Water*, vol. 2, pp. 333–350, Sept. 2010.

[13] I. I. Rabi, J. R. Zacharias, S. Millman, and P. Kusch, “A New Method of Measuring Nuclear Magnetic Moment,” *Physical Review*, vol. 53, pp. 318–318, Feb. 1938.

[14] H. Günther, *NMR Spectroscopy: Basic Principles, Concepts, and Applications in Chemistry*. Wiley, Aug. 1995.

[15] F. V. Toukach and V. P. Ananikov, “Recent advances in computational predictions of NMR parameters for the structure elucidation of carbohydrates: Methods and limitations,” *Chem. Soc. Rev.*, vol. 42, pp. 8376–8415, Oct. 2013.

[16] D. J. Harvey, “Fragmentation of negative ions from carbohydrates: Part 1. Use of nitrate and other anionic adducts for the production of negative ion electrospray spectra from N-linked carbohydrates,” *Journal of the American Society for Mass Spectrometry*, vol. 16, pp. 622–630, May 2005.

[17] A. Dell and H. R. Morris, “Glycoprotein Structure Determination by Mass Spectrometry,” *Science*, vol. 291, pp. 2351–2356, Mar. 2001.

[18] M. Balci, *Basic 1H- and 13C-NMR Spectroscopy*. Elsevier, 2005.

[19] K. Mariño, J. Bones, J. J. Kattla, and P. M. Rudd, “A systematic approach to protein glycosylation analysis: A path through the maze,” *Nature Chemical Biology*, vol. 6, pp. 713–723, Oct. 2010.

[20] G. W. Hart and R. J. Copeland, “Glycomics Hits the Big Time,” *Cell*, vol. 143, pp. 672–676, Nov. 2010.

[21] P. H. Seeberger, “Chemical glycobiology: Why now?,” *Nature Chemical Biology*, vol. 5, pp. 368–372, June 2009.

[22] S. G. Lipson, S. G. Lipson, H. Lipson, and D. S. Tannhauser, *Optical Physics*. Cambridge University Press, July 1995.

[23] A. Tzur, R. Kafri, V. S. LeBleu, G. Lahav, and M. W. Kirschner, “Cell Growth and Size Homeostasis in Proliferating Animal Cells,” *Science*, vol. 325, pp. 167–171, July 2009.

[24] U. Dürig, D. W. Pohl, and F. Rohner, “Near-field optical-scanning microscopy,” *Journal of Applied Physics*, vol. 59, pp. 3318–3327, May 1986.

[25] Y. Oshikane, T. Kataoka, M. Okuda, S. Hara, H. Inoue, and M. Nakano, “Observation of nanostructure by scanning near-field optical microscope with small sphere probe,” *Science and Technology of Advanced Materials*, vol. 8, pp. 181–185, Jan. 2007.

[26] T. Müller, C. Schumann, and A. Kraegeloh, "STED Microscopy and its Applications: New Insights into Cellular Processes on the Nanoscale," *ChemPhysChem*, vol. 13, pp. 1986–2000, June 2012.

[27] "Nanotechnology Now: Hitachi Launches World's Highest Resolution FE-SEM." http://www.nanotech-now.com/news.cgi?story_id=42612.

[28] R. Erni, M. D. Rossell, C. Kisielowski, and U. Dahmen, "Atomic-Resolution Imaging with a Sub-50-pm Electron Probe," *Phys. Rev. Lett.*, vol. 102, p. 096101, Mar. 2009.

[29] P. W. Hawkes and J. C. H. Spence, eds., *Science of Microscopy.* New York: Springer, 2007.

[30] Z. J. W. A. Leijten, A. D. A. Keizer, G. de With, and H. Friedrich, "Quantitative Analysis of Electron Beam Damage in Organic Thin Films," *The Journal of Physical Chemistry C*, vol. 121, pp. 10552–10561, May 2017.

[31] M. Adrian, J. Dubochet, J. Lepault, and A. W. McDowall, "Cryo-electron microscopy of viruses," *Nature*, vol. 308, p. 32, Mar. 1984.

[32] W. Kühlbrandt, "Cryo-EM enters a new era," *eLife*, vol. 3, Aug. 2014.

[33] G. Binnig, H. Rohrer, C. Gerber, and E. Weibel, "Surface Studies by Scanning Tunneling Microscopy," *Physical Review Letters*, vol. 49, pp. 57–61, July 1982.

[34] C. Bai, *Scanning Tunneling Microscopy and Its Application.* Springer Series in Surface Sciences, Berlin Heidelberg: Springer-Verlag, 2 ed., 2000.

[35] L. Limot, J. Kröger, R. Berndt, A. Garcia-Lekue, and W. A. Hofer, "Atom Transfer and Single-Adatom Contacts," *Phys. Rev. Lett.*, vol. 94, p. 126102, Apr. 2005.

[36] S. Kahle, Z. Deng, N. Malinowski, C. Tonnoir, A. Forment-Aliaga, N. Thontasen, G. Rinke, D. Le, V. Turkowski, T. S. Rahman, S. Rauschenbach, M. Ternes, and K. Kern, "The Quantum Magnetism of Individual Manganese-12-Acetate Molecular Magnets Anchored at Surfaces," *Nano Lett.*, vol. 12, pp. 518–521, Jan. 2012.

[37] M. Assig, M. Etzkorn, A. Enders, W. Stiepany, C. R. Ast, and K. Kern, "A 10 mK scanning tunneling microscope operating in ultra high vacuum and high magnetic fields," *Review of Scientific Instruments*, vol. 84, p. 033903, Mar. 2013.

[38] B. E. Feldman, M. T. Randeria, J. Li, S. Jeon, Y. Xie, Z. Wang, I. K. Drozdov, B. Andrei Bernevig, and A. Yazdani, "High-resolution studies of the Majorana atomic chain platform," *Nature Physics*, vol. 13, pp. 286–291, Mar. 2017.

[39] F. Meier, L. Zhou, J. Wiebe, and R. Wiesendanger, "Revealing Magnetic Interactions from Single-Atom Magnetization Curves," *Science*, vol. 320, pp. 82–86, Apr. 2008.

[40] I. G. Rau, S. Baumann, S. Rusponi, F. Donati, S. Stepanow, L. Gragnaniello, J. Dreiser, C. Piamonteze, F. Nolting, S. Gangopadhyay, O. R. Albertini, R. M. Macfarlane, C. P. Lutz, B. A. Jones, P. Gambardella, A. J. Heinrich, and H. Brune, "Reaching the magnetic anisotropy limit of a 3d metal atom," *Science*, vol. 344, pp. 988–992, May 2014.

[41] A. Rosławska, P. Merino, C. Große, C. C. Leon, O. Gunnarsson, M. Etzkorn, K. Kuhnke, and K. Kern, "Single Charge and Exciton Dynamics Probed by Molecular-Scale-Induced Electroluminescence," *Nano Lett.*, vol. 18, pp. 4001–4007, June 2018.

[42] M. C. Chong, N. Afshar-Imani, F. Scheurer, C. Cardoso, A. Ferretti, D. Prezzi, and G. Schull, "Bright Electroluminescence from Single Graphene Nanoribbon Junctions," *Nano Lett.*, vol. 18, pp. 175–181, Jan. 2018.

[43] D. M. Cyr, B. Venkataraman, G. W. Flynn, A. Black, and G. M. Whitesides, "Functional Group Identification in Scanning Tunneling Microscopy of Molecular Adsorbates," *J. Phys. Chem.*, vol. 100, pp. 13747–13759, Jan. 1996.

[44] R. Temirov, S. Soubatch, O. Neucheva, A. C. Lassise, and F. S. Tautz, "A novel method achieving ultra-high geometrical resolution in scanning tunnelling microscopy," *New J. Phys.*, vol. 10, no. 5, p. 053012, 2008.

[45] C. Weiss, C. Wagner, R. Temirov, and F. S. Tautz, "Direct Imaging of Intermolecular Bonds in Scanning Tunneling Microscopy," *Journal of the American Chemical Society*, vol. 132, pp. 11864–11865, Sept. 2010.

[46] C. Weiss, C. Wagner, C. Kleimann, M. Rohlfing, F. S. Tautz, and R. Temirov, "Imaging Pauli Repulsion in Scanning Tunneling Microscopy," *Physical Review Letters*, vol. 105, Aug. 2010.

[47] C. Wagner and R. Temirov, "Tunnelling junctions with additional degrees of freedom: An extended toolbox of scanning probe microscopy," *Progress in Surface Science*, vol. 90, pp. 194–222, May 2015.

[48] L. Gross, F. Mohn, N. Moll, P. Liljeroth, and G. Meyer, "The Chemical Structure of a Molecule Resolved by Atomic Force Microscopy," *Science*, vol. 325, pp. 1110–1114, Aug. 2009.

[49] B. Schuler, S. Fatayer, G. Meyer, E. Rogel, M. Moir, Y. Zhang, M. R. Harper, A. E. Pomerantz, K. D. Bake, M. Witt, D. Peña, J. D. Kushnerick, O. C. Mullins, C. Ovalles, F. G. A. van den Berg, and L. Gross, "Heavy Oil Based Mixtures of Different Origins and Treatments Studied by Atomic Force Microscopy," *Energy Fuels*, vol. 31, pp. 6856–6861, July 2017.

[50] G. Binnig, H. Rohrer, C. Gerber, and E. Weibel, "Tunneling through a controllable vacuum gap," *Appl. Phys. Lett.*, vol. 40, pp. 178–180, Jan. 1982.

[51] G. Binnig and H. Rohrer, "Scanning tunneling microscopy," *Surface Science*, vol. 152-153, pp. 17–26, Apr. 1985.

[52] R. S. Becker, J. A. Golovchenko, E. G. McRae, and B. S. Swartzentruber, “Tunneling Images of Atomic Steps on the Si(111)7×7 Surface,” *Physical Review Letters*, vol. 55, pp. 2028–2031, Nov. 1985.

[53] K. Morgenstern, N. Lorente, and K.-H. Rieder, “Controlled manipulation of single atoms and small molecules using the scanning tunnelling microscope,” *Physica Status Solidi B*, vol. 250, pp. 1671–1751, Sept. 2013.

[54] S.-W. Hla, L. Bartels, G. Meyer, and K.-H. Rieder, “Inducing All Steps of a Chemical Reaction with the Scanning Tunneling Microscope Tip: Towards Single Molecule Engineering,” *Physical Review Letters*, vol. 85, pp. 2777–2780, Sept. 2000.

[55] M. G. L. van den Heuvel and C. Dekker, “Motor Proteins at Work for Nanotechnology,” *Science*, vol. 317, pp. 333–336, July 2007.

[56] M. Schliwa and G. Woehlke, “Molecular motors,” *Nature*, vol. 422, pp. 759–765, Apr. 2003.

[57] P. C. W. Davies, “Quantum tunneling time,” *American Journal of Physics*, vol. 73, pp. 23–27, Jan. 2005.

[58] M. Razavy, *Quantum Theory of Tunneling*. World Scientific, 2003.

[59] “The 1986 Nobel Prize in Physics,” press release.

[60] C. J. Chen, “Introduction to Scanning Tunneling Microscopy,” *Introduction to Scanning Tunneling Microscopy*, p. 26, 2008.

[61] P. Avouris, I. W. Lyo, and P. Molinàs-Mata, “STM studies of the interaction of surface state electrons on metals with steps and adsorbates,” *Chemical Physics Letters*, vol. 240, pp. 423–428, July 1995.

[62] G. Hörmandinger, “Imaging of the Cu(111) surface state in scanning tunneling microscopy,” *Phys. Rev. B*, vol. 49, pp. 13897–13905, May 1994.

[63] J. Lagoute, K. Kanisawa, and S. Fölsch, “Manipulation and adsorption-site mapping of single pentacene molecules on Cu(111),” *Physical Review B*, vol. 70, Dec. 2004.

[64] R. Mishima, M. Takada, and H. Tada, “STM Studies of NaCl Thin Films on Cu(111) Surface at Low Temperature,” *Molecular Crystals and Liquid Crystals*, vol. 472, pp. 321–325, Aug. 2007.

[65] R. Wiesendanger and W. Roland, *Scanning Probe Microscopy and Spectroscopy: Methods and Applications*. Cambridge University Press, Sept. 1994.

[66] B. Voigtländer, *Scanning Probe Microscopy: Atomic Force Microscopy and Scanning Tunneling Microscopy*. Springer, Feb. 2015.

[67] J. Tersoff and D. R. Hamann, "Theory and Application for the Scanning Tunneling Microscope," *Physical Review Letters*, vol. 50, pp. 1998–2001, June 1983.

[68] J. Tersoff and D. R. Hamann, "Theory of the scanning tunneling microscope," *Physical Review B*, vol. 31, pp. 805–813, Jan. 1985.

[69] R. Sarkar, C. Rentenberger, and J. Rajagopalan, "Electron Beam Induced Artifacts During in situ TEM Deformation of Nanostructured Metals," *Sci Rep*, vol. 5, Nov. 2015.

[70] D. M. Eigler and E. K. Schweizer, "Positioning single atoms with a scanning tunnelling microscope," *Nature*, vol. 344, pp. 524–526, Apr. 1990.

[71] F. E. Kalff, M. P. Rebergen, E. Fahrenfort, J. Girovsky, R. Toskovic, J. L. Lado, J. Fernández-Rossier, and A. F. Otte, "A kilobyte rewritable atomic memory," *Nature Nanotechnology*, vol. 11, pp. 926–929, Nov. 2016.

[72] M. F. Crommie, C. P. Lutz, and D. M. Eigler, "Confinement of Electrons to Quantum Corrals on a Metal Surface," *Science*, vol. 262, pp. 218–220, Oct. 1993.

[73] S.-W. Hla, K.-F. Braun, and K.-H. Rieder, "Single-atom manipulation mechanisms during a quantum corral construction," *Phys. Rev. B*, vol. 67, p. 201402, May 2003.

[74] D. M. Eigler, C. P. Lutz, and W. E. Rudge, "An atomic switch realized with the scanning tunnelling microscope," *Nature*, vol. 352, p. 600, Aug. 1991.

[75] B. Neu, G. Meyer, and K.-H. Rieder, "Controlled vertical and lateral manipulation of single atoms and molecules with the scanning tunneling microscope," *Mod. Phys. Lett. B*, vol. 09, pp. 963–969, June 1995.

[76] X. Bouju, C. Joachim, C. Girard, and P. Sautet, "Imaging and moving a xenon atom on a copper (110) surface with the tip of a scanning tunneling microscope: A theoretical study," *Phys. Rev. B*, vol. 47, pp. 7454–7461, Mar. 1993.

[77] D. M. Eigler, P. S. Weiss, E. K. Schweizer, and N. D. Lang, "Imaging Xe with a low-temperature scanning tunneling microscope," *Physical Review Letters*, vol. 66, pp. 1189–1192, Mar. 1991.

[78] L. Bartels, G. Meyer, and K.-H. Rieder, "Controlled vertical manipulation of single CO molecules with the scanning tunneling microscope: A route to chemical contrast," *Applied Physics Letters*, vol. 71, pp. 213–215, July 1997.

[79] R. Raval, S. F. Parker, M. E. Pemble, P. Hollins, J. Pritchard, and M. A. Chesters, "FT-rairs, eels and leed studies of the adsorption of carbon monoxide on Cu(111)," *Surface Science*, vol. 203, pp. 353–377, Sept. 1988.

[80] L. Bartels, G. Meyer, K.-H. Rieder, D. Velic, E. Knoesel, A. Hotzel, M. Wolf, and G. Ertl, "Dynamics of Electron-Induced Manipulation of Individual CO Molecules on Cu(111)," *Phys. Rev. Lett.*, vol. 80, pp. 2004–2007, Mar. 1998.

[81] "A Boy And His Atom: The World's Smallest Movie." http://ibm.co/ZyRmcT, May 2013.

[82] L. Lafferentz, F. Ample, H. Yu, S. Hecht, C. Joachim, and L. Grill, "Conductance of a Single Conjugated Polymer as a Continuous Function of Its Length," *Science*, vol. 323, pp. 1193–1197, Feb. 2009.

[83] N. Fournier, C. Wagner, C. Weiss, R. Temirov, and F. S. Tautz, "Force-controlled lifting of molecular wires," *Phys. Rev. B*, vol. 84, p. 035435, July 2011.

[84] S. K. Kufer, E. M. Puchner, H. Gumpp, T. Liedl, and H. E. Gaub, "Single-Molecule Cut-and-Paste Surface Assembly," *Science*, vol. 319, pp. 594–596, Feb. 2008.

[85] K. S. Nakayama, E. Graugnard, and J. H. Weaver, "Tunneling Electron Induced Bromine Hopping," *Phys. Rev. Lett.*, vol. 89, p. 266106, Dec. 2002.

[86] Y. Nakamura, Y. Mera, and K. Maeda, "Hopping motion of chlorine atoms on Si(100)-(2×1) surfaces induced by carrier injection from scanning tunneling microscope tips," *Surface Science*, vol. 531, pp. 68–76, May 2003.

[87] T. Kumagai, M. Kaizu, H. Okuyama, S. Hatta, T. Aruga, I. Hamada, and Y. Morikawa, "Tunneling dynamics of a hydroxyl group adsorbed on Cu(110)," *Phys. Rev. B*, vol. 79, p. 035423, Jan. 2009.

[88] K. Motobayashi, C. Matsumoto, Y. Kim, and M. Kawai, "Vibrational study of water dimers on Pt(111) using a scanning tunneling microscope," *Surface Science*, vol. 602, pp. 3136–3139, Oct. 2008.

[89] T. Komeda, Y. Kim, M. Kawai, B. N. J. Persson, and H. Ueba, "Lateral Hopping of Molecules Induced by Excitation of Internal Vibration Mode," *Science*, vol. 295, pp. 2055–2058, Mar. 2002.

[90] T.-C. Shen, C. Wang, G. C. Abeln, J. R. Tucker, J. W. Lyding, P. Avouris, and R. E. Walkup, "Atomic-Scale Desorption Through Electronic and Vibrational Excitation Mechanisms," *Science*, vol. 268, pp. 1590–1592, June 1995.

[91] R. S. Becker, G. S. Higashi, Y. J. Chabal, and A. J. Becker, "Atomic-scale conversion of clean Si(111):H-1 x 1 to Si(111)-2 x 1 by electron-stimulated desorption," *Phys. Rev. Lett.*, vol. 65, pp. 1917–1920, Oct. 1990.

[92] L. Bartels, M. Wolf, T. Klamroth, P. Saalfrank, A. Kühnle, G. Meyer, and K. H. Rieder, "Atomic-scale chemistry: Desorption of ammonia from Cu(111) induced by tunneling electrons," *Chemical Physics Letters*, vol. 313, pp. 544–552, Nov. 1999.

[93] P. A. Sloan, M. F. G. Hedouin, R. E. Palmer, and M. Persson, "Mechanisms of Molecular Manipulation with the Scanning Tunneling Microscope at Room Temperature: Chlorobenzene/Si(111)-(7x7)," *Phys. Rev. Lett.*, vol. 91, p. 118301, Sept. 2003.

[94] T. Minato, S. Kajita, C.-L. Pang, N. Asao, Y. Yamamoto, T. Nakayama, M. Kawai, and Y. Kim, "Tunneling Desorption of Single Hydrogen on the Surface of Titanium Dioxide," *ACS Nano*, vol. 9, pp. 6837–6842, July 2015.

[95] N. Henningsen, R. Rurali, K. J. Franke, I. Fernández-Torrente, and J. I. Pascual, "Trans to cis isomerization of an azobenzene derivative on a Cu(100) surface," *Applied Physics A*, vol. 93, Nov. 2008.

[96] M. Alemani, M. V. Peters, S. Hecht, K.-H. Rieder, F. Moresco, and L. Grill, "Electric Field-Induced Isomerization of Azobenzene by STM," *Journal of the American Chemical Society*, vol. 128, pp. 14446–14447, Nov. 2006.

[97] J. Henzl, M. Mehlhorn, H. Gawronski, K.-H. Rieder, and K. Morgenstern, "Reversible cis–trans Isomerization of a Single Azobenzene Molecule," *Angewandte Chemie International Edition*, vol. 45, pp. 603–606, Jan. 2006.

[98] B.-Y. Choi, S.-J. Kahng, S. Kim, H. Kim, H. W. Kim, Y. J. Song, J. Ihm, and Y. Kuk, "Conformational Molecular Switch of the Azobenzene Molecule: A Scanning Tunneling Microscopy Study," *Phys. Rev. Lett.*, vol. 96, p. 156106, Apr. 2006.

[99] X. H. Qiu, G. V. Nazin, and W. Ho, "Mechanisms of Reversible Conformational Transitions in a Single Molecule," *Physical Review Letters*, vol. 93, Nov. 2004.

[100] V. Iancu and S.-W. Hla, "Realization of a four-step molecular switch in scanning tunneling microscope manipulation of single chlorophyll-a molecules," *PNAS*, vol. 103, pp. 13718–13721, Sept. 2006.

[101] B. Borca, V. Schendel, R. Pétuya, I. Pentegov, T. Michnowicz, U. Kraft, H. Klauk, A. Arnau, P. Wahl, U. Schlickum, and K. Kern, "Bipolar Conductance Switching of Single Anthradithiophene Molecules," *ACS Nano*, vol. 9, pp. 12506–12512, Dec. 2015.

[102] V. Schendel, B. Borca, I. Pentegov, T. Michnowicz, U. Kraft, H. Klauk, P. Wahl, U. Schlickum, and K. Kern, "Remotely Controlled Isomer Selective Molecular Switching," *Nano Lett.*, vol. 16, pp. 93–97, Jan. 2016.

[103] R. Martel, P. Avouris, and I.-W. Lyo, "Molecularly Adsorbed Oxygen Species on Si(111)-(7×7): STM-Induced Dissociative Attachment Studies," *Science*, vol. 272, pp. 385–388, Apr. 1996.

[104] B. C. Stipe, M. A. Rezaei, W. Ho, S. Gao, M. Persson, and B. I. Lundqvist, "Single-Molecule Dissociation by Tunneling Electrons," *Phys. Rev. Lett.*, vol. 78, pp. 4410–4413, June 1997.

[105] J. R. Hahn, S. H. Jang, K. W. Kim, and S. B. Son, "Hot carrier-selective chemical reactions on Ag(110)," *J. Chem. Phys.*, vol. 139, p. 074707, Aug. 2013.

[106] C. Sprodowski, M. Mehlhorn, and K. Morgenstern, "Dissociation of oxygen on Ag(100) induced by inelastic electron tunneling," *J. Phys.: Condens. Matter*, vol. 22, no. 26, p. 264005, 2010.

[107] M. A. Rezaei, B. C. Stipe, and W. Ho, “Inducing and imaging single molecule dissociation on a semiconductor surface: $H_{2<\backslash sub>S\ and\ }D_{2<\backslash sub>S\ on\ Si(111)\text{-}7\times7}$,” *J. Chem. Phys.*, vol. 109, pp. 6075–6078, Oct. 1998.

[108] M. Mehlhorn, H. Gawronski, and K. Morgenstern, “Electron Damage to Supported Ice Investigated by Scanning Tunneling Microscopy and Spectroscopy,” *Phys. Rev. Lett.*, vol. 101, p. 196101, Nov. 2008.

[109] M. Ohara, Y. Kim, S. Yanagisawa, Y. Morikawa, and M. Kawai, “Role of Molecular Orbitals Near the Fermi Level in the Excitation of Vibrational Modes of a Single Molecule at a Scanning Tunneling Microscope Junction,” *Phys. Rev. Lett.*, vol. 100, p. 136104, Apr. 2008.

[110] G. Dujardin, R. E. Walkup, and P. Avouris, “Dissociation of Individual Molecules with Electrons from the Tip of a Scanning Tunneling Microscope,” *Science*, vol. 255, pp. 1232–1235, Mar. 1992.

[111] J. Gimzewski, T. Jung, M. Cuberes, and R. Schlittler, “Scanning tunneling microscopy of individual molecules: Beyond imaging,” *Surface Science*, vol. 386, pp. 101–114, Oct. 1997.

[112] G. D. Nguyen, H.-Z. Tsai, A. A. Omrani, T. Marangoni, M. Wu, D. J. Rizzo, G. F. Rodgers, R. R. Cloke, R. A. Durr, Y. Sakai, F. Liou, A. S. Aikawa, J. R. Chelikowsky, S. G. Louie, F. R. Fischer, and M. F. Crommie, “Atomically precise graphene nanoribbon heterojunctions from a single molecular precursor,” *Nature Nanotechnology*, vol. 12, p. 1077, Nov. 2017.

[113] E. Carbonell-Sanromà, J. Hieulle, M. Vilas-Varela, P. Brandimarte, M. Iraola, A. Barragán, J. Li, M. Abadia, M. Corso, D. Sánchez-Portal, D. Peña, and J. I. Pascual, “Doping of Graphene Nanoribbons via Functional Group Edge Modification,” *ACS Nano*, vol. 11, pp. 7355–7361, July 2017.

[114] L. E. Dinca, C. Fu, J. M. MacLeod, J. Lipton-Duffin, J. L. Brusso, C. E. Szakacs, D. Ma, D. F. Perepichka, and F. Rosei, “Unprecedented Transformation of Tetrathienoanthracene into Pentacene on Ni(111),” *ACS Nano*, vol. 7, pp. 1652–1657, Feb. 2013.

[115] H. Shi, Y. Liu, J. Song, X. Lu, Y. Geng, J. Zhang, J. Xie, and Q. Zeng, “On-Surface Synthesis of Self-Assembled Monolayers of Benzothiazole Derivatives Studied by STM and XPS,” *Langmuir*, vol. 33, pp. 4216–4223, May 2017.

[116] S.-W. Hla and K.-H. Rieder, “STM Control of Chemical Reactions: Single-Molecule Synthesis,” *Annual Review of Physical Chemistry*, vol. 54, no. 1, pp. 307–330, 2003.

[117] W. Ho, “Single-molecule chemistry,” *The Journal of Chemical Physics*, vol. 117, pp. 11033–11061, Dec. 2002.

[118] Z. Li, K. Schouteden, V. Iancu, E. Janssens, P. Lievens, C. Van Haesendonck, and J. I. Cerdá, “Chemically modified STM tips for atomic-resolution imaging of ultrathin NaCl films,” *Nano Research*, vol. 8, pp. 2223–2230, July 2015.

[119] L. Gross, N. Moll, F. Mohn, A. Curioni, G. Meyer, F. Hanke, and M. Persson, "High-Resolution Molecular Orbital Imaging Using a p -Wave STM Tip," *Physical Review Letters*, vol. 107, Aug. 2011.

[120] C.-l. Chiang, C. Xu, Z. Han, and W. Ho, "Real-space imaging of molecular structure and chemical bonding by single-molecule inelastic tunneling probe," *Science*, vol. 344, pp. 885–888, May 2014.

[121] J. Repp, G. Meyer, S. Paavilainen, F. E. Olsson, and M. Persson, "Scanning Tunneling Spectroscopy of Cl Vacancies in NaCl Films: Strong Electron-Phonon Coupling in Double-Barrier Tunneling Junctions," *Physical Review Letters*, vol. 95, Nov. 2005.

[122] J. Repp, G. Meyer, S. M. Stojković, A. Gourdon, and C. Joachim, "Molecules on Insulating Films: Scanning-Tunneling Microscopy Imaging of Individual Molecular Orbitals," *Phys. Rev. Lett.*, vol. 94, p. 026803, Jan. 2005.

[123] Y.-l. Wang, Z.-h. Cheng, Z.-t. Deng, H.-m. Guo, S.-x. Du, and H.-j. Gao, "Modifying the STM Tip for the ' Ultimate ' Imaging of the Si(111)-7×7 Surface and Metal-supported Molecules," *CHIMIA International Journal for Chemistry*, vol. 66, pp. 31–37, Feb. 2012.

[124] G. Schull, T. Frederiksen, M. Brandbyge, and R. Berndt, "Passing Current through Touching Molecules," *Physical Review Letters*, vol. 103, Nov. 2009.

[125] G. Schull, T. Frederiksen, A. Arnau, D. Sánchez-Portal, and R. Berndt, "Atomic-scale engineering of electrodes for single-molecule contacts," *Nature Nanotechnology*, vol. 6, pp. 23–27, Jan. 2011.

[126] G. Mándi and K. Palotás, "Chen's derivative rule revisited: Role of tip-orbital interference in STM," *Physical Review B*, vol. 91, Apr. 2015.

[127] L. Pauling, "The nature of the chemical bond. Application of results obtained from the quantum mechanics and from a theory of paramagnetic susceptibility to the structure of molecules," *J. Am. Chem. Soc.*, vol. 53, pp. 1367–1400, Apr. 1931.

[128] E. V. Anslyn and D. A. Dougherty, *Modern Physical Organic Chemistry*. University Science Books, 2006.

[129] "Molecular orbitals in Carbon Monoxide." http://www.chemtube3d.com/orbitalsCO.htm.

[130] Z. Han, G. Czap, C.-l. Chiang, C. Xu, P. J. Wagner, X. Wei, Y. Zhang, R. Wu, and W. Ho, "Imaging the halogen bond in self-assembled halogenbenzenes on silver," *Science*, vol. 358, pp. 206–210, Oct. 2017.

[131] G. Binnig, C. F. Quate, and C. Gerber, "Atomic Force Microscope," *Physical Review Letters*, vol. 56, pp. 930–933, Mar. 1986.

[132] E. C. Teague, F. E. Scire, S. M. Baker, and S. W. Jensen, "Three-dimensional stylus profilometry," *Wear*, vol. 83, pp. 1–12, Dec. 1982.

[133] J. R. Matey and J. Blanc, “Scanning capacitance microscopy,” *Journal of Applied Physics*, vol. 57, pp. 1437–1444, Mar. 1985.

[134] G. Binnig, C. Gerber, E. Stoll, T. R. Albrecht, and C. F. Quate, “Atomic resolution with atomic force microscope,” *Surface Science*, vol. 189-190, pp. 1–6, Oct. 1987.

[135] F. J. Giessibl, “Atomic Resolution of the Silicon (111)-(7x7) Surface by Atomic Force Microscopy,” *Science*, vol. 267, pp. 68–71, Jan. 1995.

[136] S. Morita, Y. Sugawara, and Y. Fukano, “Atomic Force Microscope Combined with Scanning Tunneling Microscope [AFM/STM],” *Jpn. J. Appl. Phys.*, vol. 32, p. 2983, June 1993.

[137] K.-C. Chang, Y.-W. Chiang, C.-H. Yang, and J.-W. Liou, “Atomic force microscopy in biology and biomedicine,” *Tzu Chi Medical Journal*, vol. 24, pp. 162–169, Dec. 2012.

[138] R. G. Reifenberger, *Fundamentals of Atomic Force Microscopy*. World Scientific, Jan. 2015.

[139] F. J. Giessibl, “Advances in atomic force microscopy,” *Rev. Mod. Phys.*, vol. 75, no. 3, p. 35, 2003.

[140] N. A. Geisse, “AFM and combined optical techniques,” *Materials Today*, vol. 12, pp. 40–45, July 2009.

[141] S. Morita, R. Wiesendanger, and E. Meyer, *Noncontact Atomic Force Microscopy*. Springer Science & Business Media, Dec. 2012.

[142] T. Schimmel, T. Koch, J. Küppers, and M. Lux-Steiner, “True atomic resolution under ambient conditions obtained by atomic force microscopy in the contact mode,” *Appl Phys A*, vol. 68, pp. 399–402, Apr. 1999.

[143] Y. G. Kuznetsov, P. D. Gershon, and A. McPherson, “Atomic Force Microscopy Investigation of Vaccinia Virus Structure,” *Journal of Virology*, vol. 82, pp. 7551–7566, Aug. 2008.

[144] Y. G. Kuznetsov, C. Xiao, S. Sun, D. Raoult, M. Rossmann, and A. McPherson, “Atomic force microscopy investigation of the giant mimivirus,” *Virology*, vol. 404, pp. 127–137, Aug. 2010.

[145] A. J. Malkin, A. McPherson, and P. D. Gershon, “Structure of Intracellular Mature Vaccinia Virus Visualized by In Situ Atomic Force Microscopy,” *Journal of Virology*, vol. 77, pp. 6332–6340, June 2003.

[146] S. Kasas, N. H. Thomson, B. L. Smith, H. G. Hansma, X. Zhu, M. Guthold, C. Bustamante, E. T. Kool, M. Kashlev, and P. K. Hansma, “Escherichia coli RNA Polymerase Activity Observed Using Atomic Force Microscopy,” *Biochemistry*, vol. 36, pp. 461–468, Jan. 1997.

[147] K. Rippe, M. Guthold, P. H. von Hippel, and C. Bustamante, "Transcriptional activation via DNA-looping: Visualization of intermediates in the activation pathway of E. coli RNA polymerase·σ54 holoenzyme by scanning force microscopy," *Journal of Molecular Biology*, vol. 270, pp. 125–138, July 1997.

[148] D. Wang and T. P. Russell, "Advances in Atomic Force Microscopy for Probing Polymer Structure and Properties," *Macromolecules*, vol. 51, pp. 3–24, Jan. 2018.

[149] S. N. Magonov and D. H. Reneker, "Characterization of Polymer Surfaces with Atomic Force Microscopy," *Annual Review of Materials Science*, vol. 27, no. 1, pp. 175–222, 1997.

[150] T. V. Vorburger, J. A. Dagata, G. Wilkening, K. Lizuka, E. G. Thwaite, and P. Lonardo, "Industrial Uses of STM and AFM," *CIRP Annals*, vol. 46, pp. 597–620, Jan. 1997.

[151] S. Morita, F. J. Giessibl, and R. Wiesendanger, eds., *Noncontact Atomic Force Microscopy. Vol. 2.* NanoScience and Technology, Berlin: Springer, 2009.

[152] F. J. Giessibl, "Principles and Applications of the qPlus Sensor," in *Noncontact Atomic Force Microscopy: Volume 2* (S. Morita, F. J. Giessibl, and R. Wiesendanger, eds.), NanoScience and Technology, pp. 121–142, Berlin, Heidelberg: Springer Berlin Heidelberg, 2009.

[153] F. J. Giessibl, "A direct method to calculate tip–sample forces from frequency shifts in frequency-modulation atomic force microscopy," *Appl. Phys. Lett.*, vol. 78, pp. 123–125, Dec. 2000.

[154] F. J. Giessibl, F. Pielmeier, T. Eguchi, T. An, and Y. Hasegawa, "Comparison of force sensors for atomic force microscopy based on quartz tuning forks and length-extensional resonators," *Phys. Rev. B*, vol. 84, p. 125409, Sept. 2011.

[155] F. J. Giessibl, "Atomic resolution on Si(111)-(7×7) by noncontact atomic force microscopy with a force sensor based on a quartz tuning fork," *Appl. Phys. Lett.*, vol. 76, pp. 1470–1472, Mar. 2000.

[156] D. P. Rosenblatt, "Construction of a low temperature STM and studies of large molecular systems," 2016.

[157] C. R. Ast, M. Assig, A. Ast, and K. Kern, "Design criteria for scanning tunneling microscopes to reduce the response to external mechanical disturbances," *Review of Scientific Instruments*, vol. 79, p. 093704, Sept. 2008.

[158] Y. Hasegawa and P. Avouris, "Manipulation of the Reconstruction of the Au(111) Surface with the STM," *Science*, vol. 258, pp. 1763–1765, Dec. 1992.

[159] R. Clausius, "Ueber die bewegende Kraft der Wärme und die Gesetze, welche sich daraus für die Wärmelehre selbst ableiten lassen," *Annalen der Physik*, vol. 155, no. 4, pp. 500–524.

[160] M. F. Crommie, C. P. Lutz, and D. M. Eigler, “Imaging standing waves in a two-dimensional electron gas,” *Nature*, vol. 363, pp. 524–527, June 1993.

[161] K. D. Sattler, *Fundamentals of Picoscience.* CRC Press, Sept. 2013.

[162] G. Ctistis, E. H. Frater, S. R. Huisman, J. P. Korterik, J. L. Herek, W. L. Vos, and P. W. H. Pinkse, “Controlling the quality factor of a tuning-fork resonance between 9 and 300 K for scanning-probe microscopy,” *J. Phys. D: Appl. Phys.*, vol. 44, no. 37, p. 375502, 2011.

[163] D. G. de Oteyza, P. Gorman, Y.-C. Chen, S. Wickenburg, A. Riss, D. J. Mowbray, G. Etkin, Z. Pedramrazi, H.-Z. Tsai, A. Rubio, M. F. Crommie, and F. R. Fischer, “Direct Imaging of Covalent Bond Structure in Single-Molecule Chemical Reactions,” *Science*, vol. 340, pp. 1434–1437, June 2013.

[164] H. Heinz, R. A. Vaia, B. L. Farmer, and R. R. Naik, “Accurate Simulation of Surfaces and Interfaces of Face-Centered Cubic Metals Using 12-6 and 9-6 Lennard-Jones Potentials,” *The Journal of Physical Chemistry C*, vol. 112, pp. 17281–17290, Nov. 2008.

[165] C. Hellingman, “Newton’s third law revisited,” *Phys. Educ.*, vol. 27, no. 2, p. 112, 1992.

[166] L. Gross, B. Schuler, F. Mohn, N. Moll, J. Repp, and G. Meyer, “Atomic Resolution on Molecules with Functionalized Tips,” *NanoScience and Technology*, vol. 97, pp. 223–246, May 2015.

[167] N. Moll, L. Gross, F. Mohn, A. Curioni, and G. Meyer, “The mechanisms underlying the enhanced resolution of atomic force microscopy with functionalized tips,” *New J. Phys.*, vol. 12, no. 12, p. 125020, 2010.

[168] F. Mohn, B. Schuler, L. Gross, and G. Meyer, “Different tips for high-resolution atomic force microscopy and scanning tunneling microscopy of single molecules,” *Appl. Phys. Lett.*, vol. 102, p. 073109, Feb. 2013.

[169] B. Schuler, W. Liu, A. Tkatchenko, N. Moll, G. Meyer, A. Mistry, D. Fox, and L. Gross, “Adsorption Geometry Determination of Single Molecules by Atomic Force Microscopy,” *Physical Review Letters*, vol. 111, Sept. 2013.

[170] A. M. Sweetman, S. P. Jarvis, H. Sang, I. Lekkas, P. Rahe, Y. Wang, J. Wang, N. R. Champness, L. Kantorovich, and P. Moriarty, “Mapping the force field of a hydrogen-bonded assembly,” *Nature Communications*, vol. 5, p. 3931, May 2014.

[171] H. Mönig, D. R. Hermoso, O. Díaz Arado, M. Todorović, A. Timmer, S. Schüer, G. Langewisch, R. Pérez, and H. Fuchs, “Submolecular Imaging by Noncontact Atomic Force Microscopy with an Oxygen Atom Rigidly Connected to a Metallic Probe,” *ACS Nano*, vol. 10, pp. 1201–1209, Jan. 2016.

[172] C.-S. Guo, M. A. Van Hove, R.-Q. Zhang, and C. Minot, “Prospects for Resolving Chemical Structure by Atomic Force Microscopy: A First-Principles Study,” *Langmuir*, vol. 26, pp. 16271–16277, Nov. 2010.

[173] L. Gross, F. Mohn, N. Moll, G. Meyer, R. Ebel, W. M. Abdel-Mageed, and M. Jaspars, "Organic structure determination using atomic-resolution scanning probe microscopy," *Nature Chemistry*, vol. 2, pp. 821–825, Oct. 2010.

[174] F. Mohn, J. Repp, L. Gross, G. Meyer, M. S. Dyer, and M. Persson, "Reversible Bond Formation in a Gold-Atom–Organic-Molecule Complex as a Molecular Switch," *Phys. Rev. Lett.*, vol. 105, p. 266102, Dec. 2010.

[175] F. Mohn, L. Gross, and G. Meyer, "Measuring the short-range force field above a single molecule with atomic resolution," *Appl. Phys. Lett.*, vol. 99, p. 053106, Aug. 2011.

[176] Z. Sun, M. P. Boneschanscher, I. Swart, D. Vanmaekelbergh, and P. Liljeroth, "Quantitative Atomic Force Microscopy with Carbon Monoxide Terminated Tips," *Phys. Rev. Lett.*, vol. 106, p. 046104, Jan. 2011.

[177] R. Pawlak, S. Kawai, S. Fremy, T. Glatzel, and E. Meyer, "Atomic-scale mechanical properties of orientated C60 molecules revealed by noncontact atomic force microscopy," *ACS Nano*, vol. 5, pp. 6349–6354, Aug. 2011.

[178] M. Schneiderbauer, M. Emmrich, A. J. Weymouth, and F. J. Giessibl, "CO Tip Functionalization Inverts Atomic Force Microscopy Contrast via Short-Range Electrostatic Forces," *Phys. Rev. Lett.*, vol. 112, p. 166102, Apr. 2014.

[179] S. Kawai, A. Sadeghi, F. Xu, L. Peng, A. Orita, J. Otera, S. Goedecker, and E. Meyer, "Extended Halogen Bonding between Fully Fluorinated Aromatic Molecules," *ACS Nano*, vol. 9, pp. 2574–2583, Mar. 2015.

[180] F. Albrecht, M. Neu, C. Quest, I. Swart, and J. Repp, "Formation and Characterization of a Molecule–Metal–Molecule Bridge in Real Space," *J. Am. Chem. Soc.*, vol. 135, pp. 9200–9203, June 2013.

[181] J. Welker and F. J. Giessibl, "Revealing the Angular Symmetry of Chemical Bonds by Atomic Force Microscopy," *Science*, vol. 336, pp. 444–449, Apr. 2012.

[182] J. Zhang, P. Chen, B. Yuan, W. Ji, Z. Cheng, and X. Qiu, "Real-Space Identification of Intermolecular Bonding with Atomic Force Microscopy," *Science*, vol. 342, pp. 611–614, Nov. 2013.

[183] L. Gross, F. Mohn, N. Moll, B. Schuler, A. Criado, E. Guitián, D. Peña, A. Gourdon, and G. Meyer, "Bond-order discrimination by atomic force microscopy," *Science*, vol. 337, pp. 1326–1329, Sept. 2012.

[184] N. Pavliček, B. Fleury, M. Neu, J. Niedenführ, C. Herranz-Lancho, M. Ruben, and J. Repp, "Atomic Force Microscopy Reveals Bistable Configurations of Dibenzo[a,h]thianthrene and their Interconversion Pathway," *Phys. Rev. Lett.*, vol. 108, p. 086101, Feb. 2012.

[185] N. Pavliček, I. Swart, J. Niedenführ, G. Meyer, and J. Repp, "Symmetry Dependence of Vibration-Assisted Tunneling," *Physical Review Letters*, vol. 110, Mar. 2013.

[186] F. Mohn, L. Gross, N. Moll, and G. Meyer, “Imaging the charge distribution within a single molecule,” *Nature Nanotechnology*, vol. 7, pp. 227–231, Apr. 2012.

[187] H. Sang, S. P. Jarvis, Z. Zhou, P. Sharp, P. Moriarty, J. Wang, Y. Wang, and L. Kantorovich, “Identifying tips for intramolecular NC-AFM imaging via *in situ* fingerprinting,” *Scientific Reports*, vol. 4, p. 6678, Oct. 2014.

[188] P. Hapala, G. Kichin, C. Wagner, F. S. Tautz, R. Temirov, and P. Jelínek, “Mechanism of high-resolution STM/AFM imaging with functionalized tips,” *Phys. Rev. B*, vol. 90, p. 085421, Aug. 2014.

[189] S. Morita, F. J. Giessibl, E. Meyer, and R. Wiesendanger, *Noncontact Atomic Force Microscopy.* Springer, May 2015.

[190] G. A. Somorjai, “The surface science of heterogeneous catalysis,” *Surface Science*, vol. 299-300, pp. 849–866, Jan. 1994.

[191] G. Ertl, “Elementary Steps in Heterogeneous Catalysis,” *Angewandte Chemie International Edition in English*, vol. 29, pp. 1219–1227, Nov. 1990.

[192] J. C. Cuevas and E. Scheer, *Molecular Electronics: An Introduction to Theory and Experiment.* World Scientific, 2010.

[193] W. Haiss, R. J. Nichols, H. van Zalinge, S. J. Higgins, D. Bethell, and D. J. Schiffrin, “Measurement of single molecule conductivity using the spontaneous formation of molecular wires,” *Phys. Chem. Chem. Phys.*, vol. 6, pp. 4330–4337, Aug. 2004.

[194] I. Pong, S. Yau, P.-Y. Huang, M.-C. Chen, T.-S. Hu, Y. Yang, and Y.-L. Lee, “In Situ STM Imaging of the Structures of Pentacene Molecules Adsorbed on Au(111),” *Langmuir*, vol. 25, pp. 9887–9893, Sept. 2009.

[195] P. Guaino, A. A. Cafolla, D. Carty, G. Sheerin, and G. Hughes, “An STM investigation of the interaction and ordering of pentacene molecules on the Ag/Si(111)-($\sqrt{3}\times\sqrt{3}$)R30° surface,” *Surface Science*, vol. 540, pp. 107–116, Aug. 2003.

[196] J. Gall, P. Zeppenfeld, L. Sun, L. Zhang, Y. Luo, Z. Dong, C. Hu, and P. Puschnig, “Spectroscopic STM studies of single pentacene molecules on Cu(110) - c(6x2)O,” *Phys. Rev. B*, vol. 94, p. 195441, Nov. 2016.

[197] A. Kabakchiev, K. Kuhnke, T. Lutz, and K. Kern, “Electroluminescence from Individual Pentacene Nanocrystals,” *ChemPhysChem*, vol. 11, pp. 3412–3416, Nov. 2010.

[198] S. Koslowski, D. Rosenblatt, A. Kabakchiev, K. Kuhnke, K. Kern, and U. Schlickum, “Adsorption and electronic properties of pentacene on thin dielectric decoupling layers,” *Beilstein J Nanotechnol*, vol. 8, pp. 1388–1395, July 2017.

[199] G. Dujardin and A. J. Mayne, *Atomic and Molecular Manipulation.* Elsevier, Sept. 2011.

[200] T. Suzuki, D. C. Sorescu, and J. T. Yates, "The chemisorption of pentacene on Si(001)-2×1," *Surface Science*, vol. 600, pp. 5092–5103, Dec. 2006.

[201] P. H. Lippel, R. J. Wilson, M. D. Miller, C. Wöll, and S. Chiang, "High-Resolution Imaging of Copper-Phthalocyanine by Scanning-Tunneling Microscopy," *Physical Review Letters*, vol. 62, pp. 171–174, Jan. 1989.

[202] V. M. Hallmark, S. Chiang, K.-P. Meinhardt, and K. Hafner, "Observation and calculation of internal structure in scanning tunneling microscopy images of related molecules," *Phys. Rev. Lett.*, vol. 70, pp. 3740–3743, June 1993.

[203] P. G. Falkowski, T. Fenchel, and E. F. Delong, "The microbial engines that drive Earth's biogeochemical cycles," *Science*, vol. 320, pp. 1034–1039, May 2008.

[204] U. G. Wortmann and A. Paytan, "Rapid Variability of Seawater Chemistry Over the Past 130 Million Years," *Science*, vol. 337, pp. 334–336, July 2012.

[205] I. Zhelezinskaia, A. J. Kaufman, J. Farquhar, and J. Cliff, "Large sulfur isotope fractionations associated with Neoarchean microbial sulfate reduction," *Science*, vol. 346, pp. 742–744, Nov. 2014.

[206] B. S. Liu, D. F. Xu, J. X. Chu, W. Liu, and C. T. Au, "Deep Desulfurization by the Adsorption Process of Fluidized Catalytic Cracking (FCC) Diesel over Mesoporous Al-MCM-41 Materials," *Energy Fuels*, vol. 21, pp. 250–255, Jan. 2007.

[207] F. A. Duarte, P. d. A. Mello, C. A. Bizzi, M. A. G. Nunes, E. M. Moreira, M. S. Alencar, H. N. Motta, V. L. Dressler, and E. M. M. Flores, "Sulfur removal from hydrotreated petroleum fractions using ultrasound-assisted oxidative desulfurization process," *Fuel*, vol. 90, pp. 2158–2164, June 2011.

[208] J. Zhang, A. Wang, Y. Wang, H. Wang, and J. Gui, "Heterogeneous oxidative desulfurization of diesel oil by hydrogen peroxide: Catalysis of an amphipathic hybrid material supported on SiO2," *Chemical Engineering Journal*, vol. 245, pp. 65–70, June 2014.

[209] J. L. García-Gutiérrez, G. C. Laredo, P. García-Gutiérrez, and F. Jiménez-Cruz, "Oxidative desulfurization of diesel using promising heterogeneous tungsten catalysts and hydrogen peroxide," *Fuel*, vol. 138, pp. 118–125, Dec. 2014.

[210] U. Kraft, J. E. Anthony, E. Ripaud, M. A. Loth, E. Weber, and H. Klauk, "Low-Voltage Organic Transistors Based on Tetraceno[2,3- *b*]thiophene: Contact Resistance and Air Stability," *Chemistry of Materials*, vol. 27, pp. 998–1004, Feb. 2015.

[211] F. Elfeninat, C. Fredriksson, E. Sacher, and A. Selmani, "A theoretical investigation of the interactions between thiophene and vanadium, chromium, copper, and gold," *The Journal of Chemical Physics*, vol. 102, pp. 6153–6158, Apr. 1995.

[212] P. Saalfrank, "Manipulation of adsorbates with electric fields," *The Journal of Chemical Physics*, vol. 113, pp. 3780–3791, Aug. 2000.

[213] C. Große, A. Kabakchiev, T. Lutz, R. Froidevaux, F. Schramm, M. Ruben, M. Etzkorn, U. Schlickum, K. Kuhnke, and K. Kern, “Dynamic Control of Plasmon Generation by an Individual Quantum System,” *Nano Lett.*, vol. 14, pp. 5693–5697, Oct. 2014.

[214] J. Stöhr, J. L. Gland, E. B. Kollin, R. J. Koestner, A. L. Johnson, E. L. Muetterties, and F. Sette, “Desulfurization and Structural Transformation of Thiophene on the Pt(111) Surface,” *Phys. Rev. Lett.*, vol. 53, pp. 2161–2164, Nov. 1984.

[215] L. E. Dinca, J. M. MacLeod, J. Lipton-Duffin, C. Fu, D. Ma, D. F. Perepichka, and F. Rosei, “Tailoring the Reaction Path in the On-Surface Chemistry of Thienoacenes,” *J. Phys. Chem. C*, vol. 119, pp. 22432–22438, Oct. 2015.

[216] L. Cheng, A. B. Bocarsly, S. L. Bernasek, and T. A. Ramanarayanan, “Adsorption and reaction of thiophene on the Fe(100) surface: Selective dehydrogenation and polymerization,” *Surface Science*, vol. 374, pp. 357–372, Mar. 1997.

[217] C. L. Garcia and J. A. Lercher, “Adsorption and surface reactions of thiophene on ZSM 5 zeolites,” *The Journal of Physical Chemistry*, vol. 96, pp. 2669–2675, Mar. 1992.

[218] J. Repp, G. Meyer, S. M. Stojković, A. Gourdon, and C. Joachim, “Molecules on Insulating Films: Scanning-Tunneling Microscopy Imaging of Individual Molecular Orbitals,” *Physical Review Letters*, vol. 94, Jan. 2005.

[219] J. Krüger, F. Eisenhut, J. M. Alonso, T. Lehmann, E. Guitián, D. Pérez, D. Skidin, F. Gamaleja, D. A. Ryndyk, C. Joachim, D. Peña, F. Moresco, and G. Cuniberti, “Imaging the electronic structure of on-surface generated hexacene,” *Chemical Communications*, vol. 53, no. 10, pp. 1583–1586, 2017.

[220] P. Hapala, R. Temirov, F. S. Tautz, and P. Jelínek, “Origin of High-Resolution IETS-STM Images of Organic Molecules with Functionalized Tips,” *Physical Review Letters*, vol. 113, Nov. 2014.

[221] K. Kuchitsu, T. Fukuyama, Y. Tamaru, Z. Yoshida, and I. Tabushi, “Carbon-sulfur bond distances and sulfur valence angles in 5-thiabicyclo[2.1.1]hexane and 7-thiabicyclo[2.2.1]heptane as determined by gas electron diffraction,” *J. Am. Chem. Soc.*, vol. 93, pp. 2799–2800, June 1971.

[222] E. Penocchio, M. Mendolicchio, N. Tasinato, and V. Barone, “Structural features of the carbon-sulfur chemical bond: A semi-experimental perspective,” *Can J Chem*, vol. 94, pp. 1065–1076, Dec. 2016.

[223] Y. Ye, M. Zhang, H. Liu, X. Liu, and J. Zhao, “Theoretical investigation on the oligothienoacenes under the influence of external electric field,” *Journal of Physics and Chemistry of Solids*, vol. 69, pp. 2615–2621, Nov. 2008.

[224] D. Serrate, M. Moro-Lagares, M. Piantek, J. I. Pascual, and M. R. Ibarra, “Enhanced Hydrogen Dissociation by Individual Co Atoms Supported on Ag(111),” *J. Phys. Chem. C*, vol. 118, pp. 5827–5832, Mar. 2014.

[225] L. Grill, K.-H. Rieder, F. Moresco, S. Stojkovic, A. Gourdon, and C. Joachim, "Exploring the Interatomic Forces between Tip and Single Molecules during STM Manipulation," *Nano Letters*, vol. 6, pp. 2685–2689, Dec. 2006.

[226] L. Grill, K.-H. Rieder, F. Moresco, G. Rapenne, S. Stojkovic, X. Bouju, and C. Joachim, "Rolling a single molecular wheel at the atomic scale," *Nature Nanotechnology*, vol. 2, pp. 95–98, Feb. 2007.

[227] T. Kudernac, N. Ruangsupapichat, M. Parschau, B. Maciá, N. Katsonis, S. R. Harutyunyan, K.-H. Ernst, and B. L. Feringa, "Electrically driven directional motion of a four-wheeled molecule on a metal surface," *Nature*, vol. 479, pp. 208–211, Nov. 2011.

[228] J. M. van Ruitenbeek, A. Alvarez, I. Piñeyro, C. Grahmann, P. Joyez, M. H. Devoret, D. Esteve, and C. Urbina, "Adjustable nanofabricated atomic size contacts," *Review of Scientific Instruments*, vol. 67, pp. 108–111, Jan. 1996.

[229] M. A. Reed, C. Zhou, C. J. Muller, T. P. Burgin, and J. M. Tour, "Conductance of a Molecular Junction," *Science*, vol. 278, pp. 252–254, Oct. 1997.

[230] J. Reichert, R. Ochs, D. Beckmann, H. B. Weber, M. Mayor, and H. v. Löhneysen, "Driving Current through Single Organic Molecules," *Phys. Rev. Lett.*, vol. 88, p. 176804, Apr. 2002.

[231] A. Yazdani, D. M. Eigler, and N. D. Lang, "Off-Resonance Conduction Through Atomic Wires," *Science*, vol. 272, pp. 1921–1924, June 1996.

[232] G. Reecht, H. Bulou, F. Scheurer, V. Speisser, F. Mathevet, C. González, Y. J. Dappe, and G. Schull, "Pulling and Stretching a Molecular Wire to Tune its Conductance," *J. Phys. Chem. Lett.*, vol. 6, pp. 2987–2992, Aug. 2015.

[233] C. Nacci, F. Ample, D. Bleger, S. Hecht, C. Joachim, and L. Grill, "Conductance of a single flexible molecular wire composed of alternating donor and acceptor units," *Nature Communications*, vol. 6, p. 7397, July 2015.

[234] S. Schmaus, A. Bagrets, Y. Nahas, T. K. Yamada, A. Bork, M. Bowen, E. Beaurepaire, F. Evers, and W. Wulfhekel, "Giant magnetoresistance through a single molecule," *Nature Nanotechnology*, vol. 6, pp. 185–189, Mar. 2011.

[235] N. Xiang, X. Huang, X. Feng, Y. Liu, B. Zhao, L. Deng, P. Shen, J. Fei, and S. Tan, "The structural modification of thiophene-linked porphyrin sensitizers for dye-sensitized solar cells," *Dyes and Pigments*, vol. 88, pp. 75–83, Jan. 2011.

[236] J. Das, R. B. K. Siram, D. Cahen, B. Rybtchinski, and G. Hodes, "Thiophene-modified perylenediimide as hole transporting material in hybrid lead bromide perovskite solar cells," *J. Mater. Chem. A*, vol. 3, pp. 20305–20312, Oct. 2015.

[237] M. S. Noé, R. W. Sinkeldam, and Y. Tor, "Oligodeoxynucleotides Containing Multiple Thiophene-Modified Isomorphic Fluorescent Nucleosides," *J. Org. Chem.*, vol. 78, pp. 8123–8128, Aug. 2013.

[238] M. M. S. Silva, A. C. M. S. Dias, M. T. Cordeiro, E. Marques, M. O. F. Goulart, and R. F. Dutra, “A thiophene-modified screen printed electrode for detection of dengue virus NS1 protein,” *Talanta*, vol. 128, pp. 505–510, Oct. 2014.

[239] J. Blackburn, M. Arnold, and S. Doorn, *Carbon Nanostructures for Energy Conversion*. The Electrochemical Society, Sept. 2016.

[240] T. A. Su, M. Neupane, M. L. Steigerwald, L. Venkataraman, and C. Nuckolls, “Chemical principles of single-molecule electronics,” *Nature Reviews Materials*, vol. 1, p. 16002, Mar. 2016.

[241] G. A. Somorjai and Y. Li, “Impact of surface chemistry,” *PNAS*, vol. 108, pp. 917–924, Jan. 2011.

[242] K. Anggara, L. Leung, M. J. Timm, Z. Hu, and J. C. Polanyi, “Approaching the forbidden fruit of reaction dynamics: Aiming reagent at selected impact parameters,” *Science Advances*, vol. 4, p. eaau2821, Oct. 2018.

[243] V. Grill, J. Shen, C. Evans, and R. G. Cooks, “Collisions of ions with surfaces at chemically relevant energies: Instrumentation and phenomena,” *Review of Scientific Instruments*, vol. 72, pp. 3149–3179, July 2001.

[244] J. Cyriac, T. Pradeep, H. Kang, R. Souda, and R. G. Cooks, “Low-Energy Ionic Collisions at Molecular Solids,” *Chemical Reviews*, vol. 112, pp. 5356–5411, Oct. 2012.

[245] H.-P. Cheng and U. Landman, “Controlled Deposition, Soft Landing, and Glass Formation in Nanocluster-Surface Collisions,” *Science*, vol. 260, pp. 1304–1307, May 1993.

[246] G. Dubey, R. Urcuyo, S. Abb, G. Rinke, M. Burghard, S. Rauschenbach, and K. Kern, “Chemical Modification of Graphene via Hyperthermal Molecular Reaction,” *J. Am. Chem. Soc.*, vol. 136, pp. 13482–13485, Oct. 2014.

[247] K. D. D. Gunaratne, V. Prabhakaran, Y. M. Ibrahim, R. V. Norheim, G. E. Johnson, and J. Laskin, “Design and performance of a high-flux electrospray ionization source for ion soft landing,” *Analyst*, vol. 140, pp. 2957–2963, Apr. 2015.

[248] G. E. Johnson, D. Gunaratne, and J. Laskin, “Soft- and reactive landing of ions onto surfaces: Concepts and applications,” *Mass Spectrometry Reviews*, vol. 35, pp. 439–479, Apr. 2015.

[249] S. Rauschenbach, M. Ternes, L. Harnau, and K. Kern, “Mass Spectrometry as a Preparative Tool for the Surface Science of Large Molecules,” *Annual Review of Analytical Chemistry*, vol. 9, no. 1, pp. 473–498, 2016.

[250] G. Rinke, *Electrospray Ion Beam Deposition of Complex Non-Volatile Molecules*. PhD thesis, Ecole Polytechnique Federale de Lousanne, 2013.

[251] J. B. Fenn, M. Mann, C. K. Meng, S. F. Wong, and C. M. Whitehouse, "Electrospray ionization for mass spectrometry of large biomolecules," *Science*, vol. 246, pp. 64–71, Oct. 1989.

[252] G. R. Taylor, "Disintegration of Water Drops in an Electric Field," *Proceedings of the Royal Society A: Mathematical, Physical and Engineering Sciences*, July 1964.

[253] K.-Y. Li, H. Tu, and A. K. Ray, "Charge Limits on Droplets during Evaporation," *Langmuir*, vol. 21, pp. 3786–3794, Apr. 2005.

[254] P. E. Miller and M. B. Denton, "The quadrupole mass filter: Basic operating concepts," *J. Chem. Educ.*, vol. 63, p. 617, July 1986.

[255] L. Vitali, G. Levita, R. Ohmann, A. Comisso, A. De Vita, and K. Kern, "Portrait of the potential barrier at metal–organic nanocontacts," *Nature Materials*, vol. 9, pp. 320–323, Apr. 2010.

[256] S. Hu, T. Shima, and Z. Hou, "Carbon–carbon bond cleavage and rearrangement of benzene by a trinuclear titanium hydride," *Nature*, vol. 512, pp. 413–415, Aug. 2014.

[257] "A metal enzyme that can cleave benzene rings - Healthcare industry." https://www.gesundheitsindustrie-bw.de/en/article/news/a-metal-enzyme-that-can-cleave-benzene-rings/.

[258] Z. Zhang, X. Gong, S. Zhang, H. Yang, Y. Shi, C. Yang, X. Zhang, X. Xiong, X. Fang, and Z. Ouyang, "Observation of Replacement of Carbon in Benzene with Nitrogen in a Low-Temperature Plasma," *Scientific Reports*, vol. 3, p. 3481, Dec. 2013.

[259] S. Koslowski, "Scanning tunneling microscopy on large bio-molecular systems on surfaces," 2017.

[260] S. Abb, L. Harnau, R. Gutzler, S. Rauschenbach, and K. Kern, "Two-dimensional honeycomb network through sequence-controlled self-assembly of oligopeptides," *Nature Communications*, vol. 7, p. 10335, Jan. 2016.

[261] S. Abb, "Molecular Imaging of Biopolymers Enabled by Electrospray-Ion Beam Deposition," 2017.

[262] G. Rinke, S. Rauschenbach, L. Harnau, A. Albarghash, M. Pauly, and K. Kern, "Active Conformation Control of Unfolded Proteins by Hyperthermal Collision with a Metal Surface," *Nano Lett.*, vol. 14, pp. 5609–5615, Oct. 2014.

[263] C. R. Bertozzi and R. Sasisekharan, "Glycomics," in *Essentials of Glycobiology* (A. Varki, R. D. Cummings, J. D. Esko, H. H. Freeze, P. Stanley, C. R. Bertozzi, G. W. Hart, and M. E. Etzler, eds.), Cold Spring Harbor (NY): Cold Spring Harbor Laboratory Press, 2nd ed., 2009.

[264] A. Varki, R. D. Cummings, J. D. Esko, H. H. Freeze, P. Stanley, C. R. Bertozzi, G. W. Hart, and M. E. Etzler, eds., *Essentials of Glycobiology.* Cold Spring Harbor (NY): Cold Spring Harbor Laboratory Press, 2nd ed., 2009.

[265] R. A. Dwek, "Glycobiology: Toward Understanding the Function of Sugars," *Chem. Rev.*, vol. 96, pp. 683–720, Jan. 1996.

[266] M. Molinari, "N-glycan structure dictates extension of protein folding or onset of disposal," *Nature Chemical Biology*, vol. 3, pp. 313–320, June 2007.

[267] R. Apweiler, H. Hermjakob, and N. Sharon, "On the frequency of protein glycosylation, as deduced from analysis of the SWISS-PROT database11Dedicated to Prof. Akira Kobata and Prof. Harry Schachter on the occasion of their 65th birthdays.," *Biochimica et Biophysica Acta (BBA) - General Subjects*, vol. 1473, pp. 4–8, Dec. 1999.

[268] R. G. Spiro, "Protein glycosylation: Nature, distribution, enzymatic formation, and disease implications of glycopeptide bonds," *Glycobiology*, vol. 12, pp. 43R–56R, Apr. 2002.

[269] "Glycans," in *IUPAC Compendium of Chemical Terminology* (M. Nič, J. Jirát, B. Košata, A. Jenkins, and A. McNaught, eds.), Research Triagle Park, NC: IUPAC, 2.1.0 ed., June 2009.

[270] G.-J. Boons, ed., *Carbohydrate Chemistry.* Springer Netherlands, 1998.

[271] J. Hofmann, H. S. Hahm, P. H. Seeberger, and K. Pagel, "Identification of carbohydrate anomers using ion mobility–mass spectrometry," *Nature*, vol. 526, pp. 241–244, Oct. 2015.

[272] W. H. Brown and T. Poon, *Introduction to Organic Chemistry, 6th Edition.* Wiley, Jan. 2016.

[273] A. L. Lehninger, D. L. Nelson, and M. M. Cox, *Principles of Biochemistry.* New York W.H. Freeman, 5th ed ed., 2008.

[274] J. O. Duus, C. H. Gotfredsen, and K. Bock, "Carbohydrate Structural Determination by NMR Spectroscopy: Modern Methods and Limitations," *Chem. Rev.*, vol. 100, pp. 4589–4614, Dec. 2000.

[275] R. F. Service, "Looking for a Sugar Rush," *Science*, vol. 338, pp. 321–323, Oct. 2012.

[276] S. Daikoku, G. Widmalm, and O. Kanie, "Analysis of a series of isomeric oligosaccharides by energy-resolved mass spectrometry: A challenge on homobranched trisaccharides," *Rapid Communications in Mass Spectrometry*, vol. 23, pp. 3713–3719, Dec. 2009.

[277] J. M. Prien, D. J. Ashline, A. J. Lapadula, H. Zhang, and V. N. Reinhold, "The high mannose glycans from bovine ribonuclease B isomer characterization by ion trap MS," *J Am Soc Mass Spectrom*, vol. 20, pp. 539–556, Apr. 2009.

[278] J. Hofmann and K. Pagel, "Glycan Analysis by Ion Mobility–Mass Spectrometry," *Angewandte Chemie International Edition*, vol. 56, no. 29, pp. 8342–8349, 2017.

[279] C. Manz and K. Pagel, "Glycan analysis by ion mobility-mass spectrometry and gas-phase spectroscopy," *Current Opinion in Chemical Biology*, vol. 42, pp. 16–24, Feb. 2018.

[280] Z. Chen, M. S. Glover, and L. Li, "Recent advances in ion mobility–mass spectrometry for improved structural characterization of glycans and glycoconjugates," *Current Opinion in Chemical Biology*, vol. 42, pp. 1–8, Feb. 2018.

[281] "Biomolecular Systems - Research Program, Max Planck Institute of Colloids and Interfaces." http://www.mpikg.mpg.de/biomolecular-systems/research-program.

[282] A. Pardo-Vargas, M. Delbianco, and P. H. Seeberger, "Automated glycan assembly as an enabling technology," *Current Opinion in Chemical Biology*, vol. 46, pp. 48–55, Oct. 2018.

[283] A. C. Aragonès, N. L. Haworth, N. Darwish, S. Ciampi, N. J. Bloomfield, G. G. Wallace, I. Diez-Perez, and M. L. Coote, "Electrostatic catalysis of a Diels–Alder reaction," *Nature*, vol. 531, pp. 88–91, Mar. 2016.

[284] R. Meir, H. Chen, W. Lai, and S. Shaik, "Oriented Electric Fields Accelerate Diels–Alder Reactions and Control the endo/exo Selectivity," *ChemPhysChem*, vol. 11, no. 1, pp. 301–310, 2010.

[285] F. Che, J. T. Gray, S. Ha, N. Kruse, S. L. Scott, and J.-S. McEwen, "Elucidating the Roles of Electric Fields in Catalysis: A Perspective," *ACS Catal.*, vol. 8, pp. 5153–5174, June 2018.

[286] Y. Ie, K. Tanaka, A. Tashiro, S. K. Lee, H. R. Testai, R. Yamada, H. Tada, and Y. Aso, "Thiophene-based Tripodal Anchor Units for Hole Transport in Single-Molecule Junctions with Gold Electrodes," *The Journal of Physical Chemistry Letters*, vol. 6, pp. 3754–3759, Sept. 2015.

[287] E. Pensa, E. Cortés, G. Corthey, P. Carro, C. Vericat, M. H. Fonticelli, G. Benítez, A. A. Rubert, and R. C. Salvarezza, "The Chemistry of the Sulfur–Gold Interface: In Search of a Unified Model," *Acc. Chem. Res.*, vol. 45, pp. 1183–1192, Aug. 2012.

[288] S. Gronowitz, *Thiophene and Its Derivatives.* John Wiley & Sons, Sept. 2009.

[289] M. Pauly, M. Sroka, J. Reiss, G. Rinke, A. Albarghash, R. Vogelgesang, H. Hahne, B. Kuster, J. Sesterhenn, K. Kern, and S. Rauschenbach, "A hydrodynamically optimized nano-electrospray ionization source and vacuum interface," *Analyst*, vol. 139, pp. 1856–1867, Mar. 2014.

[290] C. S. Pereira, D. Kony, R. Baron, M. Müller, W. F. van Gunsteren, and P. H. Hünenberger, "Conformational and Dynamical Properties of Disaccharides in Water: A Molecular Dynamics Study," *Biophysical Journal*, vol. 90, pp. 4337–4344, June 2006.

List of Figures

1.1 Structures of organic molecules encountered in the oil processing resolved by nc-AFM . . . 4

2.1 Quantum tunneling effect . . . 8
2.2 Scheme of the STM . . . 9
2.3 Quantum corral . . . 12
2.4 Ullman reaction induced with an STM . . . 13
2.5 Pentacene on Cu(111) - pentacene tip . . . 14
2.6 Pentacene on NaCl(100) - pentacene tip . . . 15
2.7 STHM of PTCDA . . . 16
2.8 High resolution orbital imaging with a CO-terminated tip . . . 17
2.9 Inelastic Tunneling Probe imaging technique . . . 18

3.1 Two types of AFM . . . 22
3.2 Regimes of the AFM operation modes . . . 23
3.3 Shifts of the tuning fork resonance frequency . . . 25
3.4 Modern qPlus sensor design from *Omicron* . . . 26
3.5 The nc-AFM signal amplification circuit . . . 27
3.6 4 K STM/nc-AFM drawing . . . 28
3.7 4 K STM/nc-AFM head drawing . . . 29
3.8 qPlus sensor assembly . . . 30

3.9 4 K STM/nc-AFM photo 31

3.10 Noise spectrum, before the optimization 32

3.11 Noise spectrum, after the optimization 34

3.12 Final noise spectrum, 50 Hz peaks minimzed 34

3.13 Cu(111) atomic resolution 35

3.14 NaCl(100) on Cu(111) atomic resolution 35

3.15 Comparison of the resonance curves of the qPlus sensors 36

3.16 Influence of the nc-AFM operation on the low frequency noise 37

3.17 qPlus assembly before and ater embedding in the insulating epoxy 37

3.18 The resonance curve of the epoxy embedded qPlus sensor 38

3.19 Simultaneous STM/nc-AFM imaging 38

3.20 Lennard-Jones potential 39

3.21 Behavior of the CO molecule at the tip apex during the Pauli repulsion imaging 41

3.22 Pickup of the CO molecule from the NaCl 42

3.23 Changes of the CO apperance on Cu(111) 42

3.24 Pauli repulsion images of a reacted tetracenothiophene molecule 43

4.1 TCT and pentacene structures 46

4.2 Overview of the TCT molecules on Cu(111) 47

4.3 Two states of the TCT molecule on Cu(111) 47

4.4 Occurrence of the modified TCT specie in the function of the sample temperature 47

4.5 Locally induced reaction of the thiophene group 48

4.6 Threshold current and bias values in the function of the relative tip-sample distance 49

4.7 Threshold current and bias values in the function of the relative tip-sample distance 50

4.8 Orbital images of the TCT states compared with simulated appearance of surface-modified LUMO . . . 52

4.9 Pauli repulsion images of TCT . . . 53

4.10 Two-step reaction model . . . 56

4.11 Measurement of conductance through a single TCT molecule . . . 57

4.12 Conductance of the initial and final states of TCT in function of distance . . . 58

4.13 Conductance distribution in the 320-360 pm approach range . . . 59

4.14 TCT conductance histograms . . . 60

4.15 Electronic properties of pentacene and initial and final states of TCT . . . 61

5.1 Electrospraying . . . 65

5.2 Electrospray Ion Beam deposition technique . . . 66

5.3 Vacuum suitcase . . . 67

5.4 Reichardt's Dye . . . 68

5.5 Intact RD molecules on Cu(100) . . . 69

5.6 Optmized geometry of the RD molecule on Cu(100) . . . 70

5.7 Constant current Pauli repulsion image of RD . . . 70

5.8 Thermal reaction products of the RD annealing . . . 71

5.9 Pauli repulsion imaging of the Δ RD species . . . 71

5.10 Pauli repulsion imaging of the β species . . . 72

5.11 Thermally induced reaction of the Reichardt's Dye molecules . . . 73

5.12 Result of the hyperthermal landing of the Reichahrdt's Dye molecules . . . 74

5.13 Tip induced modification of the α' conformation . . . 75

5.14 Proposed structure of the α' species . . . 76

5.15 Schematic energy diagram representing the differences between thermal and hyperthermal activation of the Reichardt's Dye molecules . . . 77

6.1 Roles of glycans in the cell interface proccesses . . . 79

6.2 α and β D-glucose molecules 81

6.3 Glycosidation reaction of two α-D-glucose molecules 81

6.4 Branching of polysaccharides. 81

6.5 Linear and branched polymers of glucose 82

6.6 Workflow diagram of a glycoconjugate's structure determination. 84

6.7 Linear and branched polymers of mannose 85

6.8 Linear man5mer molecules on Cu(100) - overview 86

6.9 Clusters of linear man5mer molecules on Cu(100) with an observed substructure 87

6.10 Contamination on the Cu(111) surface after the cold transfer 88

6.11 Examples of nonclustered man5mer molecules 88

6.12 Details of substructure in clusters 89

6.13 Analysis of the topographic features of the nonclustered man5mer molecules . 89

6.14 Interpretation of nonclustered man5mer molecules 91

6.15 Overview of branched man5mer molecules on Cu(111) 92

6.16 Substructure observed in man6mer clusters 92

6.17 Pauli repulsion imaging of carbohydrate cluster 93

7.1 Thiophene desulfurization as an anchoring technique 97

List of Tables

6.1 Comparison of linear man5mer features 90

List of Publications

1. B. Borca, V. Schendel, R. Petuya, I. Pentegov, T. Michnowicz, U. Kraft, H. Klauk, A. Arnau, P. Wahl, U. Schlickum, K. Kern "Bipolar conductance switching of single anthradithiophene molecules", *ACS Nano* vol. 9, p. 12506, 2015.

2. V. Schendel, B. Borca, I. Pentegov, T. Michnowicz, U. Kraft, H. Klauk, P. Wahl, U. Schlickum, K. Kern "Remotely controlled isomer selective molecular switching", *Nano Letters* vol. 16, p. 93, 2015.

3. B. Borca*, T. Michnowicz*, R. Petuya*, M. Pristl, V. Schendel, I. Pentegov, U. Kraft, H. Klauk, P. Wahl, R. Gutzler, A. Arnau, U. Schlickum, K. Kern "Electric-field-driven direct desulfurization", *ACS Nano* vol. 11, p. 4703, 2017.

4. T. Michnowicz*, B. Borca*, R. Petuya*, V. Schendel, M. Pristl, I. Pentegov, U. Kraft, H. Klauk, P. Wahl, P. Mutombo, A. Arnau, U. Schlickum, K. Kern "Electric-field-driven direct desulfurization", *submitted.*

---

* - authors contributed equally

List of Acronyms

AFM	Atomic Force Microscopy
BJ	Break Junction
BR-STM	Bond Resolving Scanning Tunneling Microscopy
CCS	Collision Cross Section
DFT	Density Functional Theory
ES-IBD	Electrospray Ionization-Beam Deposition
HOMO	Highest Occupied Molecular Orbital
HV	High Vaccum
IM-MS	Ion Mobility Mass Spectrometry
LDOS	Local Density of States
LUMO	Lowest Unoccupied Molecular Orbital
MS	Mass Spectrometry
nc-AFM	Non-contact Atomic Force Microscopy
NMR	Nuclear Magnetic Resonance
PDOS	Projected Density of States
Q-TOF-MS	Quadrupole Time-of-flight Mass Spectrometry
RD	Reichardt's Dye
SEM	Scanning Electron Miscroscopy
SPM	Scanning Probe Microscopy
STHM	Scanning Tunneling Hydrogen Microscopy
STM	Scanning Tunneling Microscopy
TCT	Tetracenothiophene
TEM	Transmission Electron Miscroscopy
TOF-MS	Time-of-flight Mass Spectrometry
UHV	Ultra-high Vacuum

Eigenständigkeitserklärung

Hiermit versichere ich, dass ich die vorliegende Arbeit selbständig verfasst, keine anderen als die angegebenen Quellen und Hilfsmittel benutzt und wörtlich sowie inhaltlich übernommenen Stellen eindeutig gekennzeichnet habe. Diese Arbeit war weder vollständig noch in wesentlichen Teilen Gegenstand eines anderen Prüfungsverfahrens.

Konstanz, den

Unterschrift

Acknowledgements

I would like to thank:

Prof. Klaus Kern, for accepting me into the extraordinary group of people working together in the Nanoscale Science Department at Max Planck Institute for Solid State Research in Stuttgart. The environment and conditions created with a great effort of Prof. Kern are one of the best in the world. Participating in the research of the highest level carried out in this place was a pleasure.

Prof. Elke Scheer and Prof. Peter Nielaba, for agreeing to become members of the PhD thesis committee and evaluating my work.

Prof. Uta Schlickum, for guiding me through the long and not always easy PhD studies.

Dr. Bogdana Borca, for introducing me into the field of STM and preparing me for independent work.

Sabine Birtel, for helping me pass the everyday obstacles of German bureaucracy.

Wolfgang Stiepany, Peter Andler, Marko Memmler, Rafail Chaikevich, Martin Siemers, for their godlike engineering knowledge, which made our ideas possible to realize.

Dr. Sabine Abb, for patience and being a good friend.

Prof. Andres Arnau, Prof. Alessandro de Vita, Dr. Pavel Jelinek, Dr. Rémi Pétuya, Dr. Andrea Floris, Dr. Martina Stella, Dr. Pingo Mutombo and Dr. Kelvin Anggara for their theoretical support and fruitful collaboration.

Prof. Stephan Rauschenbach, Prof. Markus Ternes, Prof. Christian Schön, Prof. Dimas de Oteyza, Prof. Hadj Benia, Dr. Klaus Kuhnke, Dr. Pablo Merino, Dr. Alexander Riss, Dr. Rico Gutzler, Dr. Markus Etzkorn and Dr. Christian Ast, for sharing their knowledge and interesting discussions.

Prof. Peter Seeberger and Dr. Martina Delbianco for showing the perspectives of an applied STM research.

Abhishek Grewal, Alessio Scavuzzo, Sven Szilagyi, Shai Mangel, Dr. Matthias Muenks, Piotr Kot, Dr. Jacob Senkpiel, Dr. Ivan Pentegov, Tobias Wollandt, Dr. Xu Wu, Dr. Yuqi Wang, Dr. Chris Leon, Dr. Diana Hötger, Dr. Manish Garg, Haonan Huang, Maximilian Uhl, Andreas Topp, Dinesh Pinto, Carmen Rubio, Jason Peng, Domenico Paone, Hannah Ochner, Lukas Krumbein, Dr. Bastian Kern, Dr. Kelvin Anggara, Dr. Suman Sen, Dr. Sebastian Koslowski, Dr. Daniel Rosenblatt, Aditya Desai, Dr. Roberto Urcuyo and Dr. Lukas Schlipf, for the successful collaboration, interesting official and unofficial discussions, good atmosphere and time spent together.

Participants of "Nalewka" Meetings and Workshops, for embracing the "quality" of "home-made products".

Marcel Pristl, for his friendship and helping me go through the toughest time of the PhD.

My family, for lifelong support and positive approach to life.

Anna Rosławska, for this and all of the future adventures.

Stuttgart, February 2019 Tomasz